Faculty of Science and Technology

Department of Geosciences

Exploratory data analysis of flexural waves in Arctic fjord ice seismic data

Katrine Gotliebsen

Geo-3900 Master’s Thesis in Geology
May 2017

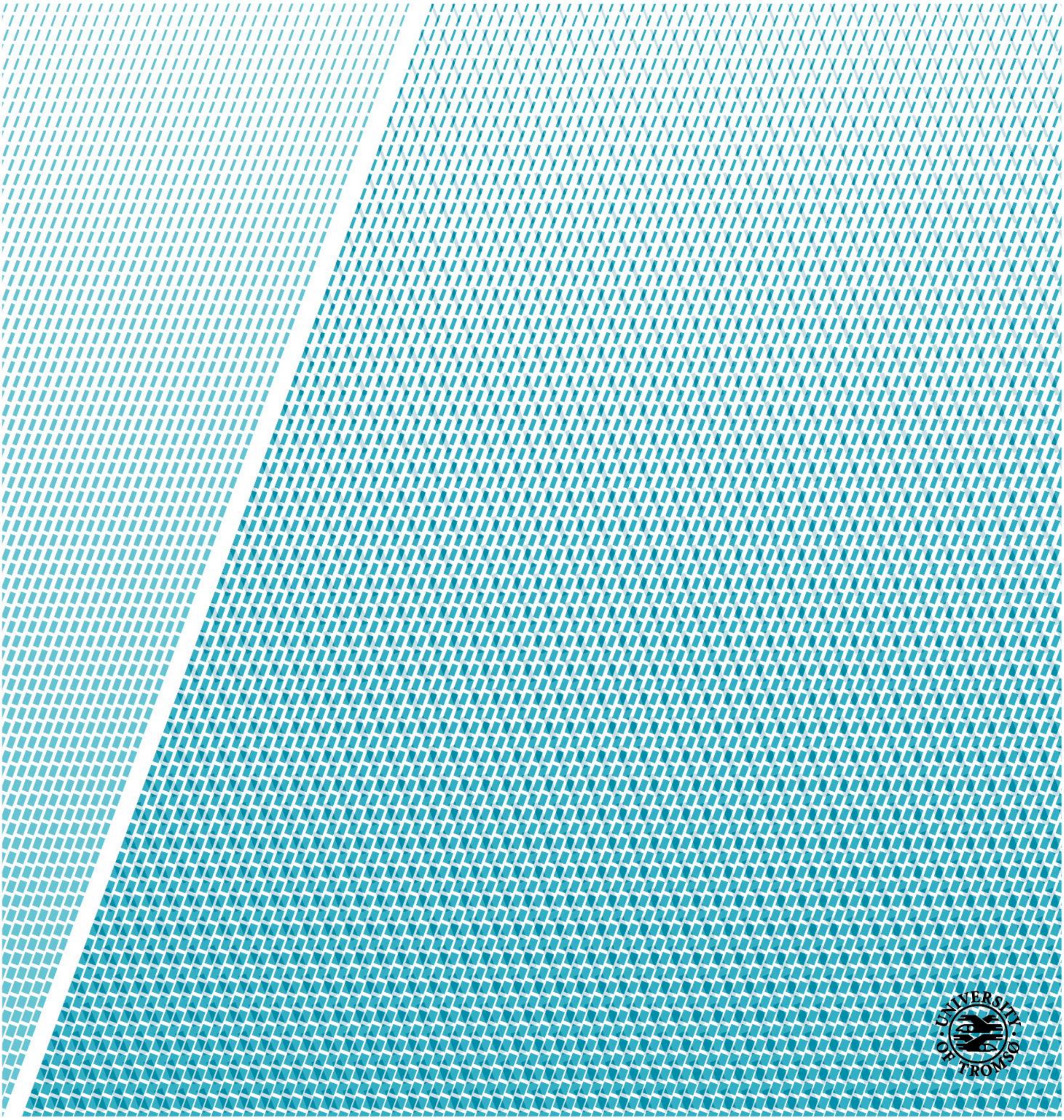

Abstract

A seismic source on floating ice induces flexural waves in the ice layer. An exploratory data analysis of Arctic fjord ice seismic data is performed for the purpose of identifying and studying characteristics of flexural waves and other related wave modes. Both geophone and hydrophone data are examined with the purpose of studying ice properties from ice wave behavior. Power spectral density estimates provide the frequency content of the entire signal, and studies of time-frequency plots have revealed both dispersive and non-dispersive ice related waves and their corresponding frequencies. F-k spectra are applied to study the dispersion relation for both flexural and acoustic ice waves. This provides the (variation in) wavelengths for the different waves. Velocities of the flexural waves are obtained by cross-correlating receivers at known offsets and by combining the obtained wavelengths with the period found from single receiver traces. Other observed waves include a guided direct wave in ice, a seafloor reflection and its multiples, and a refracted wave. The combination of several analysis methods makes it possible to identify several characteristics and properties of floating ice related waves, contributing to the understanding of such wave behavior. Wave characteristics of flexural and acoustic ice waves are combined to find ice properties like thickness and rigidity.

Acknowledgement

I thank my supervisor Professor Alfred Hanssen and my co-supervisor Professor Tor Arne Johansen for excellent advice, guidance and support during the work of my thesis. Further, I thank employees at the University of Bergen associated to the research project: Senior Engineer Bent Ole Ruud, ARCEx postdoc. Marcus Landschulze and ARCEx PhD Ronny Tømmerbakke, for providing the data, useful additional information to the data, advice and discussions on the topic. I also thank Rolf Andersen and Kristian Jensen for support on MATLAB issues.

Furthermore, I thank all my fellow students, both from the University of Bergen and the University of Tromsø, my family and my friends for support throughout the entire study program.

A special thanks to my office fellows for the past year, Suchada and Anna, for making this such a memorable time.

Katrine Gotliebsen

Contents

1 Introduction

Seismic explorations carried out on floating ice bring with them several challenges, both concerning logistics and costs of the acquisition itself and the quality and post-processing of the data. The difference in physical properties from air to ice and from ice to underlying water makes floating ice a “trap” for seismic energy. The large contrasts in density and seismic velocity between air, ice and water give rise to strong reflectors along the top and base of the ice, and therefore very little energy propagates through the water and reflects off the seafloor and deeper structures (Henley, 2004). The wave within the ice propagates as a flexural wave where velocity is depending on wave frequency and wavelength relative to the ice thickness. Flexural waves are waves depending on material properties and they change frequency and velocity as they propagate (Rovetta et al., 2009). Most of the energy registered in a receiver at the ice surface is the flexural wave, and thus the low amplitude reflections may be difficult to identify in the data. A seismogram with a strong dispersive wave shaded in yellow is seen in **Figure 1**.

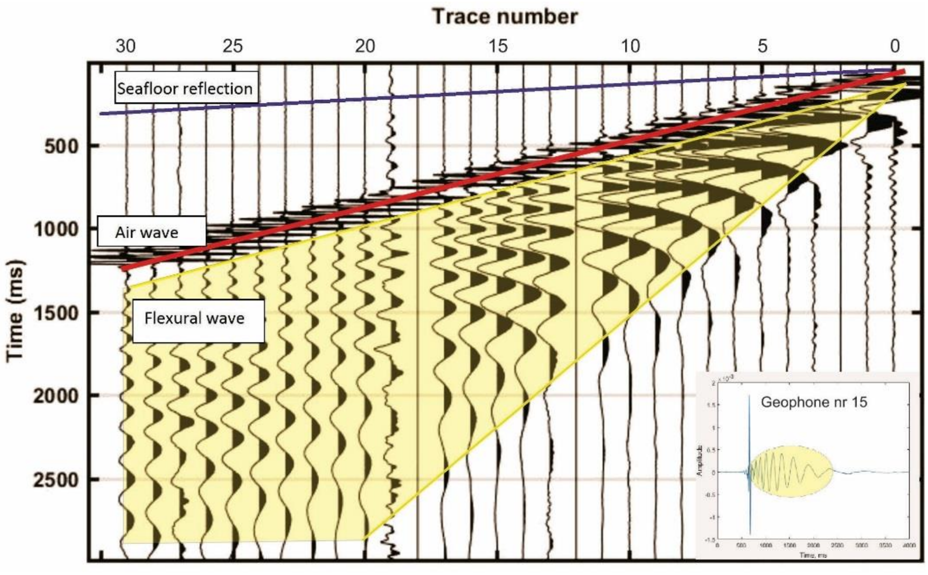

Figure 1 Seismogram with flexural wave (yellow shaded area) registered in geophones on floating ice. The direct air wave (red line) is prominent, while the seafloor reflection (blue line) is relatively weak. The single geophone trace in the lower right corner is the middle trace in the seismogram, 200 m from the source.

Because the phase velocity of flexural waves vary with angular frequency it is difficult to record them without aliasing (Henley, 2004). This leads to new difficulties in processing and attenuating the flexural noise and enhancing reflections of interest. Conventional techniques of filtering and muting can, to some degree, contribute to enhance the signal-to-noise ratio, but not enough to give a satisfying result (Del Molino et al., 2008).

1.1 Motivation for studies

Even though the Arctic sea ice raises great challenges to seismic explorations and data, there is an increased activity of explorations and acquisitions in the area. Imaging of the seafloor and the sub-seafloor may be useful in different manners, and being able to do this despite of the ice cover gives several possibilities in otherwise inaccessible areas. The fact that the oceans are covered in ice during most of the year makes it difficult to use standard marine geophysical methods, such as towed reflection seismic, to map the subsurface (Del Molino et al., 2008).

Seismic data collected on top of oceanic ice contains wave modes originated from the ice itself. Such waves are difficult to avoid and remove and as a consequence, such data may be used to study ice properties and deformation mechanisms based on the wave's dispersion relation (the relation between frequency and wavenumber), characteristics and behaviour of these waves. As wave propagation is affected by ice characteristics, the dispersion of flexural waves may be used for estimating ice temperature, thickness and distribution among others. Such information may be useful for large scale studies of sea ice (DiMarco et al., 1993), identification of climate changes and developing future climate models or sea ice forecast. A wide understanding of ice wave behaviour may be useful in developing techniques for distinguishing snow and ice from each other and thus be able to do large scale sea ice thickness measurements.

1.2 Previous work

Several attempts of seismic acquisitions in icy waters have been carried out (Hall et al., 2002; Henley, 2004; Lansley, Eilert & Nyland, 1984; Press et al., 1951), where most of them show masking of primary reflections by flexural waves. Studies of ice related waves have been conducted for different purposes where Ewing, Crary and Thorne (1934a, 1934b) and Press et al. (1951), among others, did studies of elastic waves propagating through floating ice. Ewing et al. (1934b) found a theoretical relation to calculate the velocity of flexural waves based on sea ice parameters. As sea ice is highly variable, this relation is not, however, applicable to all types of ice.

Several attempts on processing in order to reduce the flexural wave have been performed. These include deconvolution, transformations to different domains, muting and band-pass filtering, among others. Band-pass filtering alone is ineffective because the flexural wave’s frequencies and velocities cover most of the frequencies and velocities of the reflections. Conventional band-pass filtering will lead to cutting of reflections along with the noise, leaving little or no reflections in the data (Henley, 2004).

If the flexural wave can be avoided in the first place, no processing aimed at attenuating it would be required at a later stage. Earlier work (Rendelman & Levin, 1990; Henley, 2004) conclude that a source at the seafloor or buried in the shallow sediments is the most efficient set-up in terms of avoiding the flexural wave entirely. However, this is costly and difficult to carry out, especially in the Arctic where the sea ice cover is large. Press et al. (1951) discovered that a source located above ground (in the air) produces little or no flexural waves. On the contrary, dispersive waves were registered with a source located in the water in the vicinity of the ice. Bakke (2015) looked at how different acquisition geometries affect the amount of flexural noise. By studying the difference between seismograms from point and line sources, different angles between source and receivers, the use of geophones and hydrophones at varied depths below the ice, and different charges at the source, he found that hydrophones at great depths and line sources give less flexural waves in the data.

Combining hydrophones and geophones in a survey may attenuate flexural noise by destructive interference between geophones and hydrophones (Barr, Nyland & Sitton, 1993). Jensen (2015) did testing of this method, and found that it works quite well, but that a complete cancelation is not possible. The processing demonstrated by Jensen (2015) amplifies high frequencies and thus some noise is still present. Other attempts (George, 1997; Rosales & Antonie, 2004; Septayana et al., 2010) on removing the flexural wave based on the idea of Barr et al. (1993) have been performed by scaling the geophone to match the hydrophone before summing them. Coupling seafloor-based geophones and hydrophones was proved to be effective for reducing noise and increasing the signal-to-noise ratio in marine seismic data by Zhang et al. (2016). The method was tested on both synthetic and real data, revealing that the frequency bandwidth was broadened and water layer reverberations cancelled. The thought is that flexural waves are "ice reverberations" and the principle of destructive interference is the same as for water reverberations, and cancelation of flexural waves could be possible.

Jensen (2016) looked at how conventional processing affect the flexural wave by modelling it and adding it to synthetic seismic data. His modelling and testing of f-k processing, slant-stack processing and radial-trace (RT) processing concludes that f-k filtering might give good results when the receiver spacing is dense enough to avoid aliasing of the flexural wave. However, none of these methods give an optimal result of attenuated flexural waves and enhanced reflections.

As flexural waves have proven difficult to remove from seismic data, a few authors have looked into how they may be utilized for studying ice parameters. DiMarco et al. (1993) and Stein, Euerle and Parinella (1998) did this by studying the dispersion relation of flexural waves. By slightly different methods they managed to estimate the ice rigidity and a relationship between ice thickness and rigidity.

1.3 Objective of thesis

The purpose of this study is to look further into the dispersion of flexural waves found in Arctic fjord ice seismic data and how this may be utilized to study ice characteristics and properties. This requires modelling based on physical properties of ice and water, and knowledge about wave propagation through different viscoelastic media and the response of a plate when the surrounding media are fluids. Real data collected by the University of Bergen and the University Centre in Svalbard (UNIS) at Van Mijenfjorden, Svalbard in 2013 will be analysed to study flexural waves in hydrophone and geophone data. A picture from the acquisition in 2013 can be seen in **Figure 2**. Explosives were used to generate the source energy in this acquisition. The red sticks seen in the picture indicate the position of geophones, while hydrophones were lowered into the water through boreholes close to the geophones.

Figure 2 Seismic exploration performed on fjord ice close to Svea in 2013. (Photo by courtesy of UNIS AG-335 students, spring 2013.)

Studying fjord ice characteristics and properties, such as thickness and seismic velocity will be done by dedicated methods of frequency analysis, creating time-frequency plots and obtaining the f-k spectrum through a 2D FFT. To our knowledge, the estimation of physical properties by studying the flexural wave dispersion relation from real data in the f-k domain has not been done yet. By such analyses, ice mechanics and thickness will be estimated based on allowed frequency-wavenumber pairs found in the f-k spectrum.

2 Theory

2.1 Climate and sea ice in the Arctic

The Arctic extends to include Svalbard and major parts of North Norway. Together with the polar regions, the Arctic is a vulnerable area where climate changes are more evident than in the rest of the world due to the nature of winds and ocean currents. High latitudes cover small areas of Earth and hence changes here are more effective. Climate changes in the Arctic may be good indications of future changes in the rest of the world and are of great importance to global systems and the interactions between ice, land, ocean and atmosphere (Elverland & Norsk Polarinstitutt, 2008).

Considering the climate in Svalbard (Norwegian Arctic), a gradual increase in middle temperatures during the past 150 years is observed from temperature data registered at the weather station at Svalbard Airport, 28 meters above sea level (Meteorologisk Institutt, a). Climate is constantly varying, but today's changes occur at higher rates than previously, where greenhouse gases may be part of the cause (Elverland & Norsk Polarinstitutt, 2008). From 1912 until today, the middle temperature has increased by 2.2 °C, or approximately 0.22 °C pr. decade. For the last 50 years, the increase is 3.2 °C, meaning 0.65 °C pr. decade, which confirms the recent higher rate changes. Today, the temperature at Svalbard is at an all-time high (Meteorologisk Institutt, a).

The changing climate and increasing temperatures affect the sea ice cover. The Norwegian Meteorological Institute and NASA, among others, measure the sea ice extent and thickness in the Arctic Ocean from satellite images, where a gradually retreating sea ice is observed. Annual sea ice extent in the Arctic is at a maximum in March and at a minimum in September. In **Figure 3** we show that the minimum extent is decreasing faster than the maximum extent and that since 1980, the minimum extent was at an all-time low in 2012 (Meteorologisk Institutt, b). Climatic and oceanic conditions may cause short term variations in sea ice extent. In **Figure 3**, such short time variations are especially visible in the September trend. The figure is based on data from satellite images, which may also be used for developing climate models for predictions on future climate or studying deformation structures in ice to evaluate oceanic currents and eventual changes in them. Because salt precipitates when sea ice grows, the salinity just below the ice increases, meaning that when ice melts and/or grows, it impacts the salinity of the ocean which in turn affects the thermohaline circulation and the deep-water formation in the Arctic Ocean (Feltham, 2008), and later the global circulation in the rest of the world (Norwegian Polar Institute, 2016).

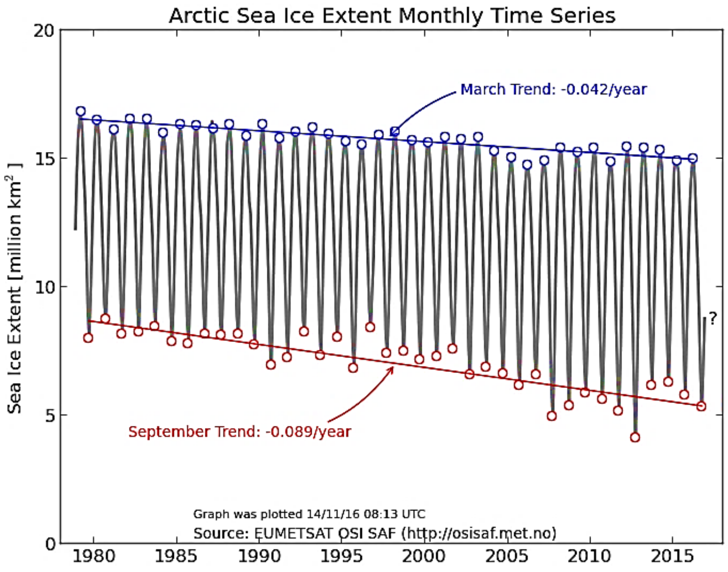

Figure 3 Total area covered by sea ice in March and September. (Graph from Ocean and Sea Ice Satellite Application Facility (OSI SAF)'s webpage.)

2.2 Wave theory

Propagation of a wave depends on the material in which it propagates. The propagation velocity is a function of frequency and wavelength, and therefore waves may be represented in both time and space by angular frequency, ω, and wavenumber, k. **Figure 4** illustrates a sinusoidal, or harmonic wave, travelling with velocity v. The wave is given by $Z(x,t) = Acos(kx - \omega t)$, i.e. it is a function of time, t, and distance x. A is the amplitude of the wave. The distance from one wave crest to the next is the wavelength, while the time between two crests is the period, T (Bécherrawy, 2013). Period gives the frequency from $f = \frac{1}{T}$. The relation between angular frequency and frequency is $\omega = 2\pi f$.

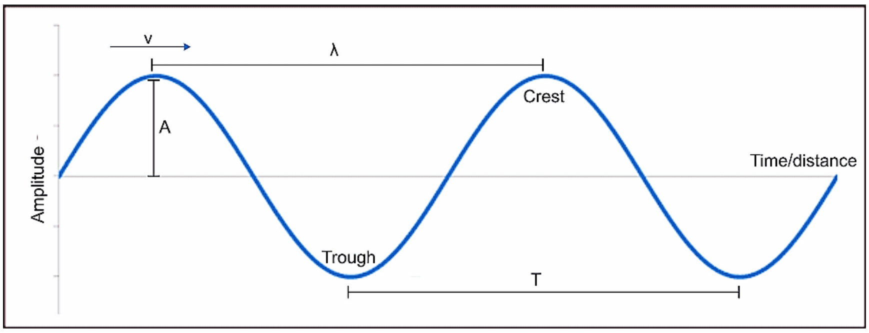

Figure 4 A sinusoidal propagating from zero time/distance. Period, amplitude and wavelength is indicated. The arrow indicates positive velocity/direction of propagation.

Seismic waves are complex compositions of several harmonics existing at the same time. Performing a Fourier analysis is a way of decomposing a signal into its individual components to estimate the frequency content. The opposite operation is a Fourier integration, where number of harmonic waves are summed to generate a pulse (Serway, Moses & Moyer, 2005).

If the wave in **Figure 4** shifts in time, the difference between two equal amplitudes in the original wave and the shifted one gives the angular shift. A phase shift, φ, is added to the cosine such that $Z(x,t) = A cos(kx - \omega t + \varphi)$.

2.2.1 Phase velocity, group velocity and dispersion

Velocity may be found from wavelength, λ, period and/or frequency as $v = \frac{\lambda}{T} = \lambda f$. From the wave equation of the simple harmonic of **Figure 4**, one also finds that $kx = \omega t$, which gives $\frac{x}{t} = \frac{\omega}{k}$, where $\frac{x}{t} = v$ is velocity. This gives that

$$v_p = \frac{\omega}{k}, \tag{2.1}$$

which is known as the *phase velocity* of the wave (Serway et al., 2005). Phase velocity is the propagation velocity of a single frequency component (simple harmonic) within the wave. The *group velocity* is the speed at which an envelope travels. One envelope consists of several harmonics propagating with different phase velocities. **Figure 5** is an illustration of how individual waves interfere to form envelopes moving at a different speed than the individual waves themselves. Group velocity is given as $v_g = \frac{\partial \omega}{\partial k}$, where $\frac{\partial \omega}{\partial k}$ is the partial derivative of ω with respect to k (Jenkins & White, 1957; Serway et al., 2005). This is considered as the wave velocity and the velocity at which energy travels (Gelius & Johansen, 2012).

Both phase and group velocity are affected by material properties. In homogenous and isotropic materials, wave fronts will be spherical and $v_p = v_g$. In anisotropic materials, wave fronts will no longer be spherical and $v_p \neq v_g$ (Gelius & Johansen, 2012).

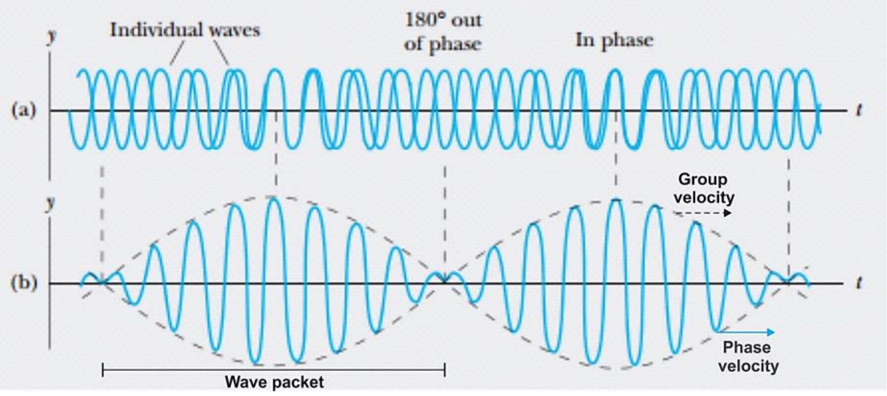

Figure 5 Illustration of phase velocity (blue arrow and line) and group velocity (black dashed). Where individual waves are in phase, the wave packet has the highest amplitude. Information propagates with the group velocity, while carrier waves propagate with the phase velocity. (Figure is modified from Serway et al. (2005)).

Dispersion causes different frequencies to travel at different phase velocities and distorts the wave packet as it travels. Usually, the wave seems to broaden and spread as a fan during propagation as was seen in **Figure 1**. Different waves have different dispersion relations as their propagation is differently depending on material properties. Dispersion relations are often visualized as curves showing how phase velocity changes with frequency (Del Molino et al., 2008). If the dispersion curve is linear it represents a non-dispersive wave. A one-dimensional wave along a string is an example of this. As derived in **Appendix B**, the equation describing a 1D wave propagating at velocity c causing displacement $u(x,t)$ is

$$\frac{\partial^2 u}{\partial t^2} = c^2 \frac{\partial^2 u}{\partial x^2}. \tag{2.2}$$

Separation of variables may be used to solve Eq. (2.2), which gives a relation between the angular frequency, wavenumber and velocity, i.e. the dispersion relation. For a 1D wave it is found in **Appendix B** as

$$\omega = kc. \tag{2.3}$$

This gives that the velocity is $\frac{\omega}{k}$, which equals the phase velocity, v_p, from Eq. (2.1), and thus dispersion describes how phase velocity varies with frequency $f = \frac{\omega}{2\pi}$ (Serway et al., 2005). As Eq. (2.3) is linear, the 1D wave is non-dispersive. The fundamental characteristic of flexural waves is that the dispersion relation is non-linear and the phase and group velocity change as frequency changes (Rovetta et al., 2009). This is observed by the decrease in frequency with time from the time-frequency analysis performed in this study, and from the non-linear relationship between frequency and wavenumber in the f-k spectra estimated from the data collected at Svea. These results will be presented in **Ch. 5**. Dispersion of the flexural wave in the Svea data is also visible in the single receiver traces as indicated in the single geophone trace of **Figure 1**.

Dispersion is one of the reasons for the challenges related to attenuation of flexural waves (Del Molino et al., 2008). Like other waves in general, the flexural wave attenuates with increasing propagated distance by absorption of energy, scattering from inhomogeneities (Hall et al., 2002), conversion from one wave mode to another (Worden, 2001) and geometrical spreading. The flexural wave is therefore less prominent with increasing distance between source and receiver (Yang & Yates, 1994) and consequently, most of the reflections masked by the dispersive wave is those registered close to the source and the shallow and low velocity ones. Attenuation may therefore increase data quality with increased water depth and source-receiver offset (Lansley et al., 1984).

One important concept when recording reflection signals is aliasing, which occurs when the sampling of a signal is not dense enough. This means that if a signal is sampled with a frequency lower than its actual one, the registrations indicate a signal of lower frequency than the actual one. Aliasing may occur both in time and space (Milsom & Eriksen, 2011a) if the sampling interval or the receiver spacing is too large. Aliasing is a common problem for seismic on floating ice, where the changing frequency of the flexural wave exposes it to aliasing, making the attenuation of it further challenging (Del Molino et al., 2008).

2.3 Mechanical and physical properties of saline ice

Formation and growth of lake ice and sea ice are similar, but the presence of salt in seawater causes physical and mechanical differences between the two types of ice. Typical salinity of sea ice is 4-6 ‰, which is much lower than the salinity of seawater (32-35 ‰) due to precipitation of salt as sea ice grows. Even though the salinity of sea ice is relatively low, the presence of salt gives rise to for example voids and pores filled with brine (Thomas & Dieckmann, 2010a). Such internal microstructures decrease mechanical strength, and thus saline ice is generally weaker than fresh water ice (Anderson & Weeks, 1958). As sea ice grows, the chance of trapped brine inclusions in the ice increases with increased water salnity (Pinet, 2013), and thus the content of brine is depending on the temperature and salinity of the water. The volume fraction of brine and trapped air bubbles are related to physical strength, where larger amounts of brine and bubbles lower the strength (Anderson & Weeks, 1958). Brine inclusions make up to 40% of the total ice volume (Thomas & Dieckmann, 2010a).

Fresh water ice is more transparent than saline ice because of the liquid inclusions in saline ice. A good example is shown in **Figure 6**, where the lack of liquid inclusions causes an apparent darker color and lower albedo of homogenous fresh water ice than of saline ice (Thomas & Dieckmann, 2010a).

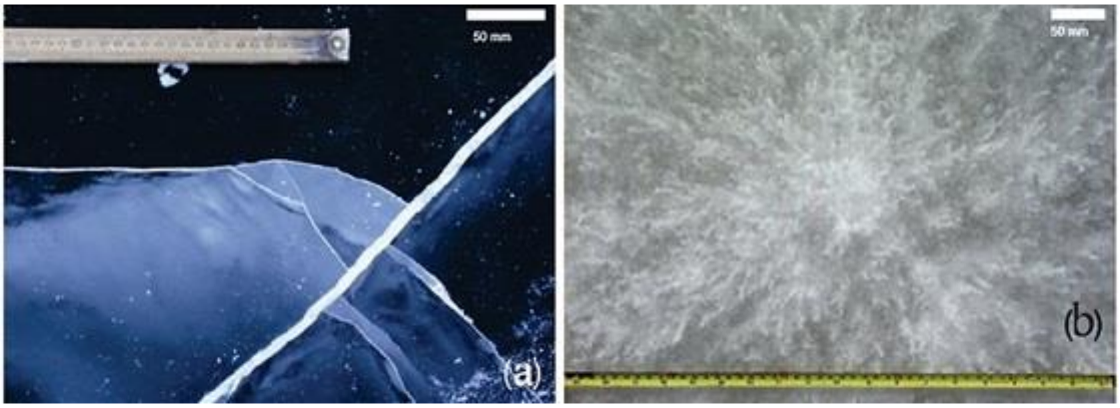

Figure 6 A close-up of internal microstructures in lake ice (a) and sea ice (b). Salt ions in sea ice makes it appear whiter and non-transparent. (Picture from Thomas and Dieckmann (2010a)).

Changes in ice temperature cause changes in microstructures, volume fractions of solids and brine, salinity, porosity and chemical composition (Thomas & Dieckmann, 2010a), and therefore influence the propagation of seismic energy and the materials mechanical strength. Anderson and Weeks (1958) did laboratory tests on ice and found that very cold sea ice (below -20 °C) is stronger than fresh water ice as salts become solid and serve as binding materials rather than flaws at such low temperatures. Timco and Weeks (2009) did measurements of Young's modulus in first-year ice using seismic methods. They estimated values of Young's modulus from both flexural waves and volume waves. They found that the physical strength of first-year sea ice to a large extent depends on the way of growth and type of dominating internal structures. As flexural strength depends on so many factors, it is difficult to say how much each factor influences it. Timco and Weeks (2009) found different values of Young's modulus from using flexural waves in the estimate compared to using volume waves, with values ranging between 1.7 and 5.7 GPa when estimated from volume wave propagation, and 1.7 and 9.1 GPa when estimated from flexural waves. Similar estimates based of P and S-wave velocities performed by Ewing et al. (1934a) gave a value of 9.17 GPa. The derivation and more details on Young's modulus is found in **Appendix A**.

Young's modulus, E, defines the relationship between stress, σ, excerted on the material, and strain, ε, caused by the working stess. It is defined as (Turcotte & Schubert, 2014b)

$$E = \frac{\sigma}{\varepsilon}. \tag{2.4}$$

The thickness of sea ice is highly variable and different within the different growth stages. Young (first-year) ice in general is thinner than older (perennial) ice, but deviations are often caused by compressional deformation causing thicker ridges or extensional deformation causing thinner areas (Thomas & Dieckmann, 2010b). Perennial ice is more exposed to compression, extension and local melting during the summer than first-year ice and therefore the thickness distribution is often smoother in first-year ice. Because abrupt changes in thickness can cause spreading of wave energy, they are sources for noise to seismic data (Thomas & Dieckmann, 2010b) and it may be beneficial to perform seismic on first-year ice.

2.3.1 Deformation mechanisms in saline ice

Several deformation types are possible in different materials, depending on properties and composition. Elastic deformation is reversible where strain returns to zero as stress is released. Plastic deformation, on the other hand, is permanent and strain is irreversible. A third deformation mechanism is the viscous type, where strain is permanent, but the strain rate is depending on stress over time (Fossen, 2010, p. 104). Thus, viscous stress may be expressed as $\sigma = \eta \frac{d\varepsilon}{dt}$, where η is viscosity (Elias, 2008). Usually, the perfect elastic state is described by the motion of a spring, while a damper describes perfectly viscous materials. Perfectly plastic materials deform by brittle, permanent strain, and are often presented by a rigid block resisting deformation until a critical stress is reached (Fossen, 2010). Materials found in nature are mostly not following just a single mechanism of deformation, but combinations of two (or more) of them.

Saline ice is a type of material where strain is partially reversible and deformation does not usually occur as brittle failure. In other words, portions of the strain diminish when stress is removed from the ice (Turcotte & Schubert, 2014a). However, ice has viscosity and the ability to resist flow in addition to its elasticity (Thomas & Dieckmann, 2010a; Vincent, 2012). Also, ice may deform plastically and strain may be permanent without being brittle (Feltham, 2008). This means that oceanic ice is neither a perfectly elastic, plastic, nor viscous material, but rather a combination of these mechanisms. Depending on the scales of time and volume, sea ice may be considered as either viscoelastic or viscoplastic (Squire & Allan, 1980; Feltham, 2008).

At macroscopic scales, a viscous-plastic model is an option for large-scale sea ice behavior (Feltham, 2008). Viscoplastic materials are known as Bingham materials, which will flow as perfectly viscous fluids above a certain stress. Whenever the stress is below this level, there will be no deformation in the material (Fossen, 2010, pp. 99-109). The model assumes that apparent stationary ice is actually in motion by very slow flow or creep, and hence the viscosity is of importance (Feltham, 2008).

However, in the case of flexural waves in ice, deformation will be at microscale, causing motion of particles at much smaller scales than considered above. Here, a viscoelastic model is more suitable to describe deformation (Squire & Allan, 1980). Whenever a material has a viscosity, deformation and rebound takes longer time than in purely elastic materials and one can say that the strain rate is time dependent (Fossen, 2010, pp. 99-109). Viscoelastic materials will dissipate heat due to energy absorption from the viscosity, making parts of the strain permanent. For comparison, dissipation does not occur in perfectly elastic materials (Thomas & Dieckmann, 2010a). **Figure 7a** shows how linear viscoelasticity gives a linear relation between stress and strain rate, and that the viscosity is the proportionality constant between them. This is a stage of deformation known as Kelvin-Voigt viscoelastic behavior, where both elastic and viscous properties work simultaneously (Fossen, 2010, pp. 99-109). However, this fairly simple model does not allow for stress relaxation over time, as is present in most materials (Mainardi & Spada, 2011).

Viscoelastic motion may also be described by the Maxwell model, where strain accumulates from the moment stress applies. This is shown in **Figure 7b**, where it's seen that strain is initially elastic and reversible, but after some time has passed, it becomes viscous and permanent (Fossen, 2010, pp. 99-109). This means that viscoelastic materials behave as elastic at a short time scale, and as viscous fluids at longer time scales (Turcotte & Schubert, 2014b).

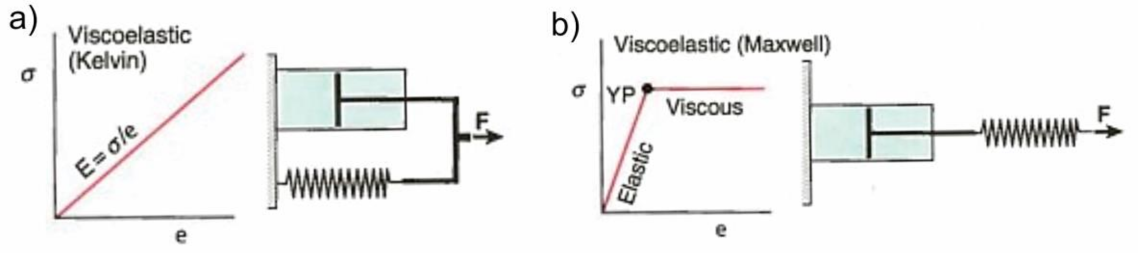

Figure 7 a) Kelvin-Voigt viscoelastic behavior of materials. The spring and damper are connected parallel to each other. Deformation is reversible and elastic and viscous at the same time. b) Maxwell viscoelasticity. Strain is elastic at first and viscous after the point of yield pressure (YP). The spring and damper are connected in a series. (Figure is modified from Fossen, (2010)).

A good way of modelling viscoelastic deformation in sea ice is by a combination of the Kelvin-Voigt and Maxwell model, also called Maxwell-Voigt model. This connects an elastic part and a viscous part of the strain rate, implying that the total strain rate is the sum of strain rate in a viscous fluid and the time derivative of elastic strain in a solid (Fossen, 2010, pp. 99-109; Squire & Allan, 1980; Turcotte & Schubert, 2014b). Turcotte and Schubert (2014b) defines the total stress in a linear viscoelastic model as

$$\frac{d\varepsilon}{dt} = \frac{1}{2\eta}\sigma + \frac{1}{E}\frac{d\sigma}{dt}. \tag{2.5}$$

Again, η is the viscosity of the fluid, σ is stress and E is Young's modulus. The first term on the right-hand side of Eq. (2.5) is therefore the strain in the viscous fluid, while the last term is the time derivative of strain in the elastic solid. Time derivatives are included due to the change in stress over time in viscoelastic materials (Turcotte & Schubert, 2014b). Laboratory tests on fresh water ice and in-situ tests on sea ice implies that this is a proper way of describing the deformation of sea ice (Squire & Allan, 1980).

2.4 Seismic wave modes related to floating ice

The floating ice is the origin of the strong, coherent dispersive wave masking the reflections from depth (Henley, 2004), where high reflection coefficients along its top and base make most of the energy generated at the source propagate as internally guided waves. The reflection coefficient is the difference in acoustic impedance between the upper and lower lithology at an interface, affecting the amount of energy reflecting off of the interface. It is defined as $RC = \frac{Z_2 - Z_1}{Z_2 + Z_1}$, where $Z_1 = \rho_1 v_1$ and $Z_2 = \rho_2 v_2$ are acoustic impedances above and below the reflector (Milsom & Eriksen, 2011b).

When most energy propagates within the ice, less energy propagates through the water and seabed sediments, and it follows that the flexural wave from the ice will have a much higher amplitude than the primary reflections from the seafloor. The flexural wave will not be a problem where the ice is in contact with land/sediments below due to the significantly reduced vertical motion in underlying sediments compared to a fluid (Barr et al., 1993). The most flexural noise is registered in the ice transition zone from land based ice to free floating ice (Lansley et al., 1984). As flexural waves often have larger amplitudes than the reflections, reflections may be difficult to identify. From Del Molino et al. (2008), measured amplitudes indicate that flexural waves usually have magnitudes of 40-60 dB higher than the reflections.

Lamb was among the first ones to discover and work on the concept of guided waves within plates, and thus such waves are sometimes termed Lamb waves (Lamb, 1916). Several types of waves arise and interfere with each other within floating ice. A study of waves in lake ice performed by Ewing, Crary and Thorne (1934a, 1934b), showed that different kinds of waves register in differently oriented seismographs as they cause particle displacement in different directions. Possible waves are, among others, the flexural wave, Rayleigh wave and the longitudinal wave (Ryden et al., 2003). Rayleigh waves (R-waves) are surface wave propagating along interfaces between solids and air (Gelius & Johansen, 2012). Longitudinal waves (P-wave) propagate by alternating compressions and dilatations of the entire volume, which means they are dependent on the bulk modulus and density of a material. In addition, shear waves (S-waves) may propagate in ice as it is a solid with the ability to hold shear strain. They cannot propagate in fluids as the shear modulus of fluids is zero (Worden, 2001). Details on bulk modulus and shear modulus can be found in **Appendix A**, and the equations of P and S-waves are derived in **Appendix B**.

2.4.1 The flexural wave

Lamb waves are guided waves within plates that arise with interference of different modes of reflected P and S-waves (Rovetta et al., 2009), where the particle displacement is both in the direction of wave propagation and normal to it (Del Molino et al., 2008). Lamb waves are divided into two types, the symmetric and the anti-symmetric mode, where the anti-symmetric mode is known as the flexural mode and the symmetric mode is sometimes called the extensional mode (Del Molino et al., 2008).

Flexural waves are volume waves with a retrograde particle motion (Gelius & Johansen, 2012; Worden, 2001). They are dispersive in nature, which means that their velocities are depending on frequency relative to plate thickness. Both the symmetric and the anti-symmetric wave propagation depend on the plate thickness, the angular frequency, the wavenumber and the P and S-wave velocities (Gomez, Fernandez & Garcia, 2011). Lamb derived the dispersion relations for symmetric and anti-symmetric Lamb waves propagating through a plate, which are given by (Lamb, 1916; Worden, 2001)

$$\frac{\tan\left(q\frac{h}{2}\right)}{\tan(p\frac{h}{2})} = -\frac{4k^2pg}{(q^2-k^2)^2} \tag{2.6}$$

and

$$\frac{\tan\left(p\frac{h}{2}\right)}{\tan(q\frac{h}{2})} = -\frac{4k^2pg}{(q^2-k^2)^2}. \tag{2.7}$$

Eq. (2.6) is the symmetric Lamb mode, whereas Eq. (2.7) is the anti-symmetric mode. In these equations, $p = \frac{\omega}{\sqrt{C_L{}^2-C^2}}$, $q = \frac{\omega}{\sqrt{C_T{}^2-C^2}}$, k is the wavenumber and the plate thickness is h. In p and q, ω is the frequency and C_T and C_L are the transverse and longitudinal wave velocities, and C is the phase velocity at a given frequency. From the definitions of p and q it is seen that the velocity is a function of frequency, indicating that both symmetric and anti-symmetric Lamb waves are dispersive (Worden, 2001).

Both symmetric and anti-symmetric Lamb waves may have an infinite number of wave modes where the modes of lowest order are named *fundamental* modes (Del Molino et al., 2008). Especially the flexural wave mode has high energy compared to primary reflections, and therefore this is important in the approach of seismic on ice in the transition zone (Rovetta et al., 2009). In the general case of floating ice, both the symmetric and anti-symmetric mode may occur, but only the anti-symmetric one is relevant for the seismic data collected at Svalbard in 2013. This is because the anti-symmetric wave is more prominent in near-offset areas, as its phase velocity is lower than that of the symmetric mode. This was shown by Gomez et al. (2011) from simulating the behavior of guided waves in dispersive plates. **Figure 8** shows their plot of dispersion relations of simulated symmetric and anti-symmetric waves, indicated by the captions *S* and *A*, respectively. It becomes clear that the symmetric mode initially has a higher velocity compared to the anti-symmetric mode and therefore they do not interfere with each other at small offsets. This only applies for the fundamental modes in this case, indicted by subscript *0*.

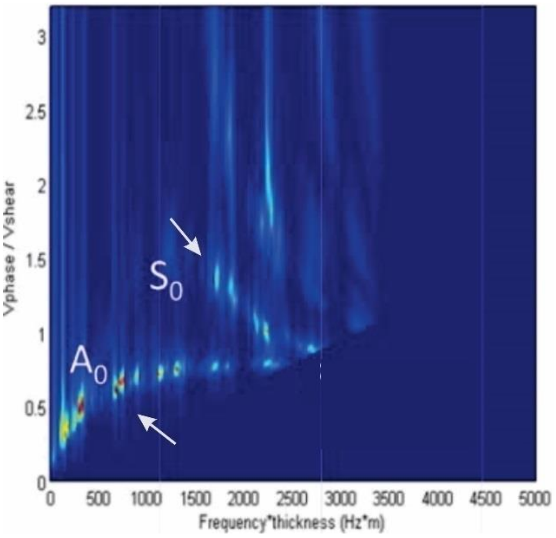

Figure 8 Dispersion relations for fundamental symmetric and anti-symmetric Lamb wave modes by Gomez et al. (2011). Y-axis has normalized velocities. (Figure is modified from Gomez et al. (2011)).

The way waves are generated in the survey at Svea allows only the anti-symmetric mode to arise. **Figure 9** illustrates how a vertical force (like the source used in the survey) generates mostly just anti-symmetric waves and how the symmetric waves would require a horizontal force to occur. Thus, it is likely that the wave seen in the seismic data from Van Mijenfjorden is the flexural mode, and the symmetric mode is not focused further on.

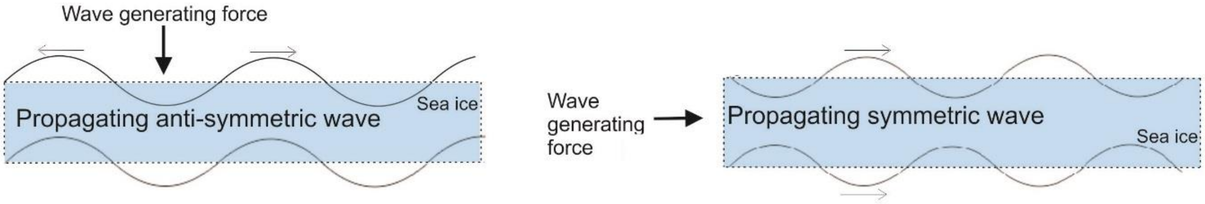

Figure 9 Illustration of how the generation of waves at Van Mijenfjorden causes mostly anti-symmetric flexural waves. The symmetric mode requires a force applied horizontally.

2.4.1 Receiver responses to seismic waves

A geophone placed on top of floating ice will respond to vertical motion caused by the (flexural) ice wave by generating a positive voltage in the positive vertical axis (Barr et al., 1993). P-waves moving upwards will register as positive particle motions, while downgoing waves will register as negative ones. The responding voltage generated in the geophone is proportional to the velocity along the top of the ice (Barr et al., 1993).

As ice is rigid, one can assume that the motion is the same along the top and the base of the ice and thus a propagating wave will cause a pressure in the water below the ice due to the vertical deflection. The hydrophones below the ice will sense the pressure variation in the water column and register it by generating a positive voltage in the opposite direction than that for the geophones. Thus, hydrophones will respond to positive pressure changes due to motion in the negative vertical direction (Barr et al., 1993), and one can say that the polarity is opposite to that of geophones.

Moving particles cause pressure changes and regardless of the direction of motion (upwards or downwards), the pressure in front of the moving particle will increase. Increased pressure registers as positive responses in hydrophones. This implies that geophones and hydrophones register upgoing waves with the same polarity and downgoing waves with opposite polarities (Rosales & Antonie, 2004; Septayana et al., 2010). As a wave passes by, the water pressure will vary about its steady state. The force exerted by the ice to the water is proportional to the product of mass and acceleration of the ice floe, and hence the pressure variations registered in the hydrophones are caused by the acceleration of the ice above (Barr et al., 1993).

2.4.2 Wave equations for waves in viscoelastic plates

The flexure of plates is a complex mechanism which may be described through a viscoelastic fluid loaded thin-plate model (Yang & Yates, 1994). It assumes a thin plate floating on a fluid of infinite depth, in which a wave is propagating. The thickness of the plate is smaller than the wavelength of the propagating wave. The equation describing flexure of plates as a response to a seismic source derives from the stress-strain relationship and the stiffness of thin plates (Squire & Allan, 1980). To derive the equation in three dimensions, we start by describing the motion in one spatial dimension and then expand it into the three dimensions of the plate.

When considering waves in a plate structure, Eq. (2.2) has to include all three spatial dimensions. Henceforth the displacement becomes $u = u(x, y, z, t)$. To simplify, we define a spatial vector $\boldsymbol{r} = (x, y, z)$, and the 3D equation of motion becomes (Pujol, 2003b)

$$\nabla^2 u(\boldsymbol{r}, t) = \frac{1}{c^2}\frac{\partial^2 u(\boldsymbol{r}, t)}{\partial t^2}. \tag{2.8}$$

Here, ∇^2 is the second order partial derivative of u with respect to x, y and z. A more detailed derivation is given in **Appendix B**.

Based on Eq. (2.8) and the required balance of working torques, the equation describing bending motion is found as (Wangen, 2010)

$$\frac{Eh^3}{12(1-\nu^2)}\frac{d^4u}{dx^4} = q(x), \tag{2.9}$$

where E is Young's modulus, h is the plate thickness, v is Poisson's ratio and u is the deflection of the plate as a response to an applied surface load, $q(x)$.

Taking into account the force exerted on the ice by the underlying fluid, deflection becomes

$$\frac{Eh^3}{12(1-\nu^2)}\frac{d^4u}{dx^4} + \Delta\rho g u = q(x). \tag{2.10}$$

The rigidity of the plate can be written as $D = \frac{Eh^3}{12(1-\nu^2)}$. Furthermore, $q(x) - \Delta\rho g u$ is the total vertical stress at the plate, where $\Delta\rho g u$ is the upwards push from the water below (Wangen, 2010).

Laboratory tests and in-situ tests show that the Maxwell-Voigt model describes motion in sea ice most accurate with deformation distributed between one elastic and one viscous component (Squire & Allan, 1980). From the definition of viscous stress $\left(\sigma = \eta \frac{d\varepsilon}{dt}\right)$, it is intuitive that the equation describing viscoelastic flexure has to include the time derivative of the deflection. The equation describing bending of a viscoelastic plate becomes

$$D\frac{\partial^4 \dot{u}}{\partial x^4} + \Delta\rho g \dot{u} + \Delta\rho g\frac{u}{t_e} = \dot{q} + \frac{q}{t_e}. \tag{2.11}$$

This time, $D = \frac{Eh^3}{12}$ is the rigidity of the plate. The dot above any variable denotes its time derivative. For sea ice, $\nu \approx 0.3$ so $(1 - \nu^2) \approx 1$ and the dependence on Poisson's ratio can be neglected. The reader is referred to **Appendix C** for more details on the derivation.

Eq. (2.11) makes a basic model for flexural wave propagation in a layer of floating ice. The equation contains both the elastic and the viscous components of deflection and time derivatives due to viscous properties. When the viscosity is zero, Eq. (2.11) is a purely elastic equation. Similarly, when elastic properties are zero, the equation is purely viscous (Wangen, 2010).

2.5 Processing and analysis of floating ice seismic data

Flexural and longitudinal waves are of different velocities and may therefore be separated based on their different arrival times (Yang & Yates, 1994). However, flexural waves have varying properties throughout their propagation and thus they overprint other wave modes. Conventional seismic processing is therefore of little help to reduce the flexural wave in floating ice seismic data. Simple filtering is generally acceptable for removing random noise, but the broad frequency spectrum of the flexural wave makes it difficult to leave the wanted reflections behind. Because the amplitudes of flexural waves are large and because of their dispersive nature, flexural noise components are among the most difficult types to remove/attenuate. The relatively low amplitudes of reflections makes it additionally difficult to enhance these, even if they are possible to identify (Henley, 2004). Separation of noise and signal is not easily done by todays processing methods and thus it is considered necessary to find new methods to overcome the challenges (Del Molino et al., 2008). Several authors (Henley, 1999; Jensen, 2015; Jensen, 2016; Septayana et al., 2010) have already attempted new techniques to cope with these challenges. Processing in different domains have been tested, but mostly on synthetic data. In general, methods seem to work relatively good on synthetic data, but they are not as efficient on real data as many unexpected factors may influence on wave propagation here.

As flexural waves are difficult to remove, they may rather be utilized to study ice mechanics. Different mechanical and physical properties may be estimated from the study of waves generated in relation to, and propagating through, ice. Data may be explored and analyzed by different techniques in order to identify and study the flexural wave and its frequency content.

Other wave modes may be identified through such analyses as well. Following is an overview of possible techniques and how they may provide information about ice characteristics.

2.5.1 The f-k domain

The f-k domain can be obtained from the x-t domain by a 2D Fourier transform (Michaels, Michaels & Ruzzene, 2011). The transform maps straight lines from the x-t domain as straight lines in the f-k domain. The difference between them are their slopes and the f-k domain is therefore effective in reducing coherent linear noise (Adizua et al., 2015). Due to dispersion, the flexural wave is non-linear in the f-k domain and the f-k transform may not be optimal for this purpose. However, viewing data in the f-k domain may contribute to a better understanding of different wave modes and how they are related to ice properties. This is discussed further in the **Method** chapter.

F-k filtering was tested on the data from the 2013-survey at Svalbard by Jensen (2015) and Jensen (2016). Depending on the amount of flexural waves, f-k filtering had varying efficiency. Jensen (2015) did filtering on both hydrophones and geophones based on the velocity of acoustic waves in water (1500 m/s), a chosen flexural velocity of 180 – 700 m/s, and velocities of primary reflections exceeding the velocity of water and flexural waves. The author performed filtering between -1500 m/s and 1500 m/s to cancel the water wave and the flexural wave. The effect was documented by estimating the signal-to-noise ratio based on the amplitudes of flexural waves and primary reflections before and after filtering. The conclusion was that f-k filtering attenuates the flexural wave in most cases, but it cannot cancel the noise completely and does not enhance any reflections in the area masked by flexural waves.

2.5.2 The autocorrelation function

When a random function is correlated with a time shifted version of itself, one may define an autocorrelation function. A seismic signal may be represented by a *stochastic process* rather than just one deterministic function. Thus, the autocorrelation function for a stochastic process, $G(t)$, is defined as (Peebles, 2001a)

$$R_{GG}(t, t+\tau) = E\{G(t)G(t+\tau)\} = R_{GG}(\tau). \tag{2.12}$$

Here, R_{GG} denotes the autocorrelation function of $G(t)$, $E\{\cdot\}$ is the expectation operator and τ is the time lag from the original stochastic process to a time shifted one. The process is assumed to be wide-sense stationary (its statistical properties do not change with time (Peebles, 2001a)), and thus it is time-independent so that t is not included as a variable in R_{GG}. The autocorrelation is symmetric for real valued processes, giving $R_{GG}(\tau) = R_{GG}(-\tau)$ (Peebles, 2001a). The autocorrelation function of a signal has its maximum correlation at zero time lag $(\tau = 0)$.

2.5.3 The cross-correlation function

The cross-correlation is a generalization to pairs of stochastic processes. For the two stationary stochastic processes $G(t)$ and $H(t)$, the cross-correlation function is defined as (Peebles, 2001a)

$$R_{GH}(t, t+\tau) = E\{G(t)H(t+\tau)\} = R_{GH}(\tau). \tag{2.13}$$

Above, R_{GH} denotes the cross-correlation between G and H for at time lag τ. As for the autocorrelation function, the processes are assumed to be mutually stationary and hence t may be disregarded in the cross-correlation function as well. The cross-correlation function is not symmetric about zero, hence $R_{GH}(\tau) \neq R_{GH}(-\tau)$ or $R_{GH}(-\tau) = R_{HG}(\tau)$ (Peebles, 2001a).

Normalized cross-correlations may be estimated to obtain a dimensionless correlation function. In normalized cross-correlations, the maximum and minimum correlation coefficients are 1 and -1 (White, 1969).

2.5.4 Frequency analysis and power spectral density estimates

A frequency analysis may be performed by a Fourier analysis in order to find the frequencies of a complex time domain signal. It defines the mathematical relationship between the time and the frequency domain. A signal is a series of measurements at different times, and during the Fourier analysis these measurements are transformed to a sum of several harmonic oscillations. These sinusoidal oscillations have different frequencies and make up the spectrum of the signal (Mastro, 2013).

The definition of the Fourier transform is (e.g., Hanssen, 2003)

$$\hat{G}(f) = \mathcal{F}\{G(t)\} = \int_{-\infty}^{\infty} G(t)e^{-j2\pi ft}dt, \tag{2.14}$$

where $\hat{G}(f)$ is the Fourier transform of $G(t)$ and $\mathcal{F}$ is the Fourier operator. The inverse operation is possible and transforms the frequency domain signal back to the time domain. This is the Fourier synthesis given by (e.g., Hanssen, 2003)

$$G(t) = \mathcal{F}^{-1}\{\hat{G}(f)\} = \int_{-\infty}^{\infty} \hat{G}(f)e^{j2\pi ft}dt, \tag{2.15}$$

where $\mathcal{F}^{-1}$ is the inverse Fourier operation.

Studying the frequency content of signals may, for example, be done through power spectral density estimates. It reveals how the power of a signal is distributed between its different frequencies. For random and nondeterministic processes, a Fourier transform will not normally exist as such processes are not absolutely integrable due to their infinite oscillation. Therefore, one aims to describe and analyze the signal in terms of its power as a function of frequency. Such a function is known as the power density spectrum and may exist for random processes (Peebles, 2001b). It is obtained by defining a finite, truncated version $G_T(t)$ of the stochastic process $G(t)$ such that $G_T(t) = \begin{cases} G(t); & -T < t < T \\ 0; & \text{elsewhere} \end{cases}$ (Hanssen, 2003; Peebles, 2001b).

$G_T(t)$ has an existing Fourier transform and its power spectral density as a function of frequency can be expressed as (Hanssen, 2003)

$$S_T(f) = \lim_{T\to\infty} \frac{E\left[\left|\hat{G}_T(f)\right|^2\right]}{2T}. \tag{2.16}$$

Using Eq. (2.14) in Eq. (2.16) gives the power spectral density of the stochastic process $G(t)$ as (Hanssen, 2003)

$$S_{GG}(f) = \lim_{T\to\infty} E\left[\frac{1}{2T}\left|\int_{-T}^{T} G(t)e^{(-j2\pi ft)}dt\right|^2\right]. \tag{2.17}$$

The power spectral density is symmetric about zero for real signals, $S_{GG}(f) = S_{GG}(-f)$ (Peebles, 2001b). As a consequence, only the positive frequencies will be plotted in the estimated power spectral density plots in the **Results** chapter.

In reality, the recorded signals are functions/realizations of one stochastic process. Signals are truncated and discretized due to the sampling in time. This makes it difficult to estimate the true spectrum of the signal. Spectral estimates, S_{GG}, are continuous functions, making it difficult to perform the estimate from a discrete realization. In contrast to the spectral estimate function, the realization of the process is a truncated/finite function, again making the estimate difficult as we cannot use a finite function to express something infinite (Hanssen, 2003).

Standard methods for estimating the power spectrum of a signal are often used, for example the periodogram and the modified periodogram. Such methods are simple and may cause inaccurate estimates due to the assumptions and simplifications made (Hanssen, 2003). Better and more precise alternatives exists, among them the *multitaper* technique which was first proposed by Thomson (1982) based on ideas of Slepian (1978). The method was developed as an alternative to overcome limitations of the standard discrete Fourier analysis.

Performing conventional frequency analysis of a signal will lead to a power spectrum with great variance. This problem is reduced when several tapers are used (hereby the name “multitaper”) (Thomson, 1982). Tapers are data windows defining at what intervals of the signal the frequency analysis is performed. Spectral leakage from the spectral maxima is another problem in conventional techniques, and side lobes occur around the signals central frequency. Leakage is often caused by the limited area by using only one taper (Percival & Walden, 1993).

The multitaper method combines multiple tapers of different sizes and in different time intervals along the signal. Doing this provides higher energy/amplitudes of the signal, but enhances the amplitude of “leaked” frequencies as well. The amount of leakage and variance is different for each taper and an average of them is computed (Percival & Walden, 1993; Thomson, 1982; Van Drongelen, 2007). The variance is reduced when computing the average power spectrum. With multiple windows, the width of the main lobe of the frequency response increases. A wide lobe means poor frequency resolution and therefore difficulties in separating close spaced events. Thus, the multitaper method has a tradeoff between variance reduction and spectral resolution (Hanssen, 2003). The main goal of the technique is to find the number of tapers and their weighted average giving as little variance and leakage as possible, along with high energy and good resolution (Thomson, 1982). Comparison of estimates from the multitaper and other spectral estimate methods show that the amount of leakage and variance is less and that the frequency resolution is better in this method compared to the standard techniques (Bronez, 1992).

3 Data

Data examined in this study are collected at the fjord ice cover in the inner parts of Van Mijenfjorden on the south-west coast of Svalbard. Data from this location are a fairly good representation for data from Arctic first-year sea ice where properties like temperature, salinity and internal growth structures are similar. The seismic exploration took place between the 13th and 16th of March 2013. The data include signals from both hydrophones and geophones.

3.1 The site and its surroundings

Van Mijenfjorden is about 70 km long and almost closed off at its mouth by the island Akseløya. In **Figure 10** we show a map where the location of exploration is indicated by the blue star. Akseløya shields the ice cover from winds and ocean currents and its presence leads to relatively steady and long-lasting ice within the fjord. This makes it possible for the ice to remain from December until July if weather conditions and temperatures permit it (Høyland, 2009). The fjord is divided into an outer and inner basin. The ice cover is usually thickest in the inner basin due to less movement of the water. The oceanic flux in Van Mijenfjorden is dominated and primary caused by the tidal currents. The effect of the tides is largest in the outer basin, leading to a flux close to zero within the inner basin. This means that there is little stress along the margins of the ice and internal deformation gives minimal effect to potential seismic data. This is also the part of the fjord that freezes first, usually in early winter season (December-January) (Høyland, 2009).

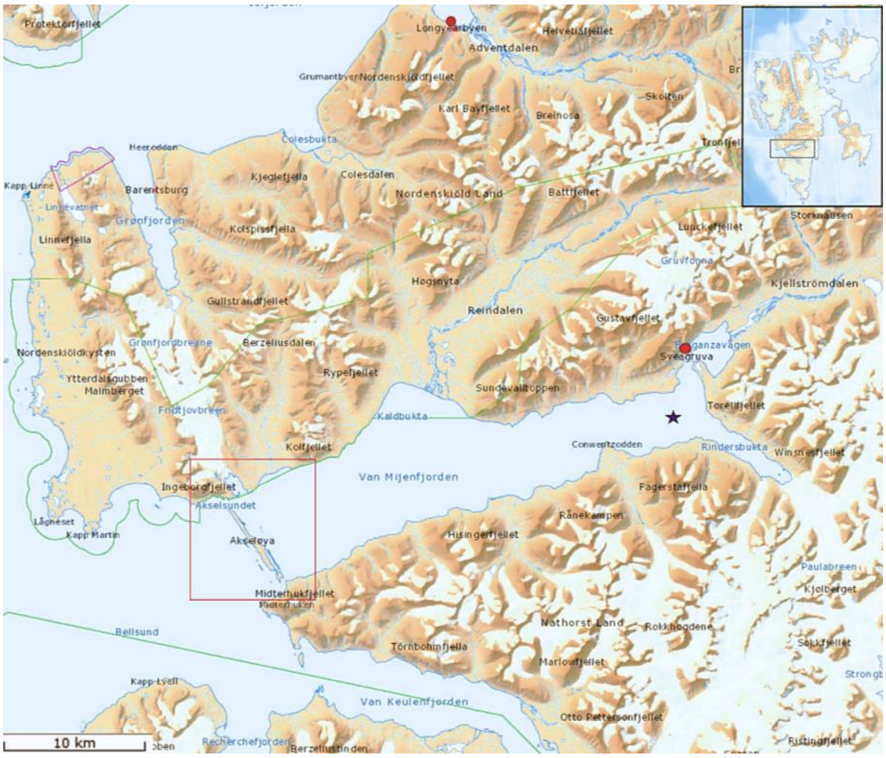

Figure 10 Map view of Van Mijenfjorden. Akseløya is indicated at the mouth of the fjord. The blue star close to Sveagruva (red dot), indicates the position of the seismic exploration. (Map found at http://toposvalbard.npolar.no/).

3.1.1 Oceanography, climate and ice cover

The character of floating saline ice depends greatly on weather conditions, currents and waves. These are ever changing factors causing the ice conditions and character to differ each year (Høyland, 2009). Seismic explorations are most appropriate in uniform ice with minimal deformation structures as it gives less internal scattering of energy. Thick ice is more difficult for winds and currents to deform, and therefore thick ice is generally more even and uniform than thin ice. As the inner basin constitutes thick and relatively steady ice, this is probably the best location to collect seismic data within Van Mijenfjorden.

A comprehensive study of the fjord ice of Van Mijenfjorden across several years was performed by Høyland (2009). Measurements show that ice thickness during one season depends on temperature and ice growth period. For example, the peak thickness at 1.28 m in 2004 is the largest thickness measured within this fjord during the 8 years-period from 1998 to 2006 of Høyland’s study. In 2004, the ice grew until April before melting started. On the contrary, 2006 had the minimum peak thickness with only 0.72 m of ice (Høyland, 2009). Temperature data from 2006 confirm that this winter was warm compared to others (Meteorologisk Institutt, a). The ice cover of Van Mijenfjorden is comparatively larger than other fjords in Svalbard, probably due to the barrier at the fjord entrance. However, smaller thickness variations within the fjord itself is observed. These may be explained by local variations of snow on the ice, where local winds give higher accumulation of snow in the southern parts of the fjord and the ice may grow faster and thicker here (Høyland, 2009).

A gradual warming of the West Spitsbergen Current since the year of 2004 might be part of the explanation for less fjord ice in the outer basin of Van Mijenfjorden during the last decade. Even though air temperatures have been well below freezing point and drift ice has been present, no fast ice cover occurred (Høyland, 2009). In general, the Arctic summer is observed to be prolonged, resulting in a shorter period of fjord ice and a decrease in the number of fjords covered by ice (Elverland & Norsk Polarinstitutt, 2008).

During the days of acquisition in March 2013, average air temperatures at and around Svea varied from about -25 °C to -14 °C. **Table 1** shows maximum, minimum and average air temperatures, in addition to the wind speed at mid-day. During the days before the exploration, air temperatures were about the same as during the exploration, hereinafter a relatively steady ice temperature is reasonable.

Table 1 Weather at Svea at the time of acquisition. Temperatures and wind speed are measured at the weather station of Sveagruva, 9 m a.s.l. Data from Yr (NRK & Meteorologisk Institutt) .

Date	Test	Max. air temp.	Min. air temp.	Avg. air temp.	Wind speed, mid-day
Day 1 13.03.13	Test 1 (shot A)	-20.6 °C	-28.8 °C	-24.0 °C	1.4 m/s from NNE
Day 2 14.03.13	Test 1 (remaining)	-17.4 °C	-23.6 °C	-19.0 °C	1.3 m/s from NE
Day 3 15.03.13	Test 2	-14.2 °C	-20.6 °C	-15.7 °C	7.3 m/s from NE
Day 4 16.03.13	Test 3 and 4	-10.6 °C	-18.0 °C	-13.9 °C	9.7 m/s from NE

Seismic explorations in fjords often give reflections from the sides of the fjord, which disturbs the reflections from the seafloor and deeper sediments. In Van Mijenfjorden, the water depth was measured through hydrophone boreholes and ranges between 50 and 60 m with an average of 56.5 m. As water depth is small compared to the several kilometers width of the fjord, any reflections from the sides in the fjord will arrive much later than the primary reflections from the seafloor. In other words, side reflections in the fjord is probably not a major problem in these data. However, the sides of the fjord will cause flexural waves to travel back and forth within the ice, but these will not interfere with the primary flexural wave at near-offset receivers and at short sampling times.

Different growth mechanisms of sea ice lead to different internal structures. Studies of ice from Van Mijenfjorden in thin sections reveal that the internal structures are mostly columnar (Høyland, 2009). Columnar ice typically occurs in first-year ice and is dominating in the Arctic environment. Columnar ice usually forms when new ice grows below an existing ice floe, in other words along the base of an ice cover (Thomas & Dieckmann, 2010a).

The fjord ice of Van Mijenfjorden is usually thick (compared to other fjords on Svalbard) and uniform, with little or no internal deformation structures from external marginal stresses. Even though if the ice were to crack and break into pieces, it would most likely freeze back into its original position due to the limited possibilities to move around in the (almost) closed off fjord (Høyland, 2009). During the seismic acquisition in March 2013, ice thickness was measured in several boreholes. The average ice thickness in the inner basin of Van Mijenfjorden was 76 cm.

3.2 Description of survey

Explosives generated the energy at the source in the survey. Several shots from five different points (at different source-receiver offsets) were fired. Both point and line sources were applied. Line sources were either double or single detonating cords, 12.5 m or 25 m long. The point sources had 0.5 kg, 1.0 kg and 2.0 kg of explosives.

Geophone data were achieved from two different receiver arrays with different orientations relative to the source points. The recording time for the survey was 8 seconds with a sampling interval of 1 ms such that there are 8000 samplings per trace. The two arrays of geophones (named L1 and L2) had 120 receivers each and were located perpendicular to each other. The 120 geophones were connected to 60 nodes along L1 and L2. The spacing between each receiver was 6.25 m, which means that the arrays were a total of 750 m long. The distance from the first receiver to the source varied, where the shortest offset was 25 m and the longest one was 1025 m. Three of the five source points were parallel to the L1-array. The fourth was at an angle to both L1 and L2, while the fifth was perpendicular to L1 and parallel to L2. See **Figure 11** for a visualization of the geometry. The exploration was carried out in four different tests, where source type and charge, and type of geophones (strings or points) varied. The different seismograms indicate that the registered energy mostly falls within the 2-3 first seconds after the detonation. This means that the sampling interval of 8 seconds is long enough to cover all the interesting reflections and flexural waves.

Hydrophone signals were collected by an array of 30 hydrophones placed 1 m, 5 m, 10 m and 20 m below the ice surface. These were connected to the surface receiver-nodes through boreholes and covered the near half of the L1-array. Hydrophones were point receivers, corresponding to every second geophone at the surface. Two geophones and one hydrophone were connected at a node and thus there were twice as many geophones as hydrophones and the distance between each hydrophone was 12.5 m.

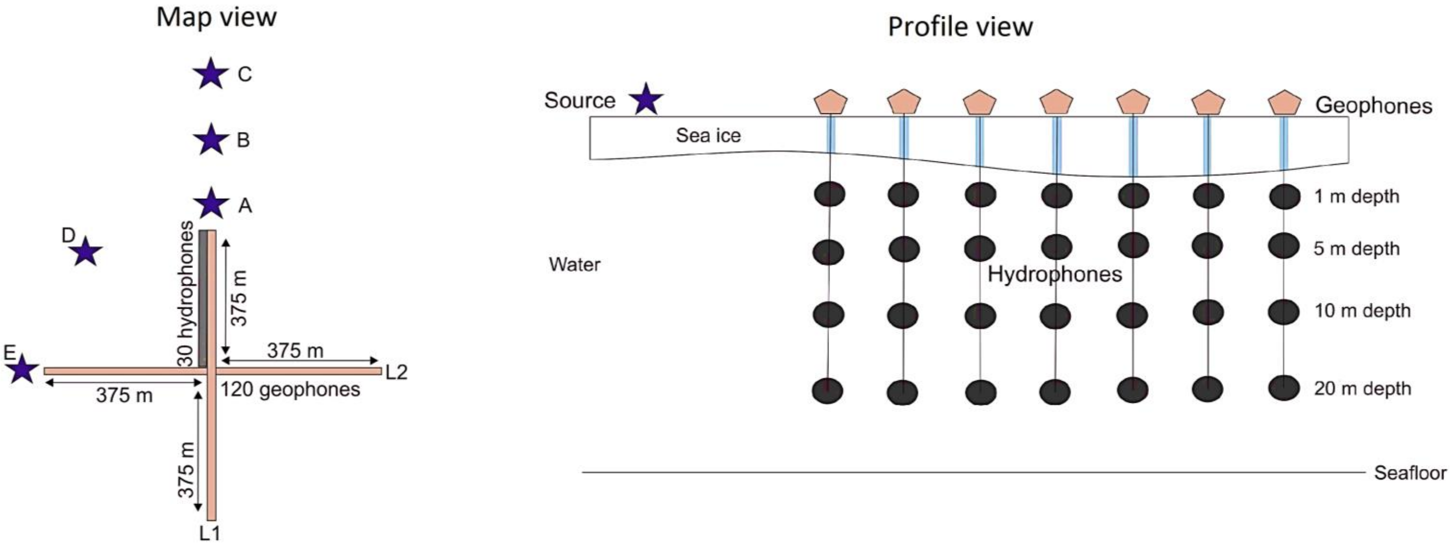

Figure 11 Map and profile view of acquisition at Van Mijenfjorden, Svalbard in 2013. Blue stars mark shot points, beige receivers are geophones while grey ones are hydrophones. L1 and L2 corresponds to the two geophone-arrays explained above.

3.2.1 Receiver types

The geophones used in the survey at Van Mijenfjorden in 2013 are of the type SM-4 produced by the company Sensor (now a part of Ion), and are designed for use both on land and in water (at the seafloor) in 2D and 3D acquisitions. They have a natural frequency of 14 Hz (± 5%) (Ruud, B. O. Personal communication, 2017).

The hydrophones are of the type P44-A produced by Mark Products, a company which is now a part of the larger company Sercel. These hydrophones are designed for use in the transition zone from land to deep water, or as OBC (ocean bottom cables). They work to a depth of 75 m, which makes them suitable for the conditions in Van Mijenfjorden. Their natural frequency is 10 Hz (± 15 %) (Ruud, B. O. Personal communication, 2017).

Because the natural frequencies of these receivers are different, one has to correct for this difference before any eventual combination of the two signals is possible. This is done by transforming both data types to a common natural frequency of 4 Hz. Because this is a much lower frequency than the original ones, low frequency flexural components are enhanced in the signals. Other low frequency components, like waves and tides, are enhanced as well, and it is a risk that the total amount of noise in the data is increased. However, if one wants to look at geophone and hydrophone signals simultaneously, this is a way to produce comparable quantities. This correction for different phase responses is a “dephasing” of the geophone converting it so that it matches the hydrophone. Band-pass filtering after dephasing is advantageous in order to remove some of the enhanced random noise and thus a zero-phase Ormsby band-pass filter (not affecting the phase such that no correction here is required later) designed by SeisLab is applied. Cut-off frequencies are 0-1 and 10-50 Hz. This means that frequencies between 0 and 1 Hz and between 10 and 50 Hz are gradually attenuated. Everything above 50 Hz is filtered out of the signal, and therefore broad-banded and high-frequent energy will not be present after filtering. A magnitude response and shape of the filter may be seen in **Figure 12**.

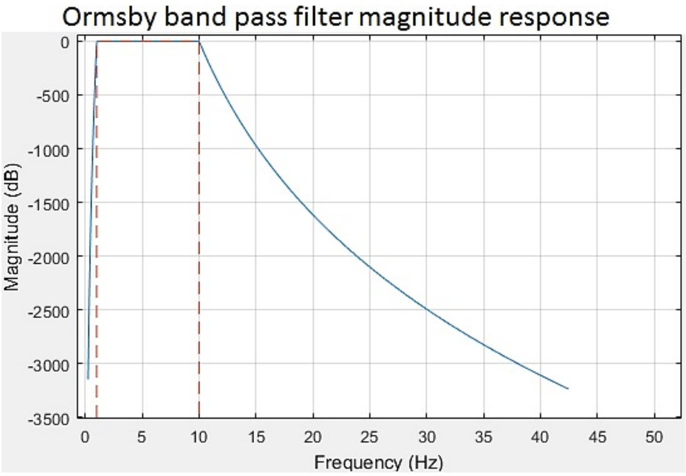

Figure 12 Filter response of the Ormsby band-pass filter applied after dephasing.

The enhanced amplitudes of flexural waves during dephasing and band-pass filtering indicate that flexural waves have frequencies below 50 Hz. Comparing geophone and hydrophone signals indicate that the flexural wave is, intuitively, stronger in the geophones. **Figure 13** shows the different amount of flexural noise in hydrophones (left panel) and geophones (right panel). The figure displays wiggle-plots after the corrections described above have been applied. The flexural wave is shaded in yellow, whereas the primary reflection and the air wave are blue and red, respectively.

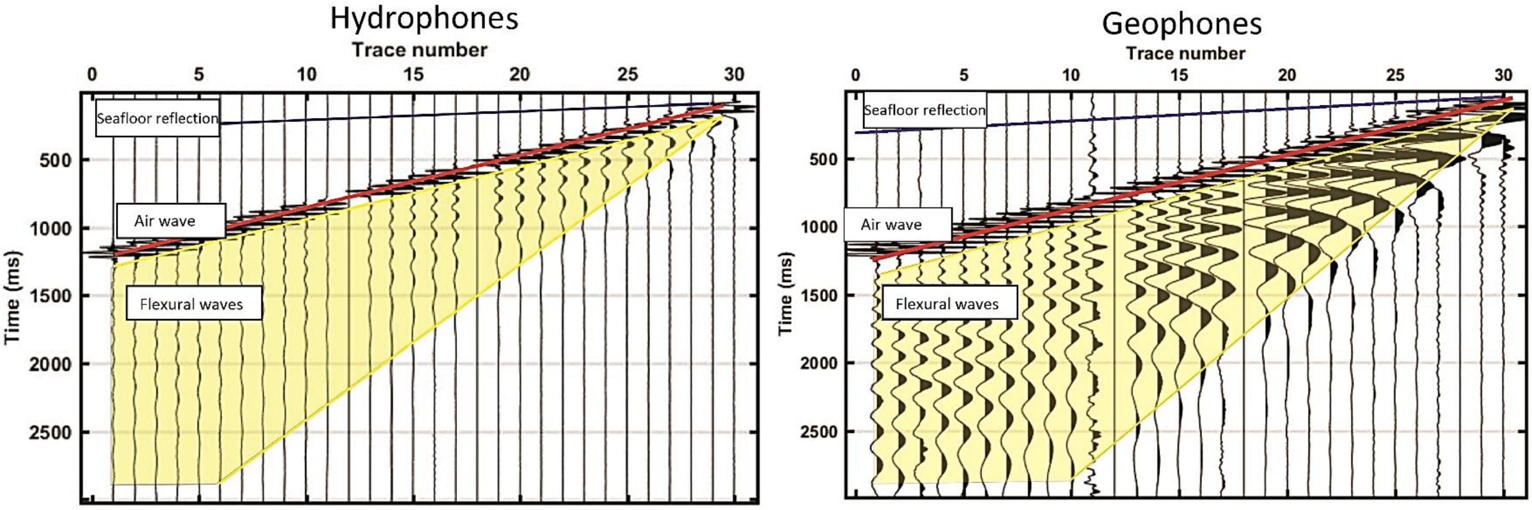

Figure 13 Flexural waves (yellow) in hydrophones (left panel) and geophones (right panel) at Van Mijenfjorden after the dephasing corrections. The seafloor reflection is indicated by the blue line while the air wave is red.

3.3 Description of data

The data from Svalbard have the SEG standard polarity where negative amplitudes correspond to positive (upwards) vertical motion in the geophones and positive pressure changes in the hydrophones (Brown & Abriel, 2014). Data are of various dimensions and resolutions, due to different numbers of receiver, different source-receiver offset, and different orientations of receiver arrays relative to the shot point. Some of the traces show more and/or clearer flexural waves than others. In particular, the geophones show the strongest flexural wave, while the deeper the hydrophones are located, the less flexural energy and the clearer the primary reflections. Below 5 m depth, hydrophones show no flexural noise. The maximum depth where we detect flexural waves is depending on the ice thickness. Because the number of hydrophones is only half the number of geophones, the resolution of geophone signals is higher than that of hydrophone signals. The geophones also cover a larger offset than the hydrophones and most of the analyses will be performed on geophone data.

The data show a very prominent air wave, as was seen in **Figure 13**, travelling directly from the source to the receivers. In the seismogram, the air wave arrives after the seafloor reflection due to its lower velocity. Its dip gives a velocity of about 340 m/s, which is approximately the speed of sound in air and confirms that it is the direct wave in air. Reflections and flexural waves are of low amplitudes and nearly invisible compared to the air wave and muting of it might be useful. Higher charges at the source causes higher amplitudes, but the relative sizes of different waves are unchanged. For double line sources, the direct air wave appears wider/thicker in the seismogram than for single line sources and point sources. A seismogram collected from a double line source is shown in **Figure 14**.

Examining the data collected throughout the different tests makes it possible to identify a few reflections arriving prior to the air wave and the flexural wave. A direct wave along the ice surface may be seen, followed by the seafloor reflection, a refracted wave and seafloor multiples – all indicated in **Figure 14**. The primary reflections are clear until they reach the area of interference with the flexural wave where they are overprinted by the relatively stronger flexural waves.

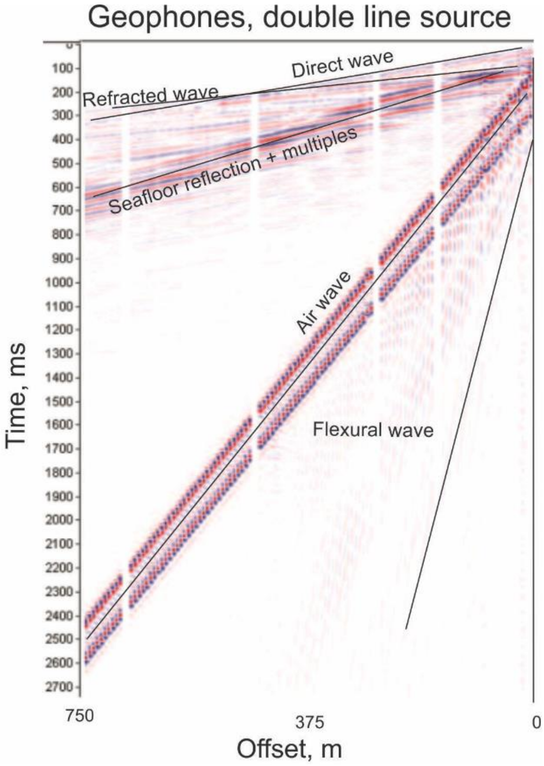

Figure 14 Geophone seismogram with different waves indicated. The air wave is broad as a consequence of the double line source (detonating cord).

The hydrophones at shallow depths (1 m) contain the air wave as well, but it quickly disappears with increasing depth. The fact that hydrophones are suspended from the ice and connected to geophones, makes motion along the surface displace the hydrophones as well. This is why the air wave shows up in the hydrophones, even though they are placed in the water. The hydrophones at greater depths (10-20 m) show no direct air wave and no flexural waves. Random noise from waves, currents and other oceanic conditions might still be present in hydrophones compared to geophones. However, an advantage with hydrophones below the ice is that they will not register the noise originating from operational equipment at the surface.

4 Method

The right combination of hydrophone and geophone data may improve the attenuation of the ice flexural waves. By looking at the frequency content of each signal, the frequencies of flexural waves may be identified. Several methods and procedures to perform such a combination has already been proposed and attempted by different authors. Therefore, we chose to focus on how different analyses and processing of the provided data may give information about the ice itself and how such information may be used for other purposes. Several operations, as explained in the following section, may give information about the frequency content and may thus be used to characterize the different components in signals.

4.1 Ice properties from autocorrelation functions

Autocorrelation functions at single receivers may be estimated to find properties of the material of wave propagation. Estimating the frequency content of the autocorrelation functions may help identify the frequencies corresponding to flexural waves (Gorbatov, Saygin & Kennett, 2013). As the band-pass filter used during the dephase-correction is a high-pass band-pass filter and enhances the flexural wave, the autocorrelations are estimated from the dephased signals. Geophone traces registered at different distances from the source are chosen for this purpose. From varying the distance from the source when estimating the autocorrelations and their frequency contents, one may be able to study how the ice related waves evolve with increasing propagation distance. Autocorrelation functions are estimated for both geophone and hydrophone traces, but as the geophones contain waves influenced by the ice alone, these are focused on in favor of the hydrophones. The waves registered in the hydrophones have propagated through both ice and water and ice properties alone may be difficult to recover.

4.2 Ice properties from cross-correlation functions

Cross-correlation functions are estimated from dephased signals as these give cross-correlation functions where dispersive envelopes are prominent and easily identified. Thus, it is easier to estimate properties of the flexural wave and the material properties of influence to the wave propagation. Cross-correlation functions are estimated at increasing distance from the source. This is done for both hydrophones and geophones, but mostly the geophones are focused on for the same reason as it was for the autocorrelations.

Cross-correlating closely spaced geophones might be performed to find the velocity of the propagating wave by identifying the time lag at which the two receivers are maximum correlated. This lag corresponds to the propagation time of the wave between the geophones (Winter & Bies, 1962). Because the offset between each receiver is knows, the velocity is easily calculated from $v = \frac{x}{t}$, where t is the propagation time ($t = \tau$) and x is the distance between the two correlated receivers. For a constant velocity, the wave is non-dispersive, whereas velocity changes as dispersive waves propagate (Winter & Bies, 1962). The cross-correlation function is estimated between every second geophone, 12.5 m apart, throughout the entire array of 120 geophones. The reason for not picking two neighboring receivers is that the spacing may be too short for the propagation time to be clearly identified by the cross-correlation. If the offset is smaller than the wavelength, an accurate time lag corresponding to propagation time may be difficult to estimate. However, too large offset may cause uncorrelated signals due to scattering and attenuation of energy with increasing offset (Marsan et al., 2012). Therefore, a receiver spacing of 12.5 m is considered reasonable.

4.2.1 Seismic interferometry

Seismic interferometry is a method that uses cross-correlations between two seismic receivers to say something about Earths properties. For seismic data from floating ice, such a method may be exploited placing an OBS (ocean bottom seismometer) at the seafloor and comparing its signal to the one registered at the surface. The cross-correlation gives a new trace where the apparent source is the OBS receiver. Note that this is not the actual source, but the signal registered in the geophone is propagating from the OBS and it seems like it is the origin of energy in the system. This leads to responses occurring prior to the OBS to be greatly reduced at the geophone and accordingly noise is reduced in the resulting cross-correlated trace. Cross-correlations may be used for estimating ice properties as well as Earth properties and as the Svea data contains many geophone signals with strong ice generated waves, they may be utilized by cross-correlation estimates in order to say something about the ice itself. In addition, as noise will attenuate as a consequence of cross-correlating OBS and surface receivers, the method may be suitable for attenuating the flexural waves. This will not be attempted here as no OBS signals are available, but it may be suggested for future work.

4.3 Frequency analysis and spectral estimates

Performing frequency analysis on data collected on floating ice may make it possible to identify the frequencies of different wave modes in the ice. Among them is the flexural wave component, where the frequency may be used to estimate the thickness and rigidity of the ice. Press et al. (1951) found very simple relations between wave frequency and ice thickness. However, as ice wave propagation is depending on several other factors in addition to the thickness, more complicated models including ice parameters are required to estimate a reasonable thickness. Performing accurate frequency analysis in form of power spectral density estimates and spectrograms will be performed in order to identify frequencies of the flexural wave to be used in a thickness estimate. The thickness estimate model is described in more detail in the next section.

4.3.1 Multitaper power spectral density estimate

As standard power spectral density estimate techniques are simple and inaccurate, the multitaper method introduced in **Ch. 2** will be used for the data analysis in this study. MATLAB has an implemented function performing this spectral estimate, in which one has to specify the time half bandwidth product, NW. This is the product between the length, N, of the signal and the bandwidth of it, 2W. NW determines the frequency concentrations and therefore affects the resolution of the multitaper estimate (Park, Lindberg & Vernon, 1987). As a rule of thumb, the discrete prolate spheroidal/Sleipan sequences (the tapers) used in the multitaper method are the first $2NW - 1$ sequences (Percival & Walden, 1993), which is the number of tapers implemented in MATLAB. As details in different parts of the spectrum are resolved with different numbers of tapers, the value of NW is varied to enhance different details of interest.

MATLAB also requires specification of the number of points to be used in the power spectral density estimate. This is set to MATLAB's default: "256 or the next power of 2 greater than the length of the signal" (The MathWorks Inc). For these signals, lengths are 4001 point (4000 ms + the zero-point) and ergo the number of points used in the estimate is $2^{12} = 4096$. As only the positive frequencies are plotted (symmetry about zero), $\frac{4096}{2} + 1 = 2049$ points are used here. This includes the first frequency of 0 Hz.

The effect of using different NW is shown in **Figure 15**, where the left panel displays the estimates obtained from 7 tapers, while the right panel displays the result from 59 tapers. The number of points is 2049 for both estimates. The figure shows that the resolution is poor and reveals few details in the estimate obtained from 59 tapers. The frequency resolution is good in the estimate obtained from 7 tapers, but the variance is large and causes noise in the spectral estimate. Therefore, it is necessary to vary the number of tapers to ensure important details are resolved.

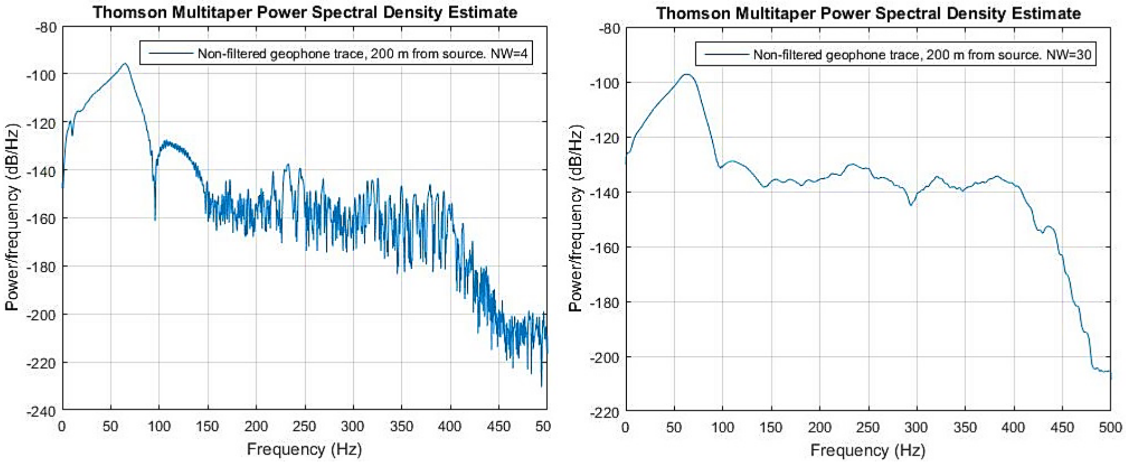

Figure 15 Left panel: multitaper power spectral estimate of a geophone trace at 200 m offset obtained from 7 tapers and 2049 points. Right panel: multitaper estimate of the same trace, but from 59 tapers and 2049 points.

4.3.2 Time-frequency domain: the spectrogram

As the power spectral density estimate gives the average frequency content of the entire time signal, it is useful to visualize the data in the time-frequency domain for the frequency variation in time to be visible. Then it is no longer the time-averaged power spectrum that’s estimated, but rather the power spectral density depending on time (Hanssen, 2003). This is useful for resolving details that may not be visible in the average power spectra. One way of representing a signal in the time-frequency domain is by the spectrogram. This is a measure of the energy spectrum instead of the power spectrum (Hanssen, 2003).

When applying the spectrogram, a data window is chosen to specify the section of the signal where the Fourier transform is estimated. The window is shifted in time and the Fourier transform for the section specified by the shifted window is computed. The type and length of window has to be specified, along with the number of overlapping samples from one window to the next. An illustration of shifted overlapping windows is seen in **Figure 16**.

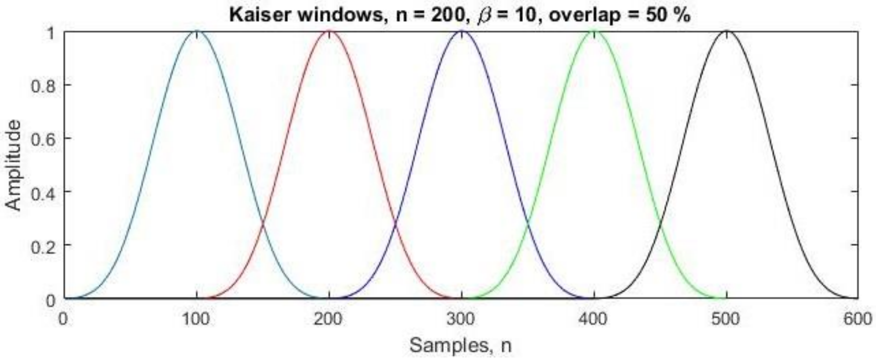

Figure 16 Five overlapping Kaiser windows of length 200. Overlap is 100 samples = 50 %.

For each window, the time and frequency resolutions are the same throughout the entire signal length. One window may therefore be suitable for studying only parts of the frequency spectrum (Hanssen, 2003) and it may be advantageous to vary the parameters of the spectrogram to enhance details in different parts of the spectrum.

The time-frequency plots displayed in the **Results** are obtained using a 200-samples long Kaiser window where the β-parameter (sidelobe attenuation parameter) is varied for the study of different frequencies. The response of a Kaiser window is shown in **Figure 17**. The width of the main lobe and the amount of attenuation of the side lobes change when the window parameters are changed. The number of overlapping samples between each window is specified to 150 and the number of points used for calculating the discrete Fourier transform is 1000. When only short time segments of the data are studied in the time-frequency domain, the length and overlap of each window are adjusted to resolve the frequency components of interest.

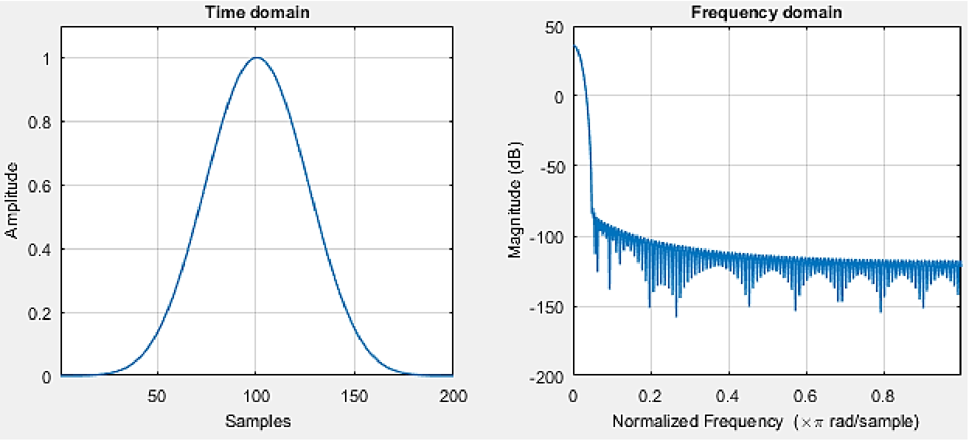

Figure 17 Kaiser window of length 200 and β = 15. A higher β gives a wider main lobe and smaller side lobes.

Spectrograms are estimated for single station signals. The same receivers as those used for the multitaper estimates are picked, as they will be comparable to the power spectra. Spectrograms for both geophones and hydrophones are obtained, and when necessary, only short time intervals of single traces are extracted to view in the time-frequency domain. To help identify the different frequency components of the spectrograms, NMO-velocities provided by the University of Bergen may be applied. A normal moveout (NMO)-velocity is the velocity that corrects the apparent dip or hyperbolic shape of a reflection, and turns it into a horizontal flat one. The offset between source and receivers affects the arrival time at the different receivers, causing the apparent dip of non-dipping interfaces (Milsom & Eriksen, 2011b).

4.4 Filtering of signals

Visualizing single receiver traces makes it possible to identify the flexural wave. At increasing offset, the flexural energy becomes even clearer as it separates further from other waves. Taking, for example, the geophone located 200 m from the source into consideration, the arrival time of the flexural wave is easily identified and its dispersive low-frequent energy is clearly visible. However, on top of this dispersive energy rides another high-frequent wave (as shown in **Figure 35** in the next chapter). By extracting the parts of the signal where this is most prominent, filtering may be performed in order to separate the two frequency components. Performing frequency analysis on the filtered signals may give information about the frequency content of the flexural wave and the higher frequency component riding on top of it. Comparing the frequency and velocity with typical frequency and velocity ranges for different wave modes may indicate what wave the high frequency represents.

Two band-pass filters are designed to cut frequencies above and below 20 Hz to include only the low-frequent component in one signal and only the high-frequent component in the other. Band-pass filters are used rather than low-pass and high-pass filters to clear the very high and low frequencies of the spectra and make the components of interest stand out clearly. The responses of the two filters with cut off frequencies 1 Hz – 20 Hz and 20 Hz – 100 Hz are seen in **Figure 18**. The width of the lobe and the attenuation rate of cut frequencies may be varied by changing the input parameters in the filter design.

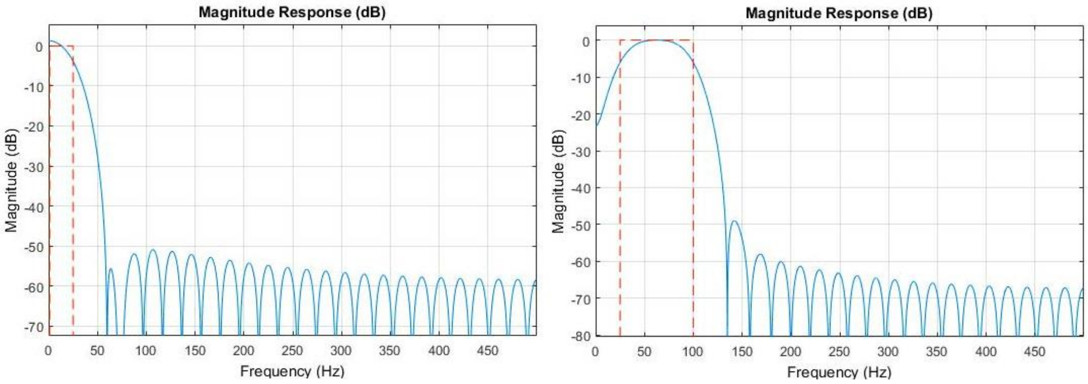

Figure 18 Left panel: band-pass filter response with cut off frequencies 1 Hz and 20 Hz. Right panel: band-pass filter response with cut off frequencies 20 Hz and 100 Hz.

4.5 Ice properties from the dispersion relation in f-k spectra

A method for estimating ice thickness and mechanical rigidity from seismic measurements of ice induced waves was proposed by DiMarco et al. (1993). They found a relationship between flexural rigidity, D, and thickness, h, from the dispersion relation of gravity flexural waves. They estimated cross spectra between two measure points along the ice surface to find the wavenumber, k, as a function of frequency. Our aim is to plot the dispersion relation for the flexural wave observed in the Svea data and use this (instead of the cross spectra) to find corresponding frequencies and wavenumbers to solve for flexural rigidity and/or thickness in the dispersion relation. DiMarco et al. (1993) find the dispersion relation for flexural waves from the equation describing motion in a uniform thin plate floating on a fluid of infinite depth (DiMarco, Dugan & Martin, 1991):

$$D\nabla^4 u(x,y) + \rho_1 h \frac{\partial^2 u(x,y)}{\partial t^2} = P(x,y), \tag{4.1}$$

where ∇^4 is the fourth order spatial derivative and $P(x,y) = p - F(x,t)$ is the difference between the pressure at the ice surface and the surface load (DiMarco et al., 1991). The flexural rigidity is $D = \frac{Eh^3}{12(1-\nu^2)}$, where ν is Poisson's ratio and E is Young's modulus. The gravitation acceleration is g, ρ_1 is ice density and the vertical deflection is $u(x,y)$. The dispersion relation is derived from the wave equation by assuming $u(x,t) = e^{i(kx-\omega t)}$.

By assuming that the water flow below the ice is irrotational with small velocity, and that energy is conserved, Bernoulli's equation gives the pressure at the surface as (DiMarco et al., 1991; Hosking & Sneyd, 1986)

$$p = \rho \frac{d\phi}{dt}\bigg|_{z=0} - \rho g u(x,y), \tag{4.2}$$

with the velocity potential $\phi(x,y,z,t)$ and sea water density ρ. The $\rho g u$-term is the pressure exerted by the water. Assuming continuity in the water,

$$\frac{\partial^2\phi}{\partial x^2} + \frac{\partial^2\phi}{\partial y^2} + \frac{\partial^2\phi}{\partial z^2} = \nabla^2\phi + \frac{\partial^2\phi}{\partial z^2} = 0, \tag{4.3}$$

Eq. (4.2) has to satisfy the boundary conditions at the ice surface (z = 0) and at the water bottom (z = H) (DiMarco et al., 1991)

$$\left.\frac{\partial \phi}{\partial z}\right|_{z=u} = \frac{\partial u}{\partial t}, \tag{4.4}$$

$$\left.\frac{\partial \phi}{\partial z}\right|_{z=H} = 0. \tag{4.5}$$

The potential ϕ is found from Eq. (4.4) by taking the Fourier transform of Eq. (4.3) - Eq. (4.5) and using the expression obtained from the transformed Eq. (4.3) in the transformed Eq. (4.4). Substituting the terms into Eq. (4.2) gives pressure as (DiMarco et al., 1991)

$$p = \frac{\rho\omega^2\hat{u}}{k} - pg\hat{u}, \tag{4.6}$$

where $\hat{u}$ is the transformed deflection. *k* is wavenumber and *ω* is angular frequency. Eq. (4.6) may now be substituted into Eq. (4.1) to obtain the expression of the equation of motion including p.

Differentiating the assumed plane wave $u(x,t) = e^{i(kx-\omega t)}$ twice with respect to *t* and four times with respect to *x*, and substituting the terms into Eq. (4.1) gives the dispersion relation as (DiMarco et al., 1993)

$$Dk^4 - \rho_1 h\omega^2 + \rho g - \frac{\rho\omega^2}{k} = 0. \tag{4.7}$$

Solving Eq. (4.7) for frequency gives *f* as a function of *k*:

$$\frac{\omega}{2\pi} = f = \frac{1}{2\pi}\sqrt{\frac{\rho g k + Dk^5}{\rho + \rho_1 h k}}. \tag{4.8}$$

In Eq. (4.7) and (4.8), the ice thickness *h* is included, and thus the allowed f-k pairs are valid for one specific thickness. Then, theoretical frequency may be plotted as a function of *k* by simply choosing a value of *h*. Eq. (4.7) may be solved to find the thickness as well as the frequency. This gives a third order polynomial where *h* is depending on all the above variables. A simplified expression becomes the cubic function

$$h^3 + \alpha h - \beta = 0, \tag{4.9}$$

where $\alpha = \frac{-12(1-\nu^2)\rho_1\omega^2}{Ek^4}$ and $\beta = \frac{12\rho(1-\nu^2)(\omega^2-gk)}{Ek^5}$.

The graph of the cubic function is shown in **Figure 19**, where its interception with the x-axis corresponds to the thickness. The interception and the curvature of the graph change as wavenumber and frequency vary. The figure shows an example of how the thickness changes with *k* when frequency is left unchanged at 10 Hz.

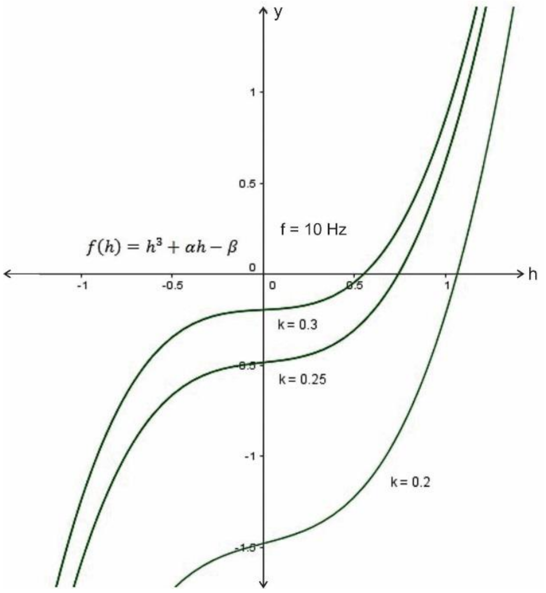

Figure 19 The cubic function giving *h* depending on *α* and *β* as defined above. The three graphs show how *h* vary with *k* when *f* is constant.

Further, a 2D Fourier transformation is applied to all the geophone traces to plot the dispersion relation of the data in an f-k spectrum. During a two-dimensional Fourier transform, the spatial dimension is transformed to wavenumber and the temporal dimension is transformed to frequency. The spectrum obtained gives the wavenumber as a function of frequency, which may be used to solve for h in Eq. (4.9). To optimize the f-k spectrum, windows are applied in both dimensions. Kaiser, Hamming and Hann windows of lengths 4001 and 120 are applied in the temporal and spatial dimensions, respectively. Different windows give different resolutions when applied, and the spectra of satisfying quality are studied in detail. For the Kaiser windows, $\beta = 5$ is chosen.

The f-k pairs may be used to solve Eq. (4.9) numerically as well as graphically. For the cubic equation, the solution can be written in terms of a hyperbolic cosine function as (Holmes, 2002)

$$h_0 = -2\frac{|\beta|}{\beta}\sqrt{-\frac{\alpha}{3}}\cosh\left(\frac{1}{3}\cosh^{-1}\left(-\frac{3|\beta|}{2\alpha}\sqrt{-\frac{3}{\alpha}}\right)\right), \tag{4.10}$$

which holds for $4\alpha^3 + 27\beta^2 > 0$ and $\alpha > 0$.

As D is dependent on h^3, a relationship between the two variables may be found. DiMarco et al. (1993) found this relationship as $D = 0.20h^3$ by the use of cross spectra. The use of f-k spectra may give slightly different results. A relationship between rigidity and thickness makes it possible to estimate the rigidity directly from the thickness, i.e. without estimating Young's modulus (DiMarco et al., 1993). Such a possibility may be useful for large scale examinations of sea ice.

5 Results

Analyzing and plotting data to obtain the following results are performed using MATLAB (version R2015b) scripts for geophysical plots and functions from the additional seismic program package for MATLAB, SeisLab (version 3.02). As the dephasing process leaves out large parts of the frequency content and no combination of geophones and hydrophones are intended, it is skipped in most analyses. Signals from test 3 are chosen as these data consists of corresponding geophone and hydrophone traces. Data collected from shot point A are chosen for analyses due to the smaller offsets giving shallower and stronger reflections compared to the other shot points.

The following chapter presents the results from the different exploring analyses described previously. Plots of most of the following figures contain data within the first 4 seconds of the recording time, as all energy of interest falls within this interval. In some cases, the full recorded 8 seconds are studied in order to verify or invalidate indications in the first 4 seconds.

5.1 Autocorrelation functions

As the autocorrelation function, R_{GG}, is symmetric about zero for real valued data, only the values along the positive time lag axis will be plotted. The correlation coefficients along the y-axis are normalized.

Following are figures (**Figure 20 - Figure 22**) showing the autocorrelation functions of geophone traces at increasing offset. It can be seen that the frequency seems to decrease (the wavelength lengthens) as the distance from the source increases, indicating that the dispersive component of the signal is the strongest one. After 400 m of propagation, the autocorrelation function shows traces of secondary higher frequency oscillations as **Figure 22** displays. The secondary oscillation is probably due to attenuated flexural waves in combination with other wave modes becoming more prominent at this stage.

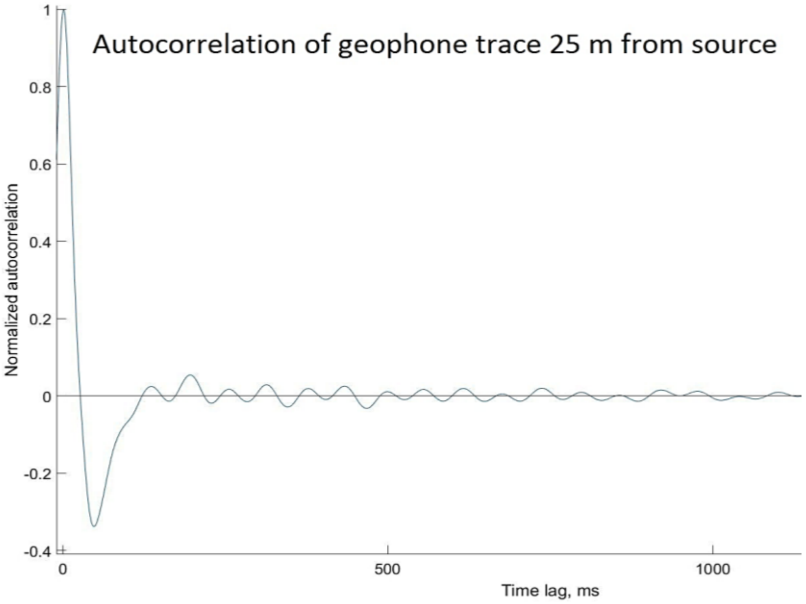

Figure 20 Autocorrelation function of the first geophone, 25 m from the source. Correlation coefficients are normalized.

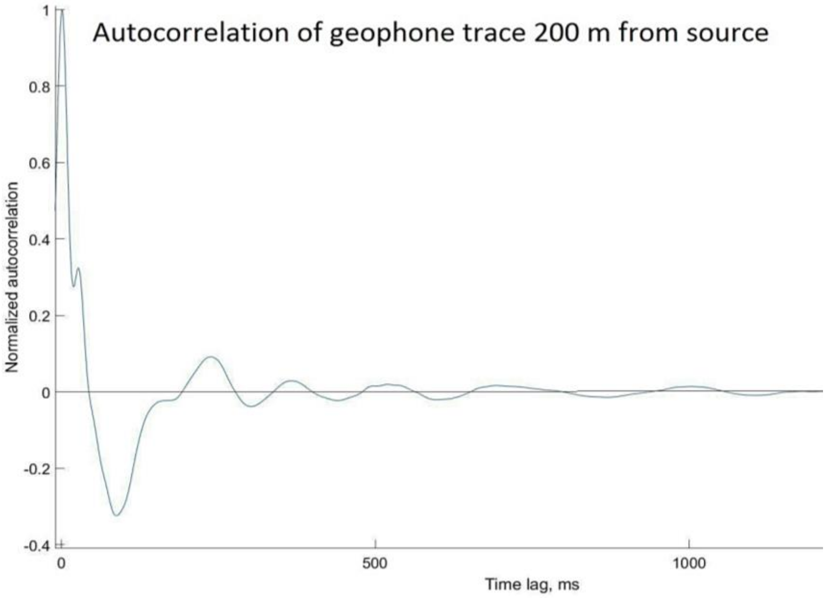

Figure 21 Autocorrelation function of the geophone trace 200 m from source. Normalized correlation coefficients.

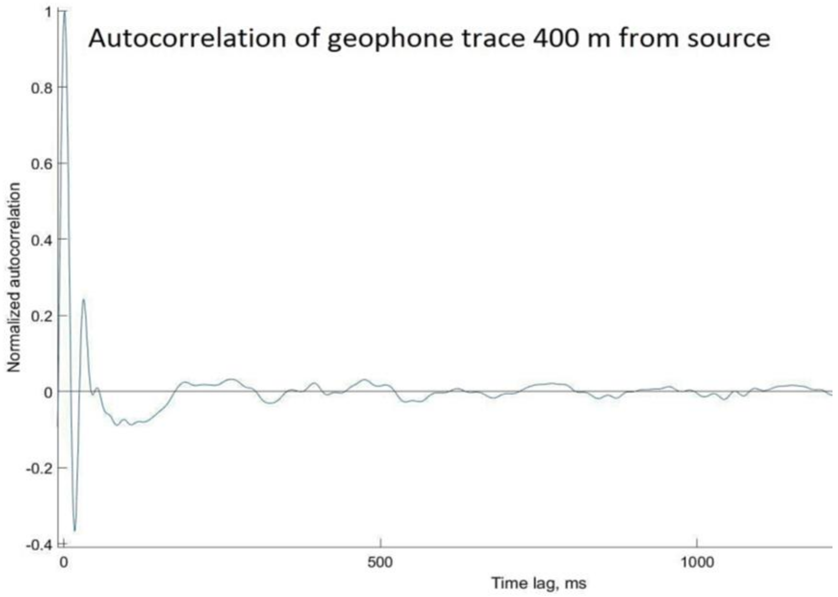

Figure 22 Auto correlated geophone 400 m from source. Normalized correlation coefficients. Traces of secondary oscillations are visible.

Estimating the frequency content of the autocorrelation functions gives the same spectra obtained from time-frequency analysis of single traces, as will be shown in the next sections. Spectra from the auto-correlated geophone traces and single geophone traces clearly show the flexural wave and its corresponding frequencies. These spectra are displayed later.

5.2 Cross-correlation functions

The cross-correlation function, R_{GH}, is not symmetric about zero and thus both positive and negative time lags are plotted. Normalized (dimensionless) cross-correlation functions are used for the following plots.

Cross-correlation functions were estimated between every second geophone to find the velocity of the ice wave propagation. The velocity found is an average across a 12.5 m interval between the two receivers. The plot in **Figure 23** shows the velocity estimated from these correlations. At 25 m distance from the source, the velocity is 195 m/s. The velocity has increased to 379 m/s after 750 m, thus indicating that the estimated velocity likely represents the flexural wave.

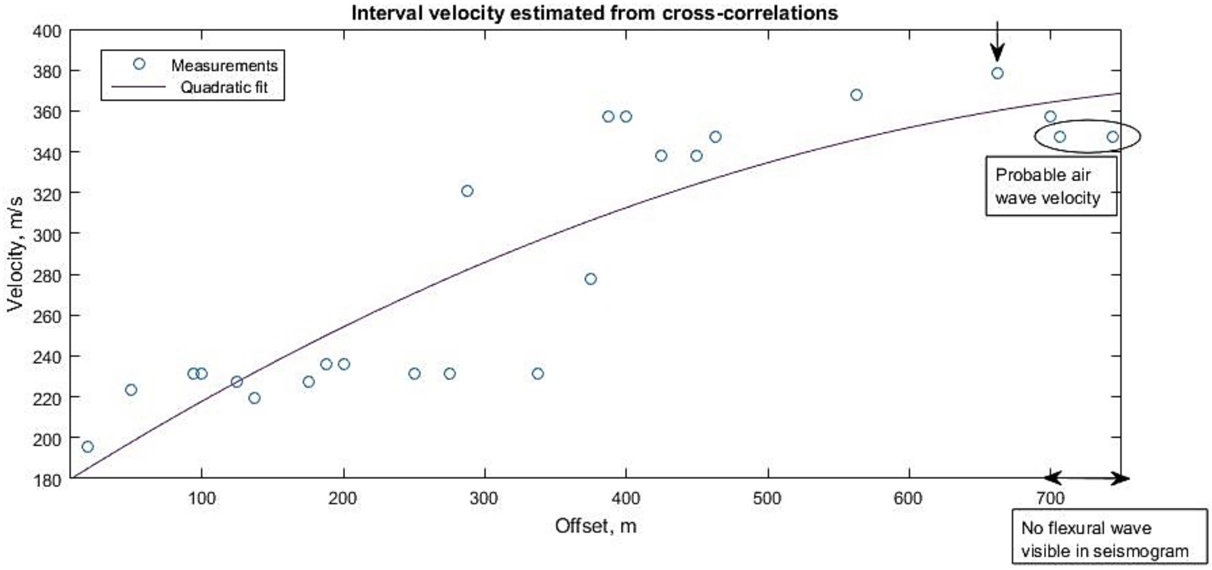

Figure 23 Propagation velocity estimated from cross correlating every second geophone (12.5 m spacing) in test 3. Offset along the x-axis is calculated from the first receiver in the array. The purple line is the quadratic fit to the measurements. The arrow points to the highest estimated velocity at 379 m/s. Indicated by the ellipse are points at 347 m/s, probably representing the air wave.

The velocity profile in the plot resembles the shape of theoretical velocity profiles for anti-symmetric flexural waves found in literature as estimated by several authors (Gomez et al., 2011; Jensen, 2016) (see **Figure 24**). Comparisons of shapes and slopes of theoretical curves to the one estimated in the data indicate that **Figure 23** shows the phase velocity.

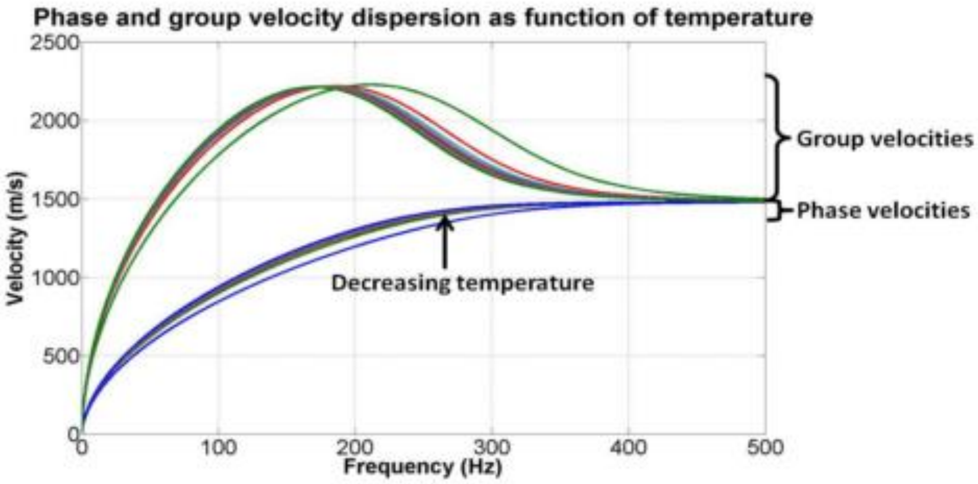

Figure 24 Theoretical phase and group velocities of flexural waves in ice with varying temperature, produced by Jensen (2016). (Figure from Jensen (2016)).

The velocity profile of **Figure 23** shows an area of highly variable velocities between 200 m and 400 m offset. This may be an effect of the way calculations are performed. After about 400 m distance, the increase rate declines. This is about halfway through the array of receivers, and wiggle plots show that flexural waves are attenuated after this distance. The velocity towards the end of the array is slightly lower than what's found only a few meters earlier. At the very last receivers, barely any flexural energy is present and the air wave is the only component seen clearly. Therefore, the velocity found from cross-correlations at the rear end of the receiver array may correspond to the air wave rather than the flexural wave. The velocity at the points indicated by the ellipse is 347 m/s.

In the geophone seismograms, for example the one in **Figure 13,** the flexural wave arrives around the same time and after the air wave. This means that its group velocity must be close to or lower than the velocity of the air wave. As some of the velocities calculated from cross-correlations exceeds the air wave velocity, it means that the velocity found here probably is the phase velocity of the flexural wave.

A plot of the average velocity estimated relative to the first receiver in the array is shown in **Figure 25**. This is estimated by cross-correlating the first geophone trace with several other traces at varying distances. The best-fitted curve of average velocity is similar to the interval velocity curve. The maximum average velocity found at the end of the array here is 361.70 m/s, which is naturally lower than the maximum interval velocity. At the beginning of the array, the average velocity is closer to the interval velocity than at the end of the array, as the distance between the correlated receivers are shorter here. At 25 m from the source, the average velocity is 192 m/s.

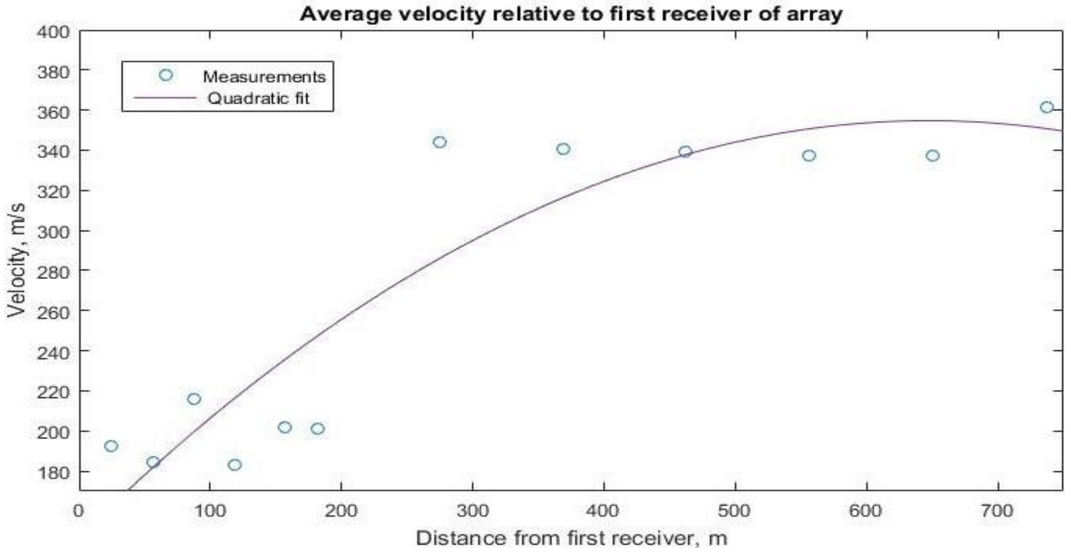

Figure 25 Average propagation velocity estimated from cross-correlating different geophones with the first one. Distance along the x-axis is relative to the first receiver.

As seen in **Figure 26**, the cross-correlation functions between two geophones in the first half of the array gave negative correlation coefficients at max correlation. A negative correlation means that the two signals are out of phase. Two positively correlated signals are in phase, as in the second half of the array. At the geophones in the middle of the array, both large negative and positive correlation values are observed at close time lags. Thus, at offsets smaller than about 350 m the two correlated geophone signals are out of phase, and geophones at larger offsets are in phase. The transition from out of phase to in phase is indicated by the cross-correlations functions at about 300-375 m. It may therefore be concluded that the flexural wavelength must be smaller than the receiver spacing (12.5 m) between 0-325 m travel distance (including the distance to the source), and larger than 12.5 m after about 400 m of propagation.

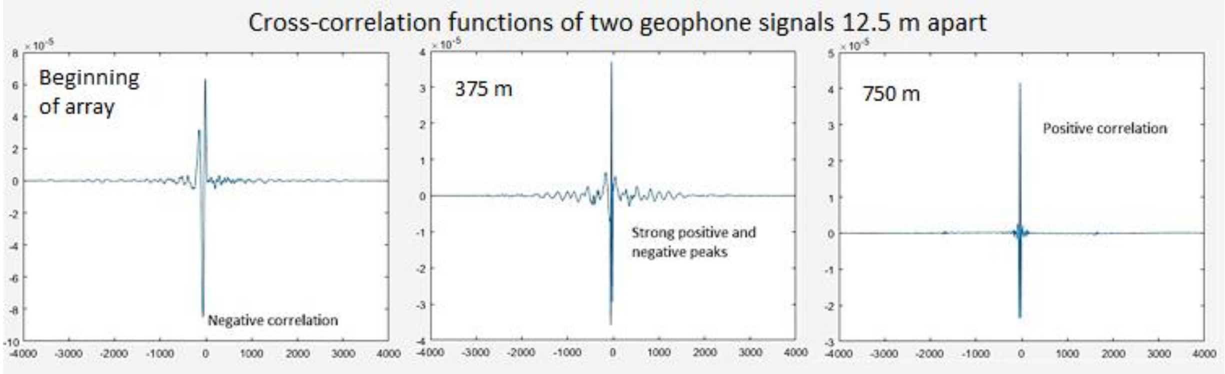

Figure 26 Cross-correlation functions of two geophones 12.5 m apart at different offsets. The transition from waves out of phase to in phase is around 300-350 m.

Both **Figure 23** and **Figure 25** show great variations from one measure point to the next between 200 m and 400 m. As cross-correlations within this interval show very small differences between positive and negative correlation peaks, it may indicate that the wavelength is close to the receiver spacing of 12.5 m here. Therefore, aliasing may be present in this part of the array and the estimated velocities here may be inaccurate.

The larger the offset between the receivers, the more the dispersive envelope is separated from other wave modes in the cross-correlation function. This is due to the low velocity of dispersive waves relative to the reflections. This is seen in **Figure 27** where an envelope of dispersive waves has developed and separated from the peaks as the wave has propagated.

Low frequency flexural waves travel further than high frequency direct waves and reflections due to attenuation (Ziola & Gorman, 1991) and thus they are naturally seen at large correlation time lags. Some “noisy” wiggles are seen at the large negative time lags following the dispersive envelope. Analysis based on cross-correlated signals with dispersive content performed by Ziola and Gorman (1991) show similar results. Further investigations of their signals indicate that these “noisy” parts correspond to very low frequent reflections. As for the 2013 data from Svalbard, the parts of the cross-correlation function highlighted by the ellipse in **Figure 27** may be a result of reflections from the fjord margins.

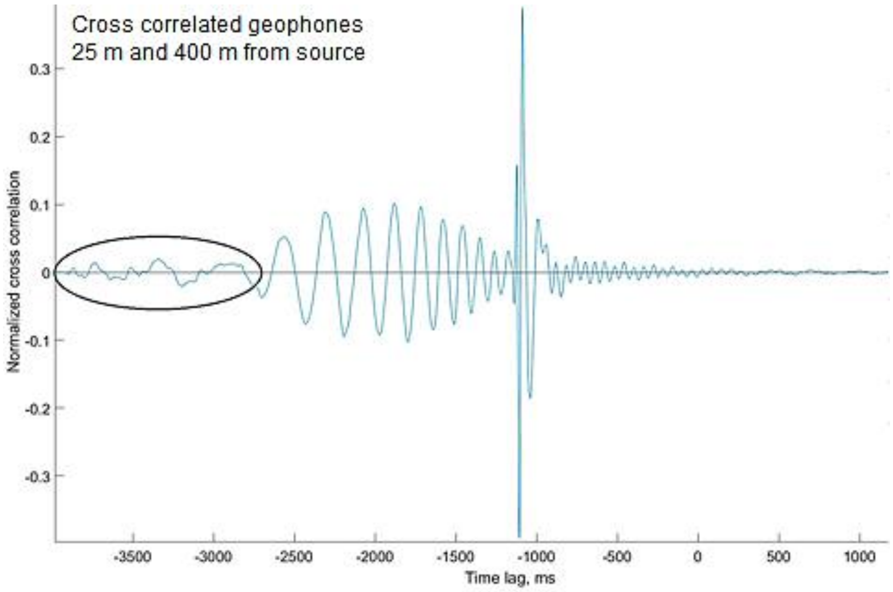

Figure 27 Cross-correlation estimated between the geophones at 25 m and 400 m distance from the source. Indicated are the “noisy” wiggles probably caused by low frequent reflections of fjord margins.

5.3 Multitaper power spectral density estimates

The power spectral density is estimated using the multitaper method as this gives more satisfying and accurate results than other standard methods (Hanssen, 2003). As it is interesting to identify other waves in addition to the flexural wave, the estimates are performed on raw data rather than dephased data where no energy is present above 50 Hz.

The number of tapers to be used in the estimate is 2NW – 1 (The MathWorks Inc, 2015), where the quantity of NW is varied according to what details one wants to study in the following figures.

Figure 28 shows the spectral estimate of geophone traces 25 m, 200 m and 400 m from the source. The lower frequencies are the most prominent ones in all of the traces. Frequencies above approximately 100 Hz are gradually decreasing in power. As the distance from the source increases, higher frequencies gradually decrease in power towards the Nyquist frequency at 500 Hz. Frequencies below 100 Hz are different from the near offset receiver to the far offset ones, probably due to the effect of the source detonation. However, all three receivers have a peak at 65 Hz, which is more pronounced as offset increases.

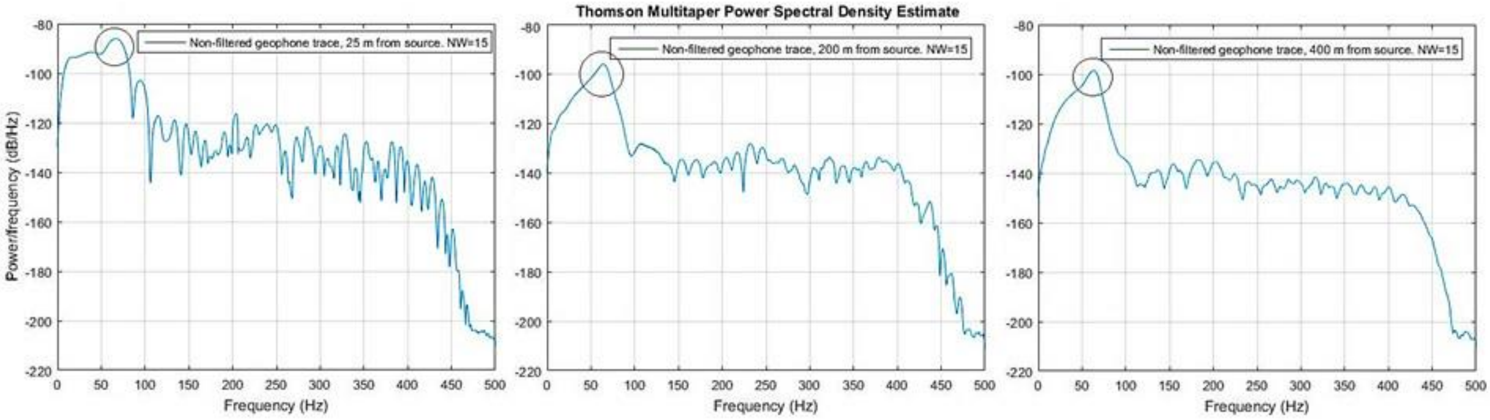

Figure 28 Power spectral density estimate of geophone traces. Number of tapers is 29, number of points is 2049. 65 Hz peak is indicated.

Hydrophone (1 m depth) spectra obtained from the same estimate show the same frequency peak at about 65 Hz as in the geophones. As it is present in both receiver types throughout the entire array, it is likely representing some important component of the signal and might be related to the ice and its properties.

Muting the air wave before estimating the power spectrum helps identify the component corresponding to the 65 Hz peak, where it rules out the possibility of it representing the air wave. After muting, the power spectrum still has the peak at about 65 Hz. Muting affects the entire spectrum, but the difference is largest around 30 Hz as can be seen in **Figure 29**, indicating that the air wave is broad-banded but strongest around 30 Hz.

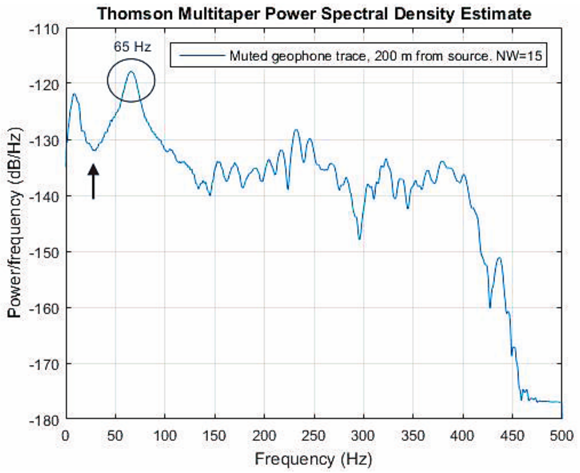

Figure 29 Estimated power spectral density of a muted geophone trace 200 m from the source. The arrow indicates the likely air wave frequency and the circle indicates the same peak seen in the unmuted power spectra.

5.4 Spectrograms

The following section presents the results obtained from viewing data in the time-frequency domain. Such an approach resolves details that may not be visible in the power spectrum as it includes the variation in time for different frequencies.

The spectrograms reveal several frequency components of high energy. Initially, the spectrum has broad-banded energy covering almost the entire frequency range as indicated in **Figure 30**. As offset increases, the arrival time of this broad-banded wave increases as well, and thus it is likely the direct waves from the detonation arriving at the different receivers. In addition, a very powerful peak at 65 Hz corresponds to the peak already seen in the power spectra from the multitaper estimates. This is indicated in **Figure 30** as well. From the known distance between source and receiver and the approximate air wave velocity, the arrival time of the air wave is easily found and the air wave is identified as the broad-banded energy arriving just after the 65 Hz.

As in the multitaper estimates, the 65 Hz peak is visible in the 1-m deep hydrophone spectrograms (right panel of **Figure 30**), but not at greater depths. This indicates that the 65 Hz might be an ice related wave rather than reflections from depth. In the geophones and hydrophones located closest to the source, the broad-banded detonation energy and the air wave arrive at the same time as the 65 Hz, as they have not yet had the time to separate due to the short distance of propagation.

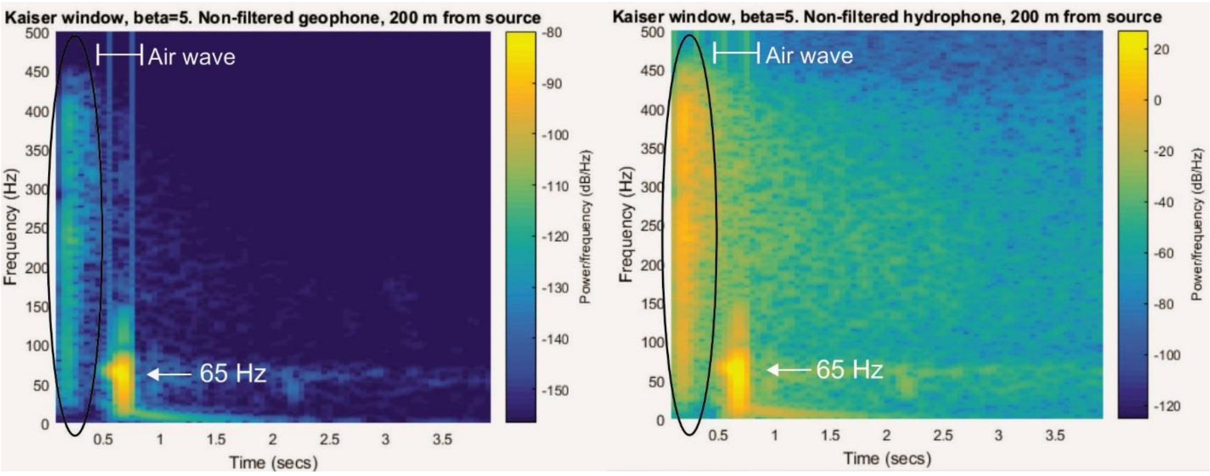

Figure 30 Left panel: spectrogram from the geophone at 200 m offset. Right panel: hydrophone (1 m depth) at 200 m offset. Frequency peak at 65 Hz is indicated by the white arrow. Broad-banded burst is indicated by the ellipse.

Following the 65 Hz peak is relatively broad-banded energy lasting several seconds. This is indicated in the left panel of **Figure 31**. The long-lasting energy is a possible indication of a resonance frequency at which oscillations in the ice occur. From studying several spectrograms, it is clear that the energy at 65 Hz is present throughout the entire section of 4 seconds. The central frequency might seem to decrease somewhat throughout propagation, but as it is broad-banded this is rather uncertain.

Following the air wave is another very prominent and low frequent chirp gradually decreasing from 12 Hz to 3 Hz. This chirp is very clear in most of the receivers, but it is barely visible in the geophone at 775 m offset (right panel of **Figure 31**). This far offset receiver spectrogram shows that the high energy around 2.3 seconds seem to be two separate peaks: 30 Hz and 70 Hz. The 30 Hz is the peak of the broad-banded air wave as was seen in the power spectrum when the air wave was muted. Judging from their arrival times in all of the spectrograms, the air wave and the 65-70 Hz energy travel along side of each other, probably one of them being pushed by the other one. The reason for a peak at 70 Hz instead of 65 Hz at 775 m offset is probably an effect of the plot.

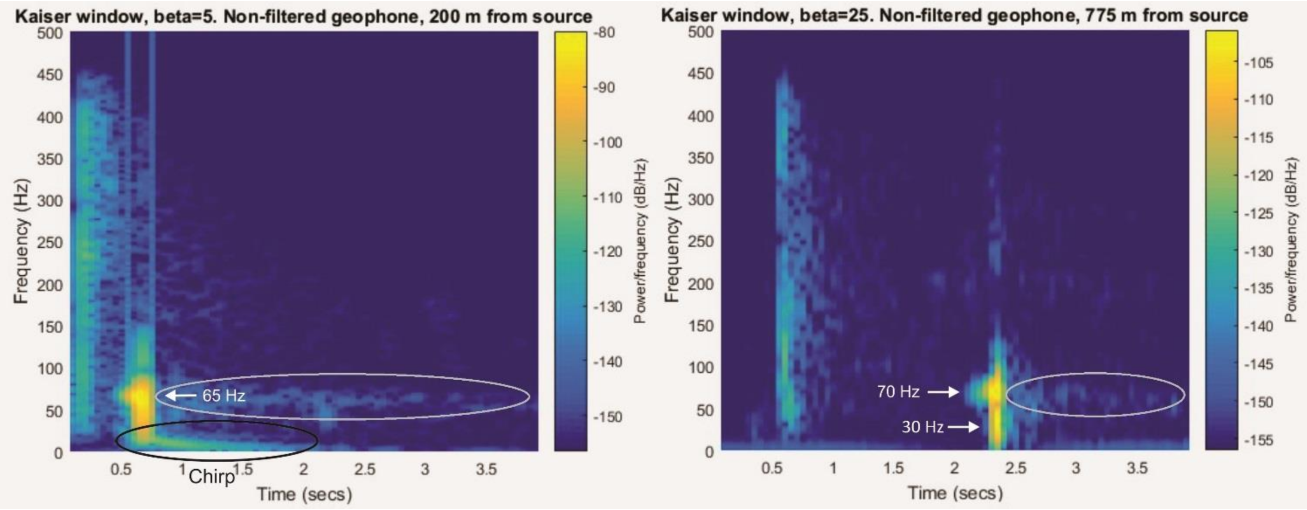

Kaiser window, beta=5. Non-filtered geophone, 200 m from source

Kaiser window, beta=25. Non-filtered geophone, 775 m from source

Figure 31 Left panel: spectrogram for the geophone at 200 m offset. The peak at 65 Hz and the following long-lasting energy is indicated. A chirp between 600 ms and 2000 ms is indicated by the black ellipse. Right panel: spectrogram of the last geophone in the array, 775 m offset.

Both the energy propagating from 12 Hz and 65 Hz are long lasting, but the higher frequency component lasts extremely long compared to the other observed wave modes. A common phenomenon in oscillating system is that different component are harmonics of each other such that $f_n = (n+1)f_0$ (Gunther, 2012). If both the 12 Hz chirp and the 65 Hz energy are caused by the ice itself, a possibility is that there exists such a relationship between them. Initially, they start off at 12 and 65 Hz, making $f_0 = 12$ Hz and $f_4 = 5 * 12 = 60$ Hz. However, if they were to be harmonically related, the same relationship should exist throughout the entire signal. After a few seconds, the 12 Hz has decreased to 3 Hz, while the 65 Hz might have decreased – but not as much as the other component. Then, $f_0 = 3$ Hz and $f_4 = 5 * 3 \neq 60$ Hz, and these components are not harmonically related.

As only half the recording time has been plotted in all the previous plots, it is interesting to create spectrograms containing the full recorded 8 seconds to investigate whether any of the frequency components actually are visible after 4 seconds. **Figure 32** shows the spectrogram between 0 and 8 seconds for the geophone signal recorded at 200 m offset, where the energy following the 65 Hz energy peak is still visible after 8 seconds.

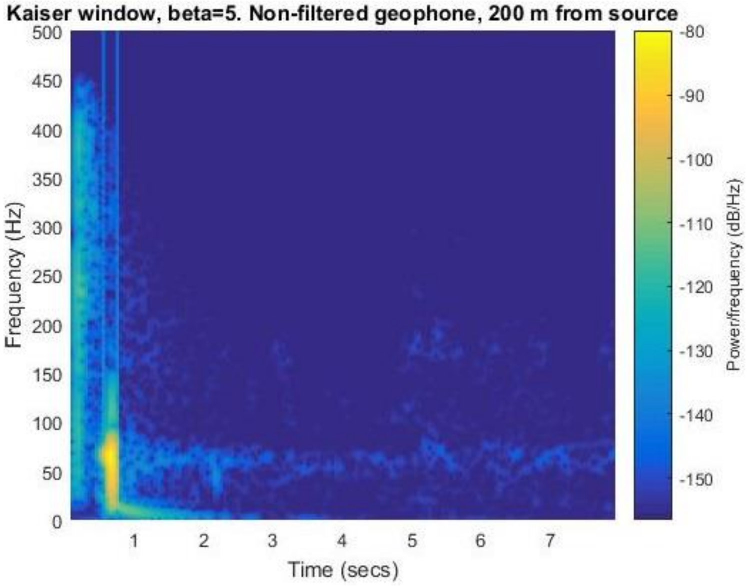

Figure 32 Spectrogram for the full recorded 8 seconds of a geophone.

A way of confirming that the frequency components observed in the spectrograms and multitaper estimates are real, is to perform the same analyses on data collected during test 1. Test 1 was collected two days earlier than test 3 and therefore comparisons of their estimated time-frequency spectra indicate which components are robust. From estimating the power spectral density and creating spectrograms for several geophones and hydrophones from test 1, using the same input parameters as for the plots obtained from test 3, several of the components described already are recognized. To rule out the possibility of any of the features being effects of acquisition geometry, data obtained using line sources are investigated in the same way. It may be concluded that all features identified in test 3 data are robust features originating either from the ice itself or the geology.

To help identify what waves are represented by the observed frequencies, velocities of the different arrivals, provided by the University of Bergen, is applied in addition to comparison of single traces and spectrograms. The velocities and events given in the seismogram of **Figure 33** correspond to the events identified in **Figure 14**. The direct wave has a velocity of 2446.8 m/s, while the seafloor reflection has a velocity of 1404.6 m/s. The refracted wave has velocity 4625 m/s, which is much higher than those of the direct and the reflected wave. Thus, it will outrun them after a certain distance and be the first to arrive at the receiver, as for example at 775 m offset (indicated in **Figure 38**).

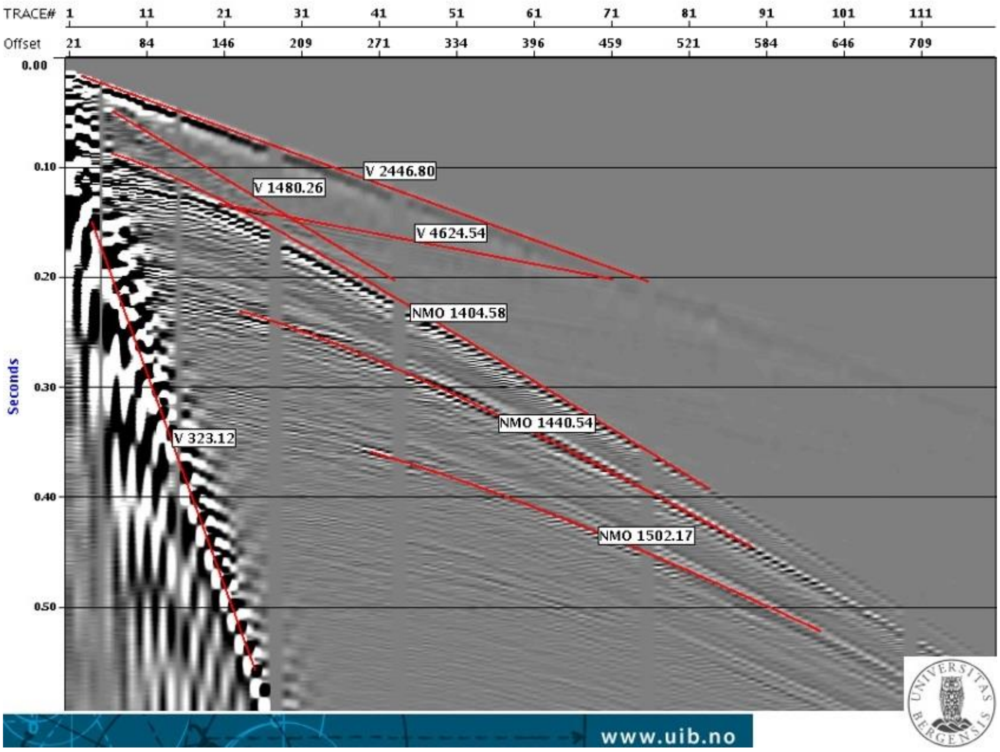

Figure 33 NMO-velocities from analysis performed by the University of Bergen.

Using the velocities of the different events (direct wave, seafloor reflection and refracted wave) to calculate the arrival time at the receiver 200 m from the source makes it easy to identify what frequency component they correspond to in the spectrogram. The events are identified in the single receiver traces based on the same calculations of arrival times. **Figure 34** shows the trace at 200 m and its spectrogram with the different events identified. At this distance, the refracted wave has not yet outrun the direct wave and they are arriving very close to each other.

In **Figure 34**, a higher frequency is seen to ride along with the flexural wave. As this must have the same arrival time as the flexural wave in the spectrogram, it is likely the long-lasting 65 Hz seen in previous figures. The next section presents the filtering performed to confirm or invalidate this hypothesis.

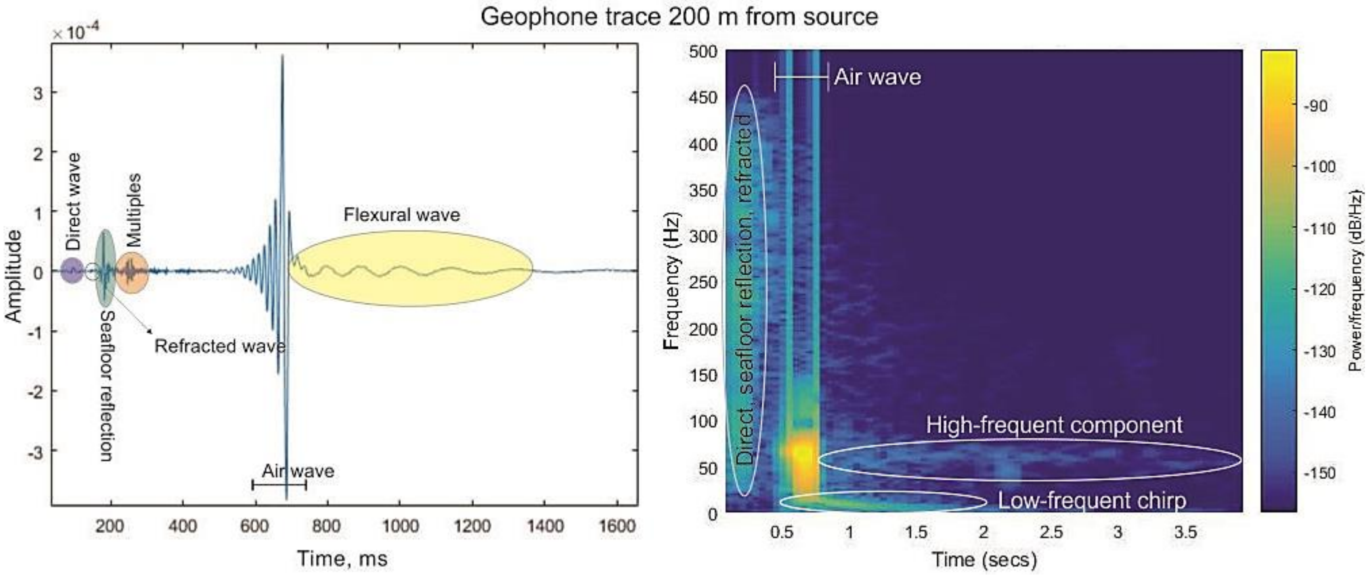

Figure 34 Left panel: trace at 200 m offset. Right panel: spectrogram of the trace. Different events are identified based on NMO-velocities and calculated arrival times.

5.5 Filtering of signals

Considering the geophone signal registered 200 m from the source, we extract the section between 725 ms and 4000 ms, as seen in **Figure 35**, in order to separate the higher and lower frequencies of the signal by filtering.

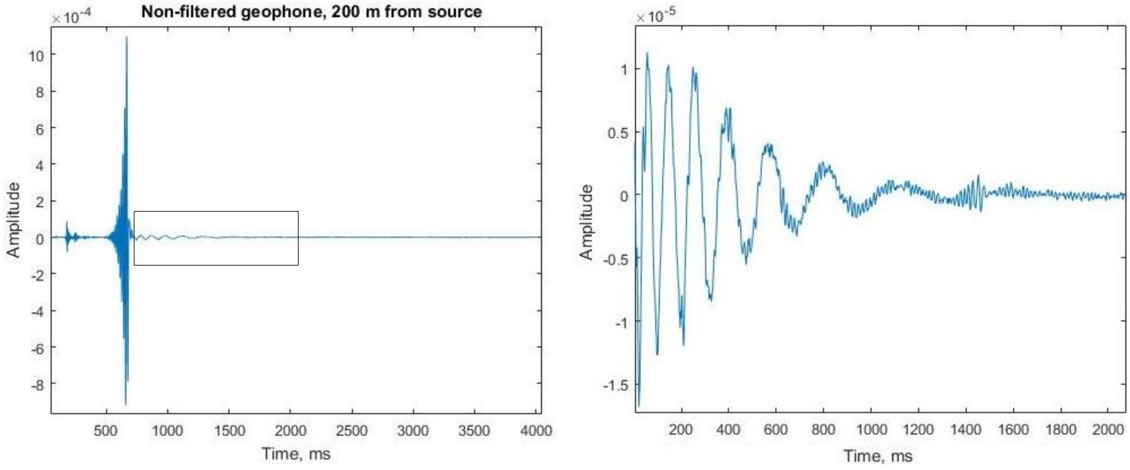

Figure 35 Left panel: geophone signal registered 200 m from the source. Right panel: extracted part of the signal, between 725 and 4000 ms, only including the flexural wave where lower and higher frequencies are overriding each other.

The frequency content of the extracted part of the trace does not include the air wave and the high-energy peak at 65 Hz, as only the energy arriving after the air wave is extracted. From the single trace is it clear that this section includes mostly just the flexural wave and the high-frequent component riding along it. The frequency content of this section is estimated both by the multitaper method and the spectrogram, and the results are shown in **Figure 36**. Comparisons of these spectra identifies the flexural wave as the low frequent chirp already found in previous spectrograms. As other broad-banded and high energy waves are left out, the flexural wave is now prominent in the power spectrum. In the previous power spectra, it has not been possible to identify alone due to interference with other waves within the same frequency range.

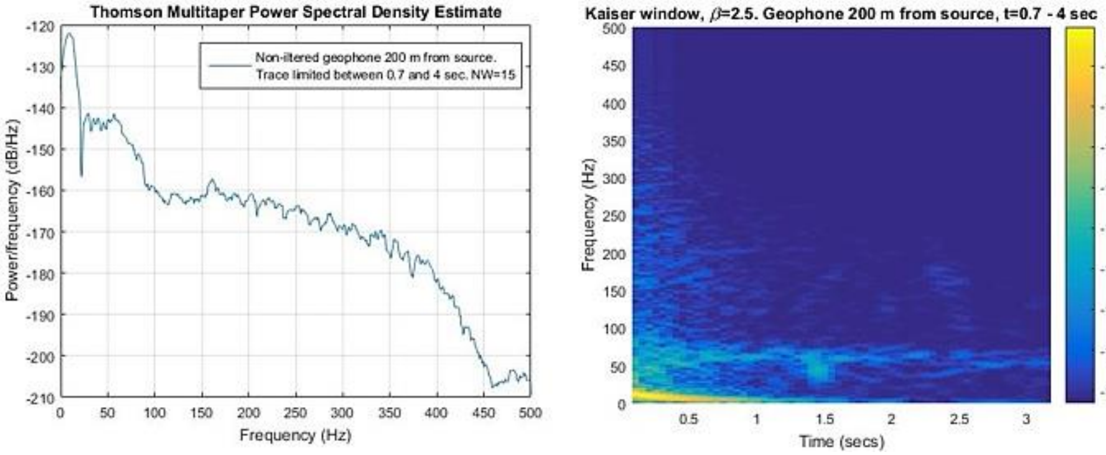

Figure 36 Left panel: multitaper estimate of geophone energy between 0.7 and 4.0 seconds. Right panel: spectrogram of the same section. The distance from the source is 200 m.

Spectral estimates and spectrograms may be computed to study the frequency content of the two filtered signals. As we have limited the trace to only include the flexural waves this confirms that the flexural waves generated in first-year Arctic fjord ice at Van Mijenfjorden have low frequencies starting off at 12 Hz and tapering off to 3 Hz as seen in the estimated spectrogram in **Figure 37** (left panel). From the performed filtering, one may also observe that the energy surrounding 65 Hz becomes narrower and ends up with a slightly lower central frequency compared to the initial one. The bandwidth is 70 Hz at the beginning of the extracted time interval, whereas it has narrowed to a bandwidth of 25 Hz at the end of the trace.

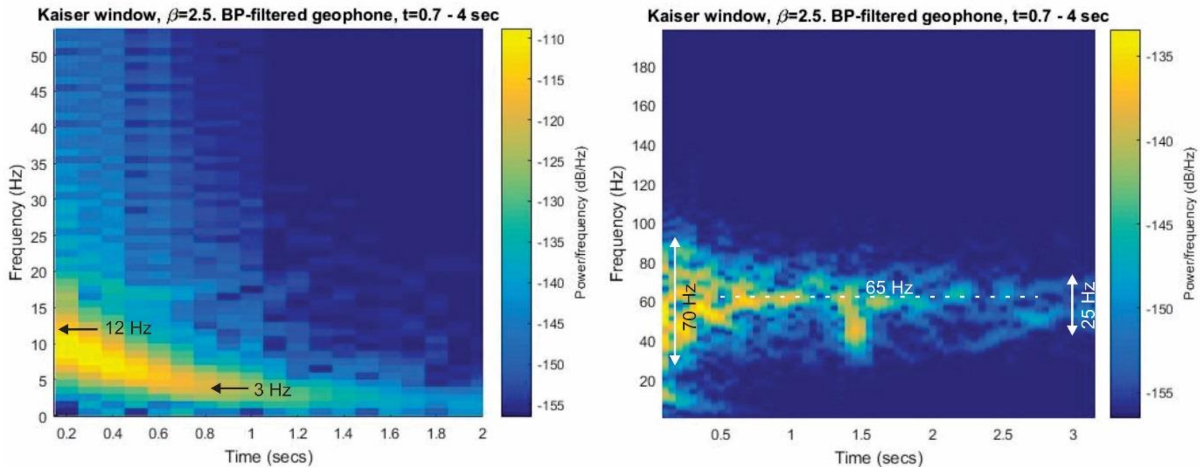

Figure 37 Left panel: spectrogram of low-frequency band-pass filtered geophone signal between 0.7 and 4.0 seconds. Right panel: spectrogram of the same section, but high-frequency band-pass filtered.

From the single trace, it seems like the 65 Hz energy is travelling as a secondary oscillation on top of the dispersive low-frequent wave. According to its spectrogram of **Figure 37** (right panel), the 65 Hz seems to be a non-dispersive wave decreasing its bandwidth as it propagates.

Now that there is no doubt on what frequencies correspond to the flexural wave, it may be identified in the spectrogram along with the other wave modes as in **Figure 34**. **Figure 38** shows both the flexural wave and the high-frequent component riding along it in the spectrogram. At 775 m distance from the source, only the high-frequent component remains as the flexural wave is attenuated. As the 65 Hz component is long-lasting and prominent throughout the entire length of the array, it is attenuated slowly and probably propagating quickly. Because the refracted wave has outrun the other waves, it arrives first at the receiver 775 m from the source. It is indicated in the right panel of **Figure 38**.

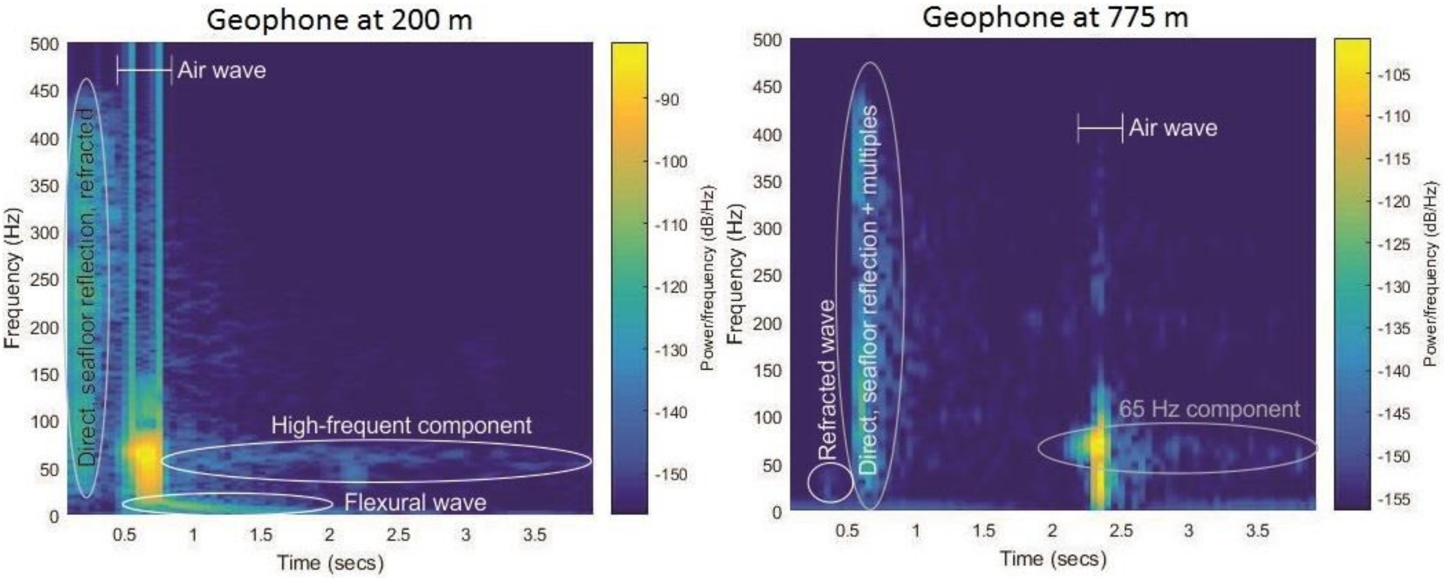

Figure 38 Left panel: Wave modes in the 200-m geophone. Right panel: the same wave modes at 775 m.

5.6 Dispersion relation in the f-k spectrum

Performing a 2D FFT gives a spectrum where frequency is a function of wavenumber. Thus, the dispersion relation may be found from identifying the flexural wave in this spectrum. Three different windows are applied to ensure satisfying resolution to study the details of interest. The Hann, Hamming and Kaiser window are suitable for different purposes as they enhance different details. The effect of windows in either the temporal or the spatial dimension, or in both dimensions is seen in **Figure 39**, where frequencies up to 100 Hz are displayed as the dispersive energy lies within this range. When applied only in space (middle panel of figure), other wave modes at higher frequencies are resolved in the spectrum. When windows are applied in both dimensions at the same time, the resolution at low frequencies generally seems better and two windows are chosen for the study of flexural waves.

Energy is highest within the first 100 Hz of the f-k spectrum and therefore waves at these frequencies are probably related to the ice itself. Several linear and parallel events with the exact same spacing between them are observed here. Linear features must be non-dispersive as their linearity means that $f \sim k$. At the very lowest frequencies of the f-k spectrum, a non-linear event is observed. This must be the flexural wave, as dispersive components are non-linear features in an f-k spectrum. Both the dispersive and the non-dispersive events are indicated in **Figure 39** by the white dotted and the black dashed line, respectively.

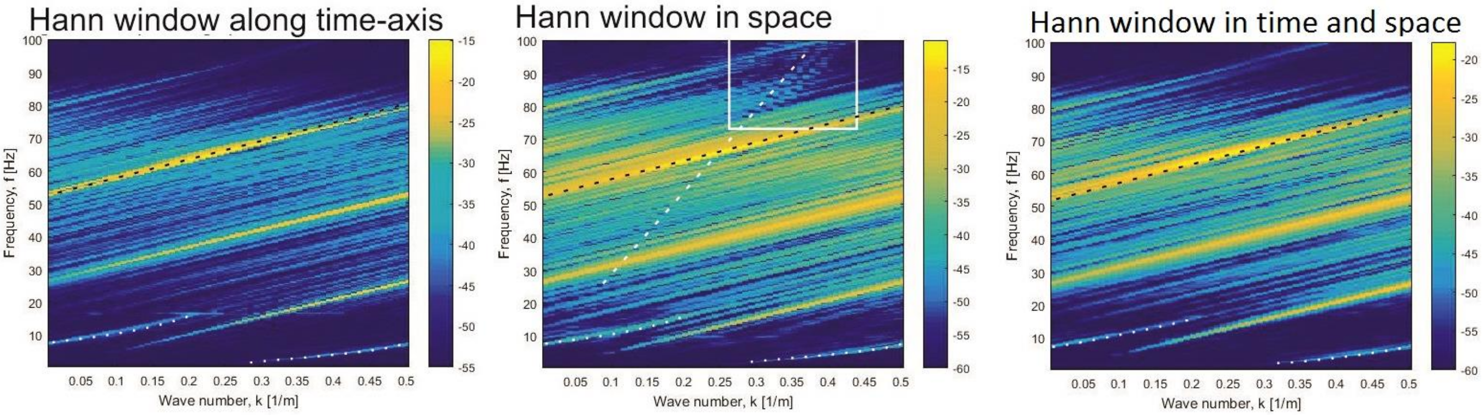

Figure 39 The effect of applying a Hann window in the temporal (left panel), spatial (middle panel) and in both dimensions at the same time (right panel). 65 Hz is indicated by the black dashed line while the flexural wave is indicated by the white dotted line. In the middle panel, different wave modes are resolved and indicated.

The linear events of high energy seen in the f-k spectra are all the same frequency component. As they are parallel and equally spaced, they are continuations of each other. This effect occurs as a consequence of signal sampling in both time and space. However, one can distinguish the real feature from the sampling effect by identifying the feature of highest energy. In **Figure 39**, the highest energy occurs at 65 Hz and hence the rest of the linear features are sampling effects of this component.

As energy appear above 100 Hz with a window applied in the spatial dimension, it is interesting to study higher frequencies of the spectra as well. The spectrum between 0 and 300 Hz is displayed in **Figure 40**, where the same linear events below 100 Hz are still very prominent. As the figure indicates, at least two different linear events are present above 100 Hz. Also, these ones are affected by the sampling and have parallel continuations of themselves. As they are linear, they are non-dispersive, and as their slopes are steeper than the ice related waves, they are of higher velocities. Thus, they are probably originating from the geology below the ice. The two separate events are indicated by a blue and a white dashed line. Using the NMO-velocities given in the previous section along with the relation $v = \frac{2\pi f}{k}$ makes it possible to identify what wave is represented by which linear f-k event by finding the corresponding frequency and wavenumber of the wave. The velocities of the seafloor reflection and the refracted waves match one of these events each. Thus, the blue dashed line in **Figure 40** indicates the seafloor reflection, while the white dashed line indicates the refracted wave. Naturally, they are crossing each other. Where the reflection and the refracted wave interfere with the ice related wave modes they are overprinted.

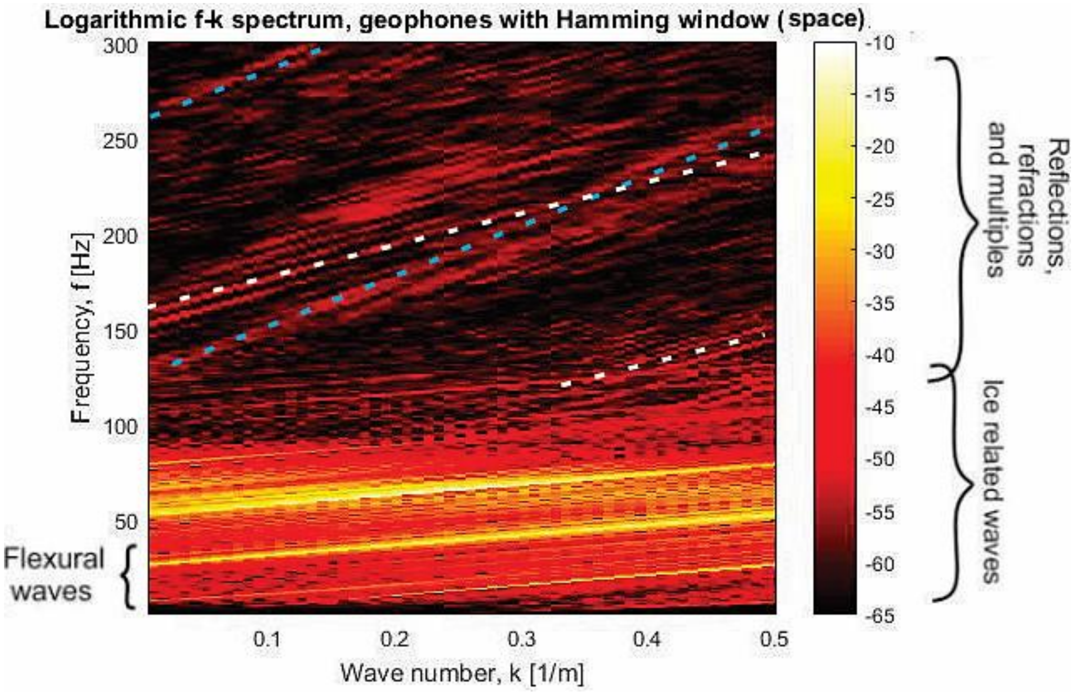

Figure 40 f-k spectrum between 0 and 300 Hz of the geophone spectrogram. Blue dashed line is the seafloor reflection; white dashed line is the refracted wave. Below 100 Hz are ice related wave modes. The flexural wave is not visible at this scale.

As the 65 Hz is non-dispersive, it is an acoustic wave with gradually decreasing bandwidth. A close-up of it is seen in **Figure 41** where it can be seen that the distance between each parallel line is 25 Hz. This is equal to the bandwidth of the component at its narrowest (see **Figure 37**). The dispersive wave is also seen in this figure, but an even further close-up to study it in detail reveals that there are several dispersive features at the very lowest frequencies. This is shown in **Figure 42**.

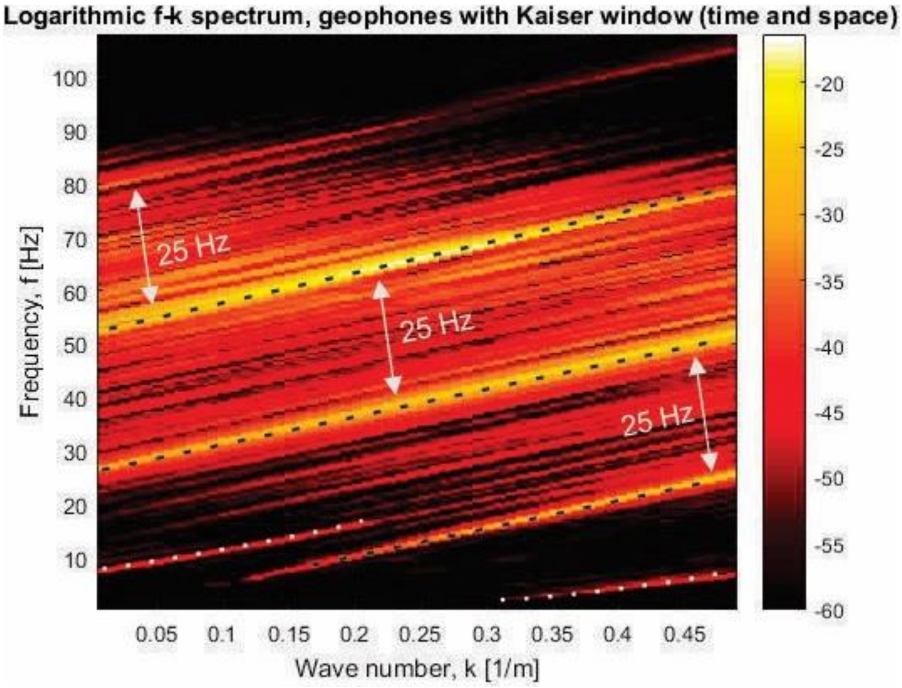

Figure 41 f-k spectrum between 0 and 100 Hz of the geophone seismogram. The black dashed line indicates the 65 Hz component, while the white dotted line indicates the flexural wave.

The frequency of 65 Hz and the corresponding wavenumber of 0.27 m^{-1} gives $v_s = 1775\, m/s$, which is representative of S-waves. The wavelength of this wave is $\lambda = \frac{2\pi}{k} = 27.3\, m$. The particle motion of S-waves is perpendicular to the direction of wave propagation, but the direction of shear is unconstrained such that it may be polarized into either the horizontal or the vertical plane (Pujol, 2003b). As this wave is very prominent in the geophones, the 65 Hz must be a wave causing vertical displacement and thus it is likely a vertically polarized S-wave.

As the air wave and the S-wave travel along each other, the powerful air wave probably generates and pushes the S-wave ahead. Once induced, the S-wave travels very quickly, outrunning both the air wave and the flexural wave that seem to follow each other throughout the entire acquisition. The S-wave is long-lasting and attenuated slowly compared to the flexural wave.

As there are several dispersive events closely spaced at the lower frequencies of the f-k spectrum, the flexural wave must be affected by the sampling as well. As there are so many of them, it is difficult to say which one is the actual flexural wave and which ones are artificial effects from sampling. A close-up of the dispersive components is displayed in the lower panel of **Figure 42**. It is reasonable to think that the event of highest energy is the real flexural wave, however, the frequency range of this does not fit the frequencies observed in the previous analyses. To identify which of these lines represent the flexural wave, the theoretical dispersion relation of flexural waves for different ice thicknesses is estimated. This is done by using the theoretical dispersion relation as was given in Eq. (4.7) (or Eq. (4.8)). Different values for ice thickness is chosen and the resulting frequencies and wavenumbers are seen in the upper panel of **Figure 42**. The graphs make it clear that the dispersion relation is strongly dependent on ice thickness, as the difference is large with only small changes in h. The orange graph of the figure represents an ice thickness of 0.75 m and is the most suitable one for wavelengths and frequencies measured from the single time traces. This is also the curve where frequencies fall within the range of frequencies observed as the flexural wave from the spectrogram analysis and the band-pass filtering. Therefore, this relation is used as the basis for identifying the real flexural wave in the f-k spectrum. The theoretical dispersion relation from the upper panel is indicated by the white dotted line in the spectrum in the lower panel. The frequency range of this one is in accordance to the frequency range 3-12 Hz as previously found for the flexural wave. **Figure 42** also includes a linear event of high energy as indicated by the black dashed line. This is one of the S-waves sampling effect lines.

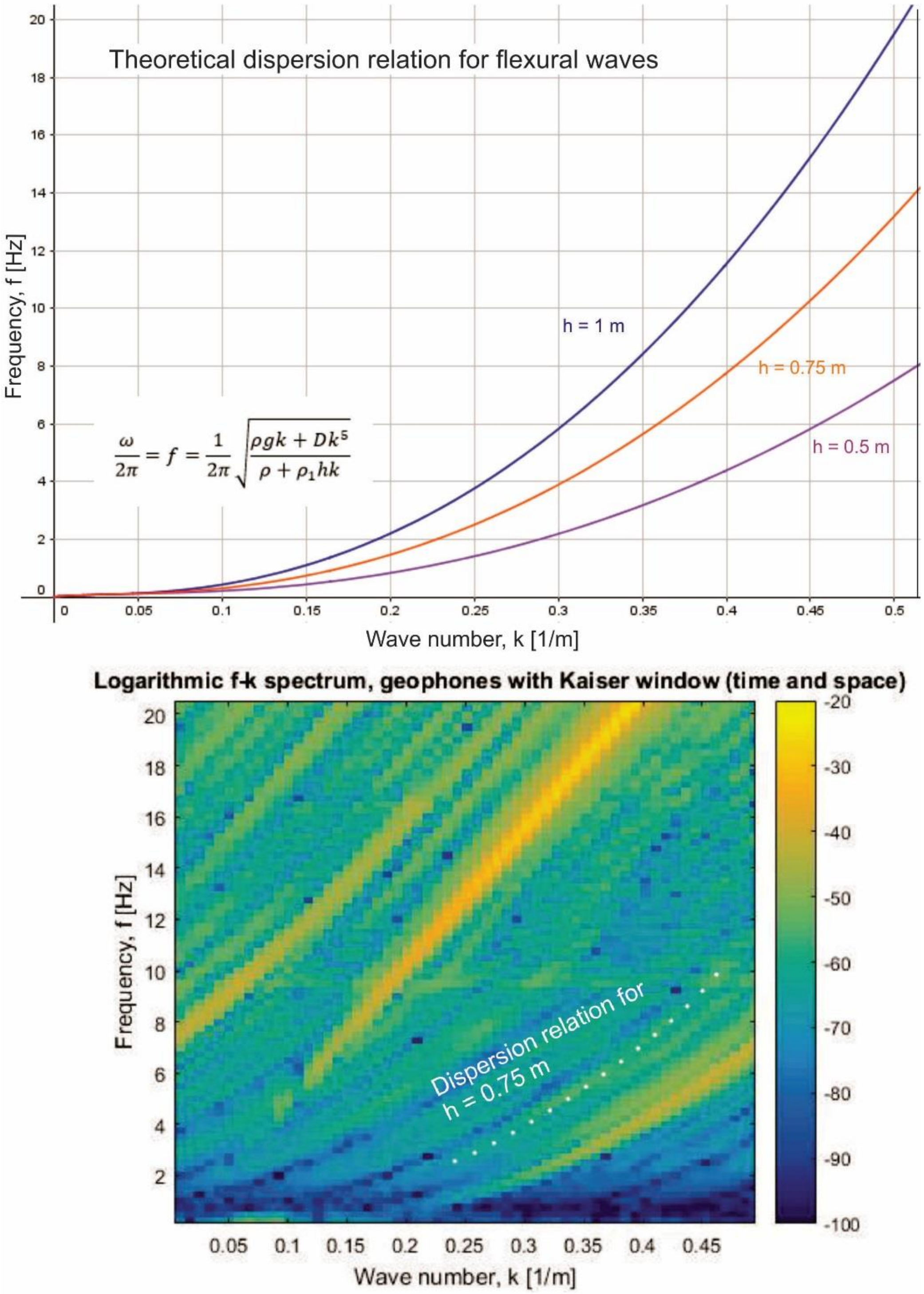

Figure 42 Upper panel: theoretical dispersion relation for flexural waves in ice of thickness 0.5m, 0.75m and 1m. Lower panel: f-k spectrum of geophone data with the theoretical dispersion relation for h = 0.75m indicated. This is the real flexural wave observed in the data.

Both the S-wave and the flexural wave has artificial extensions of themselves. However, the S-wave at 65 Hz is the feature of strongest energy compared to the sampling effects. On the contrary, the flexural wave is rather weak compared to its sampling effects. The explanation may be interference of several sampling effects or the resolution in the plot. Frequencies and corresponding wavenumbers of the realistic flexural wave give velocities ranging between 75 m/s and 160 m/s, and wavelengths in the range of 12-25 m.

The cubic function given in Eq. (4.9) may be written in terms of *h* by the corresponding values of *f* and *k* from the flexural wave dispersion relation.

The variables $\alpha = \frac{-12(1-\nu^2)\rho_1\omega^2}{Ek^4}$ and $\beta = \frac{12\rho(1-\nu^2)(\omega^2-gk)}{Ek^5}$ include all of the physical parameters influencing the wave propagation. As there is no data on these parameters from ice cores or in-situ measurements, values are assumed from reasonable and typical quantities. The S-wave may be utilized to estimate Young's modulus based on the shear wave velocity.

It is known that the relation between Young's modulus and shear modulus, *G*, is (Stein et al., 1998)

$$E = 2G(1+\nu), \tag{5.1}$$

where *G* is found from the shear wave velocity $v_s = \sqrt{\frac{G}{\rho}}$ such that $G = {v_s}^2\rho$. From the shear wave velocity and assuming a Poisson's ratio of 0.33, *E* becomes 7.63 GPa. When Young's modulus and the flexural wave properties are known, ice thickness may be estimated from the model explained by Eq. (4.9).

The densities of ice and sea water are assumed 910 kg/m^3 and 1027 kg/m^3. The gravitational acceleration is 9.81 m/s^2. Plotting the graph of Eq. (4.9) gives the ice thickness at the intersection between the graph and the x-axis. The estimated value of *h* is different for each f-k pair, but the values are close to each other, ranging between 0.74 m and 0.77 m. The graphical solution of Eq. (4.9) for f = 4 Hz and k = 0.3 m^{-1} is shown in **Figure 43** where the intersection is indicated by point C. As the estimated thickness is consistent about the real average thickness at the site, it indicates that the method works well for relatively smooth first year ice. The good match between the estimated and the actual *h* also indicates that the estimated Young's modulus is reasonable.

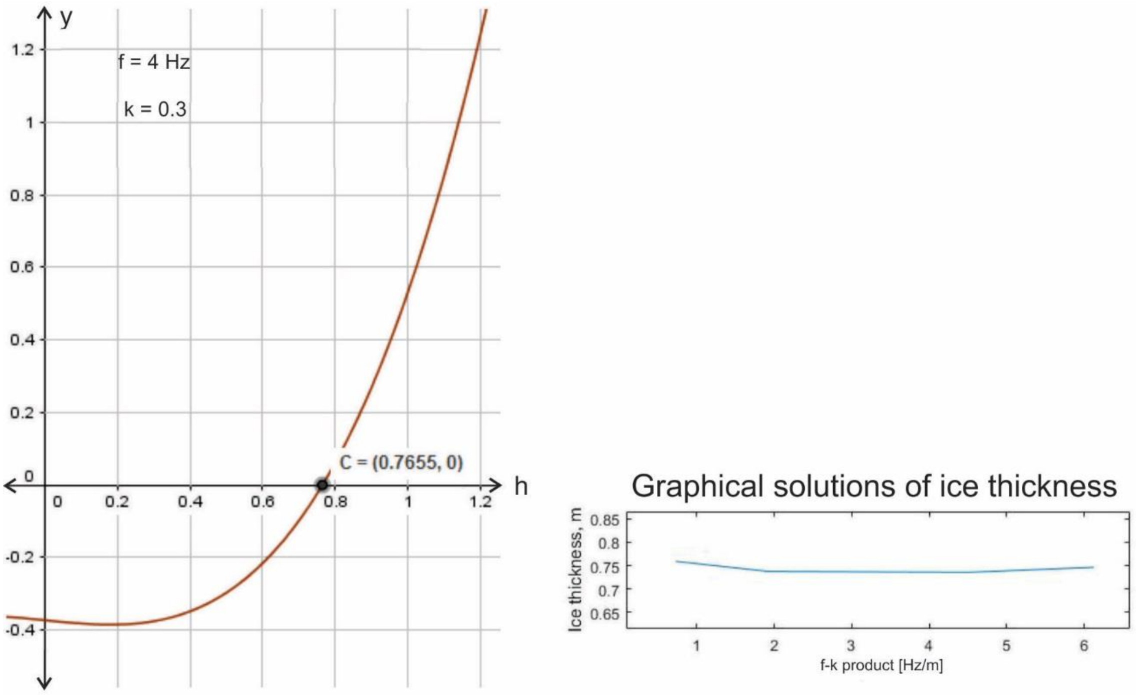

Figure 43 Left panel: graphical solution of h for f = 4 Hz and k = 0.3 m^{-1}. Right panel: thickness estimated from different f-k products.

The cubic function is solved numerically in addition to the graphical solution provided above. The numerical solution, as given in Eq. (4.10), gives an ice thickness ranging between 0.74 m and 0.76 m, giving a very similar "profile" as the one seen in the right panel of **Figure 43**.

As the estimated Young's modulus is representative of the ice at Van Mijenfjorden, the rigidity may be estimated. The flexural rigidity is $D = \frac{Eh^3}{12(1-\nu^2)}$, giving a rigidity of 313.23 x 10^6 Nm or 0.313 GNm. A relationship between D and h may be found based on the estimated rigidity. As D depends on h^3 it is natural that such a relation includes h^3 as well. From the estimated rigidity and the measured ice thickness, the relation becomes $D = 0.706\ h^3$, which is slightly different from the relation derived by DiMarco et al. (1993).

5.7 Background noise measurements

To make sure none of the features identified are noise representatives, measurements of background noise are studied. Energy was recorded a few seconds before the source was fired, revealing the noise present before the detonation. In general, these measurements show low levels of noise. However, the noise is more powerful in the geophones than in the hydrophones as receivers below the ice are influenced less by weather, electronics and surface equipment. Both receiver types show continuous low-frequent noise between 0 Hz and 5 Hz, and thus it may be concluded that what looks like a long-lasting chirp between 12 and 3 Hz is actually not as long as it seems. As the very lowest frequencies are visible before the detonation, they are not reliable as real features. The background noise lengthens the flexural wave chirp, but further examinations of it makes it clear that it terminates after about 2 seconds of duration.

6 Discussion and conclusions

Throughout the exploratory analysis of the data, several features related to floating sea ice have been identified and documented in a way that has not, to our knowledge, been attempted earlier. Following is a discussion of the results and their quality in association to the methods and a concluding summary based on the results. At last, some suggestions for future work on the topic are presented.

6.1 Discussion

Studying the flexural wave by auto correlating single receiver signals has proven the present dispersive waves to decrease in frequency and amplitude as they propagate. At large distances from the source, the autocorrelation functions show components of higher frequencies riding along the flexural wave. Cross-correlation functions between different receivers at different locations indicate the dispersive envelopes very well and makes it possible to estimate the velocities of the flexural wave. From cross-correlating single receivers located 12.5 m from each other, a velocity ranging between 195 m/s and 379 m/s is obtained. As this is a velocity exceeding the air wave velocity, it is likely the phase velocity of the wave. However, the cross-correlation functions between receivers in the central part of the array show little difference between the maximum positive and negative correlations. Thus, it is uncertain whether the velocities estimated from these correlations are accurate or not. The little difference between positive and negative correlations indicate a transition from receiver signals out of phase to signals in phase. A conclusion may be that the wavelength of the flexural wave is close to 12.5 m here.

From the f-k spectrum, flexural wave velocities were estimated based on its frequencies and wavenumbers. Here, velocities are found ranging between 75 m/s and 160 m/s. As these are velocities lower than the air wave velocity, they may represent the flexural wave group velocity. Comparing these velocities to the theoretical dispersion curves (see **Figure 44**) calculated by Jensen (2016), indicate that the group velocity is higher than the phase velocity. However, at the frequency range where the flexural wave is identified and at the suitable thickness in this case, the difference from group to phase velocity is small. Independent of which velocity is the phase velocity and which is the group velocity, the flexural wave velocities found from the data analyses resemble the theoretical velocity ranges for flexural waves at the low frequencies.

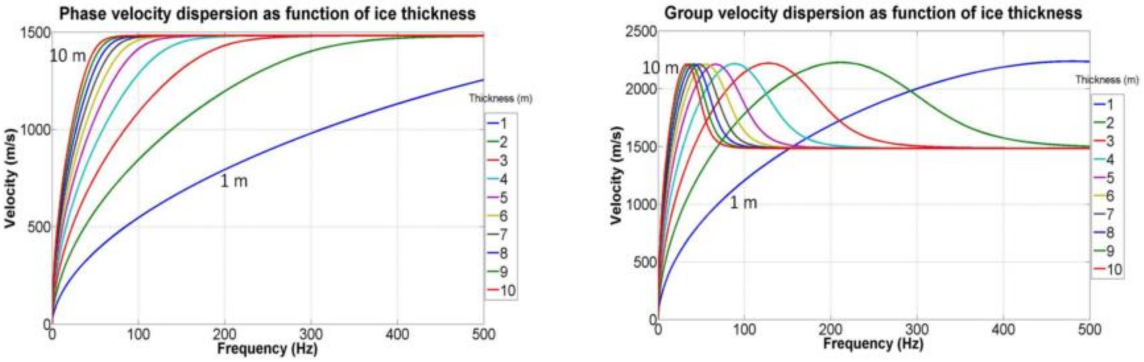

Figure 44 Theoretical dispersion relation for flexural waves giving phase velocity (left panel) and group velocity (right panel) in increasing thick ice. The blue line represents 1 m thick ice, which is most suitable in this case. (Figure by Jensen (2016)).

The frequency content of the signal is estimated by the multitaper method. The power spectral density estimate shows how the energy of the signal is distributed between the different frequencies. As the waves propagating in the ice layer has frequencies within 0 and 100 Hz, the highest energy is found in this range. The entire spectrum expands to the Nyquist frequency at 500 Hz. The energy at the very highest frequencies represents the broad-banded energy originating from the detonation, the air wave, the direct wave in ice, the seafloor reflection and the refracted wave. This is confirmed by studying frequency variations in time by the spectrogram. As NMO-velocities are known from other analyses, the frequency identifications from calculated arrival times of these events are unique.

However, it is possible that the wave identified as the direct wave may be the symmetric Lamb wave. The symmetric mode has much higher velocity than the anti-symmetric mode, as was shown in **Figure 8**, and it is possible that this is the wave arriving first at the receivers. On the other hand, based on the force applied on the ice to generate waves in the survey at Van Mijenfjorden, it is unlikely that the symmetric mode is generated. This was illustrated in **Figure**

9. The first arrival is thus rather a direct wave than the symmetric Lamb mode. The velocity of the direct wave is in accordance to typical P-wave velocities of ice (Stein et al., 1998), and as it is visible in the deep hydrophones, it is a possibility that this the primary wave. As P and S-waves are easily generated waves, they are expected to be present in the data.

The spectrogram provides identification of the flexural wave as this is the only component displayed as a chirp as its frequency decreases with time. The spectrograms reveal a long-lasting component with broad-banded frequencies around 65 Hz, which is seen to override the flexural wave in the single receiver traces. As there is much energy present in the range of the dispersive frequencies, it is difficult to extract the exact frequencies representing the flexural wave and to identify its duration in time. However, when band-pass filtering of only a segment of a single trace is performed, the exact frequencies are found. The filtering separates the low-frequent flexural wave from the high-frequent component. Thus, a relatively accurate frequency content of the flexural wave is obtained, and the 65 Hz component is proven to be non-dispersive but decreasing in bandwidth as it travels. Stein et al. (1998) are among the very few authors who have estimated the frequencies of the flexural wave. They found frequencies between 5 and 50 Hz for the flexural wave, where the flexural wave from the Svea data falls within this frequency range.

Performing a 2D FFT on the geophone seismogram results in the f-k spectrum of the data. Several of the components identified in the spectrograms may be observed in the f-k spectrum as well. The seafloor reflection and the refracted wave are identified based on their velocities. The wavenumber of the 65 Hz component is identified and its velocity is estimated, lying within the typical velocity range of S-waves (Stein et al., 1998). However, as this wave is visible in the hydrophones at 1 m depth as well, there is a possibility that it is a P-wave. That being said, its velocity is simply too low to represent a P-wave and it is rather a shear wave causing motion in the hydrophones through their connection to the geophones at the ice surface. In other words, the S-wave is not actually propagating through the water, but the motion in the geophones is transferred to the hydrophones through the strings connecting them. The 65 Hz is no longer visible at 5 m or deeper, strengthening the assumption of it not actually propagating in the water. As the surface geophones are designed to register vertical motion, the 65 Hz wave must be a vertically polarized shear wave causing vertical deflections rather than horizontal shear.

The high-frequent component riding along the flexural wave is observed in several earlier acquisitions and studies performed by other authors. Among them are Yang and Yates (1994) and Stein et al. (1998), where data were collected in similar environments and manners as the data studied in this thesis. The authors mostly don't comment on this high-frequent component in their data, and if they do, they interpret it as a "noise wave". As the 65 Hz oscillation is not present before the arrival of the air wave, our belief is that it represents a wave generated by the push of the air wave.

A full wave field simulation of flexural waves based on the conditions at Svea in 2013 have been performed by Landschulze (2016). Both a pure elastic and a viscoelastic simulation was performed, resulting in two very different seismograms. The pure elastic simulation has a very prominent component at 66 Hz shown to be depending on the ice thickness. The author refers to this wave as a secondary oscillating noise wave, but our belief is that this is the same wave observed in the real data at 65 Hz. The viscoelastic simulation resembles the real data very well and seem to be the most suitable to model sea ice. The 65 Hz component is, although, only slightly visible in the synthetic data based on this viscoelastic model. As it is likely a shear wave in reality, its vertical motion may not be as amplified in the synthetic data as in the real data.

Several dispersive components are identified in the f-k spectrum. It is natural to believe that the one of highest energy corresponds to the real anti-symmetric flexural wave. However, this proves to be false. The frequency content of this feature does not match the flexural frequencies identified in the other analyses, and thus the theoretical dispersion relation is estimated in order to identify the correct f-k domain feature. The theoretical dispersion relation for 0.75 m thick ice fits the frequency range of 3-12 Hz best, and matches one of the dispersive events of the spectrum very well. It is therefore concluded that this feature must represent the real flexural wave in the data. An explanation for the multiple dispersive events among the lowest frequencies is that they are effects of the sampling in space and time and possible interferences of such effects. The detailed analysis and the application of data windows may give rise to false effects among the low frequencies due to resolution challenges.

To verify some of the results, synthetic data may be used as a reference for comparisons. Jensen (2016) generated synthetic reflections and a flexural wave to study how the flexural wave influences the reflections. Parameters were chosen to match the real conditions at Svea and the modelling of the flexural wave is based on the elastic thin-plate model by Yang and Yates (1994). The same analyses as those performed here on real data was performed on these synthetic reflections and flexural wave as well. The spectrogram shows the frequencies of the flexural wave, and it is in good accordance to the frequencies found from real data analysis. The synthetic reflections are broad-banded, matching the real data reflections in the spectrograms and f-k spectrum. Thus, the interpretations made in the Svea data are in accordance to a synthetic, ideal case. An example of a real data spectrogram with resolved seafloor reflection and multiples is shown in **Figure 45**, where the reflection is clearly broad-banded. The reflections and the refracted wave are close spaced at this distance, and the energy appearing just prior to the reflection is likely the refraction.

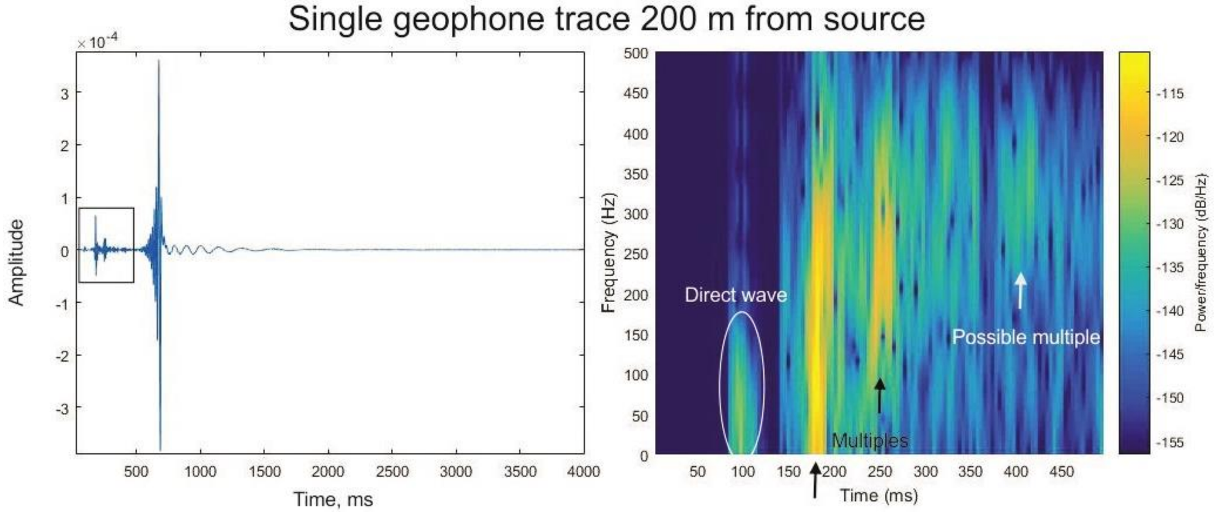

Figure 45 Left panel: single geophone trace at 200 m offset. The first 0.5 seconds are extracted to resolve details in the close spaced events. Right panel: incoming events are indicated in the spectrogram. The black arrow points to the seafloor reflection arriving at 0.17 seconds.

Frequency-wavenumber pairs of both the dispersive and non-dispersive features provides velocities and wavelengths in addition to the frequency ranges. As the vertically polarized shear wave has longer wavelength than the flexural wave, it is the flexural wave that is the secondary oscillation to the S-wave rather than the opposite way around, as it may seem from the single receiver traces. The wavelengths of the flexural wave are longer than the receiver spacing, and thus the flexural wave is probably not exposed to aliasing in space. As the sampling interval in time is very short, aliasing in time is unlikely as well. The flexural wavelengths obtained in this study is in accordance to wavelengths of 5-30 m as estimated by Stein et al. (1998)

The ice thickness is estimated both numerically and graphically by solving a cubic polynomial where the thickness is depending on ice rigidity, ice and water density, and Poisson's ratio. As none of these parameters are known from ice cores or in-situ measurements, they are assumed. Only Young's modulus (implemented in the rigidity) is estimated from the data. As this is based on the shear wave velocity, it may not be accurate. DiMarco et al. (1993) estimated a mean Young's modulus from ice cores to 2.2 GPa, which is very different from the one found here (E = 7.63 GPa). An explanation may be that the type of ice is different, as the ice at their site was much thicker than that of Van Mijenfjorden. However, Stein et al. (1998) created theoretical dispersion curves by assuming the same ice parameters as is assumed in this study. They found that the assumptions who produced the best fit to the measured phase velocities from data was a Young's modulus of 7.2 GPa, a Poisson's ratio of 0.33 and a shear modulus of 2.95 GPa. Their Young's modulus is very close to the one obtained here from the shear wave velocity. As $v_s = 1775\ m/s$ gives $G = {v_s}^2\rho = 2.87$ GPa (in very good accordance to Stein et al. (1998)), the shear wave velocity found from the data analyses performed here is reasonable. The thickness estimated from the dispersion relation being very close to the measured thickness at the site, is yet another indication that the estimate of Young's modulus is representative of the ice.

Shear waves and Rayleigh waves have similar particle motion along the surface of a solid, as indicated in **Figure 46**. The difference is that R-waves propagate only along the surface while S-waves propagate through the entire volume (Gelius & Johansen, 2012). They are similar also in terms of frequency and velocity ranges, but the shear wave velocity is slightly higher than the Rayleigh wave velocity (Plona & Mayer, 1975). Pure Rayleigh waves are non-dispersive, but propagation in the leaky mode shows dispersive behavior (Zhu, Popovics & Schubert, 2004). As sea ice is not homogenous and uniform, it is rather likely that any possible Rayleigh wave is leaky and dispersive. As the 65 Hz component observed in the data has a wavenumber proportional to the frequency, is it not dispersive. Therefore, it is likely that the 65 Hz is a shear wave rather than a Rayleigh wave. The fact that the velocity of this components gives realistic values of shear modulus and Young's modulus in accordance to other authors (DiMarco et al., 1993; Stein et al., 1998), and that these quantities give a very accurate ice thickness, strengthens the assumption of the 65 Hz being a vertically polarized S-wave. In addition, shear waves are easily generated and it would be expected to exist in the data.

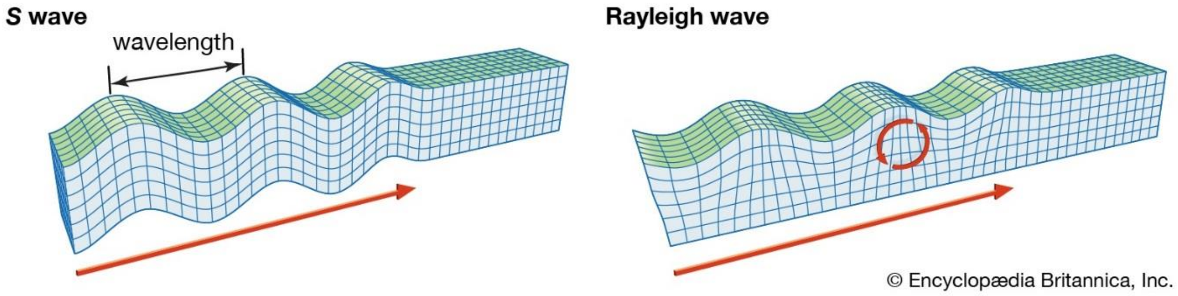

Figure 46 Particle motion of shear and Rayleigh waves are similar at the surface. (Figure is modified from Encyclopædia Britannica, https://www.britannica.com/science/seismic-wave [12.05.17].)

Frequencies and wavenumbers are influenced by the ice thickness and thus f-k pair are required to estimate the thickness. As these are extracted from the dispersive f-k curve matching the theoretical dispersion relation, it is confident that these are accurate. As Poisson’s ratio must be between 0 and 0.5 (Pujol, 2003a), it is not of large significant to the resulting thickness estimate (Ryden et al., 2003). Any mismatch between the measured and the estimated thickness is thus probably due to the other assumed parameters.

DiMarco et al. (1993) derived the dispersion relation on the assumption that the wavelengths are very short relative to the water depth. As the water depth is only about 50 m in the inner basin of Van Mijenfjorden, this may not be a valid assumption in this case and inaccurate results may occur. Also, as sea ice properties vary throughout the ice volume, a thin-plate model assuming homogenous and isotropic ice may give inaccurate estimates of both ice rigidity and thickness. The physical properties of ice vary both horizontally and vertically, where first-year ice mostly vary vertically due to the relatively uniform thickness. As a consequence, assuming uniformity and homogeneity makes a plate model improper for more complex perennial ice (DiMarco et al., 1993). Nevertheless, the estimated value of h is very similar to the measured value even though many assumptions are made. This suggests that reasonable properties are assumed.

The estimated elastic modulus and rigidity of the ice at Van Mijenfjorden is used to find a relationship between D and h as $D = 0.706h^3$. According to DiMarco et al. (1993), the relationship is $D = 0.20h^3$, which is quite different from the relationship estimated from these data. They estimate a rigidity between 6.0 and 8.6 GNm, much higher than the rigidity estimated for the Van Mijenfjorden ice ($D = 0.313$ GNm). However, their study is conducted on ice that is much thicker than in this case. The ice at the site where DiMarco et al. (1993) did their study is up to 3.5 m thick, and naturally it is much stiffer than the thin Van Mijenfjorden ice at 0.76 m. Heat from the relatively warm water below propagates easier through thin ice and thus it is probably even softer and D is small. The large difference from the estimates relation between D and h from this study to the one estimated by DiMarco et al. (1993) may indicate that a general relation like this does not apply to all types of ice. As rigidity is highly variable from different thicknesses and types of ice, the relation between D and h is likely different from one ice floe to the next.

To develop an accurate model to estimate thickness and rigidity based on ice wave frequencies may be accomplished with known ice parameters. In-situ measurements and/or ice cores may provide this. However, as there are so many different possible types of sea ice, a unique model may not be possible to cover any type of ice - and a simplified model based on typical parameters may be sufficient after all.

6.2 Conclusions

Different investigation methods of data collected at Van Mijenfjorden in 2013 have confirmed different wave modes generated by, or in relation to, the floating fjord ice at the site. Studies of several observed frequency components by combination of many frequency estimates have given information about the characteristics of these different wave modes.

- The flexural wave is a high-energy chirp with initial frequency 12 Hz and ending at 3 Hz. Because of its very low frequencies and low energy at the end of the chirp, it is difficult to say for certain how long it lasts in time. However, from studying several spectrograms and the level of background noise, it can be concluded that the chirp is prolonged as offset increases, but lasts no longer than about 2 seconds at the longest.

- The flexural wave phase velocity is estimated from cross-correlations between ice coupled receivers to range from 195 m/s to 379 m/s across the 750-m receiver array. F-k pairs of the flexural wave give the velocity from related frequencies and wavelengths. Such estimates give wavelengths of 12-25 m and velocities within a range between 75 m/s and 160 m/s. As these velocity estimates are quite different, a possibility is that 75-160 m/s is the group velocity of the flexural wave.

- The vertically polarized S-wave observed around 65 Hz has a velocity of 1775 m/s and a wavelength of 27.3 m. It is decreasing in bandwidth from 70 Hz to 25 Hz. The shear wave lasts throughout the full 8 seconds recording time.

- The flexural wave and the S-wave arrives at the same time as the air wave, and the two of them are induces by the vertical push on the ice surface from the air wave. Once generated, the S-wave quickly outruns the flexural wave as its velocity is much greater.

- The air wave is very prominent in all the plots. It has very high energy relative to the other waves generated in the survey, and it is broad-banded with a possible peak frequency about 30 Hz. Its velocity is estimated between 325 m/s and 340 m/s, where the variation probably is an effect of differently enhanced details in different analyses. It is short lasting, but still so powerful that it is visible in the hydrophones at 1 m depth.

- The direct ice wave has a velocity of 2447 m/s and, according to the spectrograms (i.e. **Figure 45**), a frequency range from 0 to 150 Hz. The seafloor reflection has a velocity of 1405 m/s and is broad-banded, covering almost the entire range up to 500 Hz. The multiples arriving after the reflection are broad-banded as well, but with slightly higher velocities than the primary reflection. The refracted wave has much higher velocities than the other wave modes: 4625 m/s. This makes it outrun the other waves and arrive first at the receiver at the crossover distance at approximately 490 m.

- The broad-banded seafloor reflection and refracted wave are visible in the upper part of the f-k spectrum, but overprinted by the high amplitudes of the ice related wave modes (direct wave, flexural wave, S-wave) within the first 150 Hz.

- The rigidity and thickness of the ice are found from the shear wave velocity and the dispersion relation for flexural waves. This gives a Young’s modulus of 7.63 GPa. Solutions of the third-degree polynomial give an estimated thickness between 0.74 and 0.77 m, very close to the actual thickness of the ice.

- The accurate results indicates that the estimated rigidity of 0.313 GNm and quantities of physical parameters are reasonable, and it proves the dispersion relation derived by DiMarco et al. (1993) to represent flexural waves in first year ice very well. Other assumptions made on unknown parameters, like ice and water density and Poisson’s ratio, are evidently reasonable as well.

6.3 Suggestions for future work

As the frequencies of the flexural wave have been identified through several analyses, it may be possible to utilize this information in the processing of data. Attenuating and removing flexural waves from seismograms have proven difficult, but with the frequency range known, the task may simplify. As the range of flexural frequencies is relatively narrow compared to the entire frequency content of the signal, a simple band-pass filter may attenuate the flexural energy by quite a bit. As wave propagation is depending on physical parameters of the material, the frequency content of waves in different types of ice will vary. To identify the flexural frequencies, similar analyses as those performed here is a good alternative.

6.3.1 Muting in the f-k domain

As the f-k spectrum indicates dispersive waves as non-linear events and the ice related waves are very powerful compared to reflections and refractions originating from depth, muting of unwanted events in the f-k spectrum may be efficient. As the wave propagating only in ice has lower velocities than those originating from the geology below the ice, their slopes are gentler in the f-k spectrum. Therefore, muting gently dipping linear events along with non-linear events in the f-k domain may result in relatively clear reflections from depth with less influence by the dispersive energy. It has earlier been shown by Jensen (2015) and Jensen (2016) that f-k filtering is not as efficient as desired when attenuating flexural waves (see chapter **2.5**). However, the filtering performed here was based on velocities not matching the flexural velocities identified in the Svea data during this study. F-k filtering might prove more efficient if accurate velocities and frequencies of the flexural wave as identified from methods as those proposed above.

6.3.2 Seismic interferometry and cross-correlations

Where several receiver types are available, seismic interferometry and cross-correlations are alternatives in the processing. By cross correlating receiver signals from above and below the ice, the flexural wave may attenuate because much of the energy prior to the first correlated receiver attenuates in the correlation function. Primary reflections register as positive particle displacements whether the receiver is located above or below the ice, while parts of the flexural wave is different from the surface receiver to the subsurface receiver. The cross-correlation is a measure of how similar one signal is to another, and therefore it may enhance the primary reflections similar in both receiver types. The most efficient method is probably to correlate signals from a surface geophone and an OBS geophone, as they register the same type of motion. In addition, the OBS signal does probably not contain any flexural energy as it is located too deep to sense the ice motion. Therefore, the OBS signal probably contains only primary reflections from depth, even though they will be relatively weak. Seismic interferometry and cross-correlation with a surface receiver may thus enhance the reflections.

In the data studied in this thesis, hydrophone signals at different depths are available. Estimating cross-correlation functions between one hydrophone with flexural waves and one without may give the same results as the surface geophone and the OBS cross-correlation probably gives. In the Svea data, hydrophones at 1 m, 5 m, 10 m and 20 m depth are available. Of these, mostly just the 1-m deep hydrophones contain dispersive energy and it may be cross-correlated with hydrophones at for example 5 m depth. Unfortunately, the hydrophone data at 1 m and 5 m depth were not collected during the same test. As a consequence, only cross-correlations between hydrophones at 5 m and 10 m depth, and between 5 m and 20 m depth may be estimated. As there are barely any flexural waves in any of these, the cross-correlations are not of use for the purpose of attenuating the flexural wave. Cross-correlations between the 1-m deep hydrophone signal and the other ones are interesting, but as the 1-m deep hydrophone signal was not recorded at the same time as the deeper hydrophone signals, it is not efficient to estimate this correlation.

To ensure enough energy propagating to the seafloor to give deeper reflections, a source located in the water may be sufficient. As both a subsurface source and OBS receivers is operationally difficult, it is not suitable in very deep waters. However, where the water depth is not too large, for example in fjords, this may be a possibility.

6.3.3 Geophone-hydrophone combinations: transfer functions

As several authors (Krohn & Chen, 1992; Barr et al., 1993; George, 1997; Rosales & Antonie, 2004; Septayana et al., 2010) have proposed already, combining geophones with hydrophones may attenuate the flexural wave. By phase shifting the frequencies representing the flexural waves in hydrophone signals and adding them to geophone signals, destructive interference will cancel most of the flexural wave. For this to work, it is required that the primary reflection frequencies have the same phase and interfere constructively when combined with other receiver signals. This has proven difficult to perform earlier as there has been uncertainties about what frequencies the flexural waves contain. As a method for identifying them is now presented through this thesis, the resulting frequencies may be processed for phase shifts and combinations with other receiver type signals.

References

Adizua, O., Ebeniro, J., Ehirim, C., & Adizua, O. (2015). Application of the Frequency-Wave Number (F-K) and the Radial Trace Transform (RTT) in the Attenuation of Coherent Noise in Onshore Seismic Data. *Asian Journal of Earth Sciences, 8*(1), 15-15.

Anderson, D. L., & Weeks, W. F. (1958). A Theoretical Analysis of Sea-Ice Strength. *Eos Trans. AGU., 39*(4), 632–640.

Bakke, S. H. (2015). *Seismiske bølger i havis.* (Master degree), University of Bergen, Department of Earth Science, Bergen.

Barr, F. J., Nyland, D. L., & Sitton, G. A. (1993). Attenuation of flexural ice waves and random noise using geophones and hydrophones. *SEG Technical Program Expanded Abstracts 1993*, 558-561.

Bécherrawy, T. (2013). Ch. 1 "Free Oscillations" *Mechanical and Electromagnetic Vibrations and Waves*. Hoboken: Wiley.

Bronez, T. P. (1992). On the performance advantage of multitaper spectral analysis. *IEEE Trans. Signal Proc., 40*(12), 2941 - 2946.

Brown, A. R., & Abriel, W. L. (2014). The polarity of zero-phase wavelets. *Interpretation, 2*(1), 19F-19F.

Del Molino, G., Rovetta, D., Mazzucchelli, P., Sandroni, S., Rizzo, F., & Andreoletti, C. (2008). Seismic exploration on ice: The flexural wave noise challenge. *SEG Technical Program Expanded Abstracts 2008*, 2571-2575.

DiMarco, R. L., Dugan, J. P., & Martin, W. W. (1991). Ice Motions Forced by Boundary Layer Turbulence. *Journal of Geophysical Research, 96*(C6), 10617-10624.

DiMarco, R. L., Dugan, J. P., Martin, W. W., & Tucker, W. B. (1993). Sea ice flexural rigidity: a comparison of methods. *Cold Regions Science and Technology, 21*(3), 247-255.

Elias, H.-G. (2008). Ch. 17: "Viscoelasticity" *Macromolecules*. Weinheim, Germany: Wiley-VCH Verlag GmbH.

Elverland, E., & Norsk Polarinstitutt. (2008). *Det Arktiske System*. Tromsø: abcGrafisk as.

Ewing, M., Crary, A. P., & Thorne, A. M. J. (1934a). Propagation of Elastic Waves in Ice. Part 1. *Journal of Applied Physics, 5*(6), 165-168.

Ewing, M., Crary, A. P., & Thorne, A. M. J. (1934b). Propagation of Elastic Waves in Ice. Part 2. *Journal of Applied Physics, 5*(7), 181-184.

Feltham, D. L. (2008). Sea Ice Rheology. *Annual Review of Fluid Mechanics 2008, 40*, 91-112.

Fossen, H. (2010). *Structural Geology*. New York: Cambridge University Press.

Gelius, L.-J., & Johansen, T., A. (2012). "Elastic Waves" *Petroleum Geophysics Vol II* (2nd ed., pp. 7 - 68). Bergen: John Grieg AS.

George, D. (1997). OB hydrophone and geophone processing. *Offshore, 57*(4), 28.

Gomez, P., Fernandez, J. P., & Garcia, P. D. (2011). *Lamb Waves and Dispersion Curves in Plates and its Applications in NDE Experiences Using Comsol Multiphysics*. Paper presented at the 2011 COMSOL Conference (5 pages), Stuttgart, 26 - 28 Oct., 2011.

Gorbatov, A., Saygin, E., & Kennett, B. L. N. (2013). Crustal properties from seismic station autocorrelograms. *Geophysical Journal International, 192*(2), 861-870.

Gunther, L. (2012). Ch. 2 "The Vibrating String" *The Physics of Music and Color* (1. ed., pp. 20-23): Springer Science + Business Media.

Hall, K. W., Nieto, C. E., Gallant, E. V., Stewart, R. R., & Cary, P. (2002). *Multicomponent seismic acquisition in the MacKenzie Delta, N.W.T.* Paper presented at the CSEG Geophysics 2002 Convention (4 pages), 2002.

Hanssen, A. (2003). *Introduction to Statistical Signal Processing and Data Analysis*. Lecture notes Fys-261. Physics Department, University of Tromsø.

Henley, D. C. (1999). The radial trace transform: an effective domain for coherent noise attenuation and wavefield separation. *SEG 1999 Expanded Abstracts*, 1204-1207.

Henley, D. C. (2004). Attenuating the flexural ice wave on arctic seismic data. *CREWES Research Report, 16*, 1-17.

Holmes, G. C. (2002). The Use of Hyperbolic Cosines in Solving Cubic Polynomials. *The Mathematical Gazette, 86*(507), 473-477.

Hosking, R. J., & Sneyd, A. D. (1986). *Waves due to Vehicles on Floating Ice Sheets*. Paper presented at the 9th Australasian Fluid Mechanics Conference, Auckland, 8 - 12 December.

Høyland, K. V. (2009). Ice thickness, growth and salinity in Van Mijenfjorden, Svalbard, Norway. *Polar Research, 28*(3), 339-352.

Jenkins, F. A., & White, H. E. (1957). Ch. 12 "The Superposition of Waves" *Fundamentals of Optics* (3rd ed.). New York: McGraw-Hill.

Jensen, K. (2016). *Modelling and processing of flexural wave noise in sea ice.* (Master degree), University of Bergen, Department of Earth Science, Bergen.

Jensen, M. (2015). *Metodar for demping av fleksurbølgjer i havis.* (Master degree), University of Bergen, Department of Earth Science, Bergen.

Krohn, C. E., & Chen, S. T. (1992). Comparisons of downhole geophones and hydrophones. *Geophysics, 57*(6), 841-847.

Lamb, H. (1916). On Waves in an Elastic Plate. *Proceedings of the Royal Society of London, 93*(648), 114-128.

Landschulze, M. (2016). *Full wave field simulation of flexural waves in an acoustic-viscoelastic medium*. Paper presented at the Offshore Technology Conference, Newfoundland, 24. - 26. October.

Lansley, R. M., Eilert, P. L., & Nyland, D. L. (1984). *Surface sources on floating ice; the flexural ice wave.* Paper presented at the 1984 SEG Annual Meeting, Society of Exploration Geophysicists, Atlanta, Georgia.

Mainardi, F., & Spada, G. (2011). Creep, Relaxation and Viscosity Properties for Basic Fractional Models in Rheology. *The European Physical Journal, 193*, 133-160.

Marsan, D., Weiss, J., Larose, E., & Metaxian, J.-P. (2012). Sea-ice thickness measurement based on the dispersion of ice swell. *J. Acoust. Soc. Am., 131*(1), 80-91.

Mastro, M. (2013). Ch. 12: "Fourier Transform" *Financial Derivative and Energy Market Valuation: Theory and Implementation in Matlab®* (pp. 397-457). Hoboken, NJ, USA: John Wiley & Sons, Inc.

Meteorologisk Institutt. (a). Klima siste 50 år, Svalbard Lufthavn på Spitsbergen. Retrieved from http://met.no/Svalbard+lufthavn+p%C3%A5+Spitsbergen.9UFRHWYI.ips (14.11.16)

Meteorologisk Institutt. (b). Hav- og Istjenester. Retrieved from http://met.no/Hav_og_is/ (14.11.16)

Michaels, T. E., Michaels, J. E., & Ruzzene, M. (2011). Frequency–wavenumber domain analysis of guided wavefields. *Ultrasonics, 51*(4), 452-466.

Milsom, J., & Eriksen, A. (2011a). Ch. 1: "Introduction" *Field Geophysics* (4th ed.). Chichester, UK: Chichester, UK: John Wiley & Sons, Ltd.

Milsom, J., & Eriksen, A. (2011b). Ch. 12: "Seismic Reflection" *Field Geophysics* (4th ed.). Chichester, UK: Chichester, UK: John Wiley & Sons, Ltd.

Norwegian Polar Institute. (2016). *The Norwegian Arctic, A Rapidly Changing Climate* Retrieved from http://edition.pagesuite-professional.co.uk/Launch.aspx?EID=41e410b1-b3d8-44fb-80d2-e89c21188923

Park, J., Lindberg, C. R., & Vernon, F. L. (1987). Multitaper spectral analysis of high-frequency seismograms. *Journal of Geophysical Research, 92*(B12), 12675-12684.

Peebles, P. Z. J. (2001a). Ch. 6 "Random Processes - Temporal Characteristics" *Probability, Random Variables and Random Signal Principles* (4th ed.): McGraw-Hill.

Peebles, P. Z. J. (2001b). Ch. 7: "Random Processes - Spectral Characteristics" *Probability, Random Variables and Random Signal Principles* (4th ed.): McGraw-Hill.

Percival, D. B., & Walden, A. T. (1993). Ch. 7: "Multitaper Spectral Estimation" *Spectral Analysis for Physical Applications: Multitaper and Conventional Univariate Techniques*: Cambridge University Press.

Pinet, P. R. (2013). Formation of Sea Ice *Invitation to Oceanography* (6th ed., pp. 166): World Headquarters, Jones & Bartlett Learning.

Plona, T. J., & Mayer, W. G. (1975). Rayleigh and Lamb waves at liquid-solid boundaries. *Ultrasonic, 13*(4), 171-175.

Press, F., Crary, A. P., Oliver, J., & Katz, S. (1951). Air-coupled flexural waves in floating ice. *Transactions. American Geophysical Union, 22*(2), 166-172.

Pujol, J. (2003a). Ch. 4: "Linear elasticity – the elastic wave equation" *Elastic Wave Propagation and Generation in Seismology*. Cambridge, UK: The Press Syndicate of the University of Cambridge.

Pujol, J. (2003b). Ch. 5: "Scalar and elastic waves in unbounded media" *Elastic Wave Propagation and Generation in Seismology*. Cambridge, UK: The Press Syndicate of the University of Cambridge.

Rendelman, C., & Levin, F. K. (1990). Seismic exploration on a floating ice sheet. *Geophysics, 55*(4), 402-409.

Rosales, A., & Antonie, G. (2004). Ocean-bottom hydrophone and geophone coupling. *Stanford Exploration Project, report 115*, 57–70.

Rottmann, K. (2003). *Matematisk Formelsamling (Matematische Formelsammlung)*: Spektrum forlag.

Rovetta, D., Mazzucchelli, P., Del Molino, G., & Sandroni, S. (2009). *Flexural Ice Wave: modelling by analytical approach*. Paper presented at the SEG 2009 International Exposition and Annual Meeting, Houston.

Ryden, N., Park, C. B., Ulriksen, P., & Miller, R. D. (2003). Lamb wave analysis for non-destructive testing of concrete plate structures *Symposium on the Application of Geophysics to*

Engineering and Environmental Problems 2003 (pp. 782-793): Society of Exploration Geophysicists.

Septayana, T., Supriatna, Y., Suprioyono., Schurtet, G., Keggin, J., & Chameau, J. J. (2010). Different approaches of combining geophone and hydrophone data from OBS seismic at Bintuni-Berau Bay, Papua. *PROCEEDINGS, INDONESIAN PETROLEUM ASSOCIATION, Thirty-Fourth Annual Convention & Exhibition*.

Serway, R. A., Moses, C. J., & Moyer, C. A. (2005). Ch. 5: "Matter Waves" *Modern Physics* (3rd ed.): David Harris, for Thomson Learning.

Shearer, P. M. (2009). Ch. 3: "The Seismic Wave Equation" *Introduction to Seismology* (2nd ed.). New York: Cambridge University Press.

Slepian, D. (1978). Prolate spheroidal wave functions, Fourier analysis, and uncertainty V: the discrete case. *The Bell System Technical Journal, 57*(6), 1371-1430.

Squire, V. A., & Allan, A. J. (1980). Propagation of Flexural Gravity Waves in Sea Ice *Sea Ice Processes and Models, Proceedings of the Arctic Ice Dynamics Joint Experiment* (pp. 327-338). Seattle: University of Washington Press.

Stein, P. J., Euerle, S. E., & Parinella, J. C. (1998). Inversion of pack ice elastic wave data to obtain ice physical properties. *Journal of Geophysical Research, 103*(C10), 21.783-721.793.

The MathWorks Inc. fft Fast Fourier Transform. Retrieved from https://se.mathworks.com/help/matlab/ref/fft.html (16.03.17)

The MathWorks Inc. (2015). Multitaper Method. Retrieved from https://www.mathworks.com/examples/signal/mw/signal-ex41524780-multitaper-method (16.03.17)

Thomas, D. N., & Dieckmann, G. S. (2010a). Ch. 2: "Growth, Structure and Properties of Sea Ice" *Sea Ice* (2nd ed.): Blackwell Publishing Ltd.

Thomas, D. N., & Dieckmann, G. S. (2010b). Ch. 4: "Dynamics versus Thermodynamics: The Sea Ice Thickness Distribution" *Sea Ice* (2nd ed.): Blackwell Publishing Ltd.

Thomson, D. J. (1982). Spectrum estimation and harmonic analysis. *Proceedings og the IEEE*, *70*(9), 1055-1096.

Timco, G., & Weeks, W. F. (2009). A review of the engineering properties of sea ice. *Cold Region Science and Technology*, *60*(2), 107-129.

Turcotte, C., & Schubert, G. (2014a). Ch. 3: "Elasticity and Flexure" *Geodynamics* (3rd ed.). Cambridge, UK: Cambridge University Press.

Turcotte, C., & Schubert, G. (2014b). Ch. 7.10: "Viscoelasticity" *Geodynamics* (3rd ed.). Cambridge, UK: Cambridge University Press.

Van Drongelen, W. (2007). *Signal Processing for Neuroscientists: An Introduction to the Analysis of Physiological Signals* (1st ed.). Amsterdam: Academic Press, Elsevier.

Vincent, J. (2012). Ch. 1: "Basic Elasticity and Viscoelasticity" *Structural Biomaterials* (3rd ed.).

Wangen, M. (2010). Ch. 9: “Flexure of the lithosphere" *Physical Principles of Sedimentary Basin Analysis*: Cambridge University Press

White, H. E. (1969). Cross Correlation in Structural Systems: Dispersion and Nondispersion Waves *The Journal of the Acoustic Society of America*, *45*(5), 1118-1128.

Winter, E. F., & Bies, D. A. (1962). Correlation Properties of Flexural Waves in Long Thin Bars. *The Journal of the Acoustic Society of America, 34*(4), 472-475.

Worden, K. (2001). Rayleigh and Lamb Waves - Basic Principles *Strain, 37*(4), 167 - 172.

Yang, T. C., & Yates, T. W. (1994). Flexural waves in a floating ice sheet: Modeling and comparison with data. *The Journal of the Acoustical Society of America*, *97*(2), 971-977.

Yr (NRK & Meteorologisk Institutt). Været som var, Sveagruva (Svalbard).   Retrieved from http://www.yr.no/sted/Norge/Svalbard/Sveagruva/statistikk.html (14.11.16)

Zhang, B.-Q., Zhou, H., Li, G. F., & Guo, J.-Q. (2016). Geophone-seabed coupling effect and its correction. *Applied Geophysics, 13*(1), 145 - 155.

Zhu, J., Popovics, J. S., & Schubert, F. (2004). Leaky Rayleigh and Scholte waves at the fluid–solid interface subjected to transient point loading. *The Journal of the Acoustical Society of America, 116*(4), 2101-2110.

Ziola, S. M., & Gorman, M. R. (1991). Source location in thin plates using cross-correlation. *The Journal of the Acoustic Society of America*, *90*(5), 2551-2556.

Appendix A

The flexure of an ice floe can be described as bending of thin plates. The plates rigidity depends on material properties like Young's modulus, Poisson's ratio and thickness (Yang & Yates, 1994). Following are derivations of the different material parameters that influence the flexure and deformation of plates.

Young's modulus

Young's modulus defines the relationship between stress and strain. The stress on a surface is the force, F, divided by the area of the surface, S. Strain is the change in length of the object, δl, divided by the original length, l. **Figure 47** shows a bar where a force is acting at the cross-section and stretching the bar.

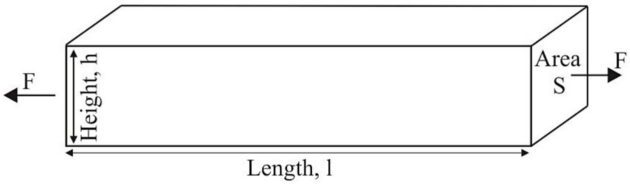

Figure 47 Working force F causes stretching of the bar in the x-direction, resulting in a positive change in length.

Stress is $\frac{F}{S}$, and strain is $\frac{\delta l}{l}$. These are related to each other by a constant, E, such that $\frac{F}{S} = E\,\frac{\delta l}{l}$, where strain is $\varepsilon = \frac{\delta l}{l}$ and E is Young's modulus. This is Hooke's law, defined as (Pujol, 2003a)

$$\sigma = E\varepsilon. \tag{A.1}$$

When strain occurs, internal forces arise in the object and E is depending on the type of deformation that takes place. Type of deformation is depending on other factors like temperature, salinity and porosity (Pujol, 2003a).

Poisson’s ratio

If stress causes stretching in one dimension, it causes contraction in the orthogonal dimension. Therefore, the height of the bar in **Figure 47** will change when the length changes. A positive change in length results in a negative change in height, or vice versa. The change in length and the change in height are related by Poisson’s ratio (Fossen, 2010, p. 81). Because it describes the relative size of change in length to change in height, it is a dimensionless constant given by

$$\frac{\delta h}{h} = -\nu \frac{\delta l}{l}. \tag{A.2}$$

Eq. (A.2) relates longitudinal stretching to transverse compression, where υ is known as Poisson’s ratio. Ryden et al. (2003) concluded that the propagation of Lamb waves is relatively insensitive to changes in Poisson’s ratio, as will be seen from the equation describing flexure of plates in **Appendix C**.

Shear modulus

If a shear force providing simple shear stress acts on a cube, its diagonal will extend or contract. A shear force is a force working in opposite directions on each side of the cube, like **Figure 48** illustrates. The change in length of the diagonal is δd.

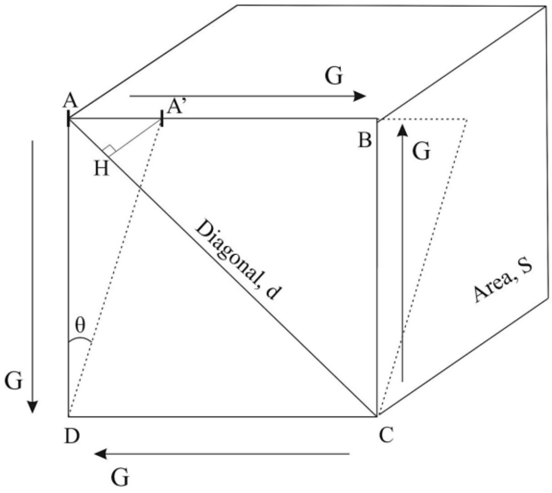

Figure 48 Shear forces acting on a cube.

The corner A will move to a new position, A', during shearing. Triangle AHA' gives the change in the diagonal. The diagonal running across the cube in the opposite direction (*BD*) will be stretched due to shearing from force G. Diagonal AC will change to $A'C$. Trigonometric relations in triangle ADA' gives the angle θ as $\sin\theta = \frac{AA'}{AD}$.

In reality, θ is very small and thus $\sin\theta \approx \theta$ applies (Pujol, 2003a). From the geometry of triangle $AHA',\ AH = AA' = HA'$, and θ is $\theta = \frac{\sqrt{2}AH}{AD}$.

The change of length of the diagonal δd is equal to AH. From geometrical identities, $AD = \frac{d}{\sqrt{2}}$. Then $\theta = \frac{\sqrt{2}\delta d\sqrt{2}}{d} = \frac{2\delta d}{d}$, where strain is $\frac{\delta d}{d} = \frac{1+\nu}{E}\frac{G}{S}$, which gives $\theta = \frac{2(1+\nu)}{E}\frac{G}{S}$.

To simplify, the constant

$$\mu = \frac{E}{2(1+\nu)} \tag{A.3}$$

is defined. This is the shear modulus, which is a materials ability to hold shear and it defines the ratio of shear stress to change in angle (Pujol, 2003a).

Bulk modulus

Consider the same cube as in **Figure 48**, except that now it is lowered into a fluid with a known pressure, P. Given hydrostatic pressure, the fluid constitutes an equal force on all the cubes surfaces and thus the deformation is homogenous and Hooke's law applies in all three dimensions. The length, l, corresponds to the baseline DC in the figure, while height, h, is DA. The width, w, equals the length of the cube in the z-direction.

Because the fluid pressure is higher than air pressure, the volume of the cube is compressed and deformation is in form of volume changes. The volume is $V = lhw$.

After compression, $l = l + \delta l$, $h = h + \delta h$ and $w = w + \delta w$. The volume after compression is $(l + \delta l)(h + \delta h)(w + \delta w)$, and the volume change is $\Delta V = (l + \delta l)(h + \delta h)(w + \delta w) - V$ (Fossen, 2010, pp. 32-33).

Rearrangement gives $\Delta V = V\left(1+\frac{\delta l}{l}\right)\left(1+\frac{\delta h}{h}\right)\left(1+\frac{\delta w}{w}\right) - V$. Due to small quantities, the volume change is approximately

$$\Delta V = V\left(\frac{\delta l}{l}+\frac{\delta h}{h}+\frac{\delta w}{w}\right). \tag{A.4}$$

Because compression is caused by hydrostatic fluid pressure, the change of l is caused by three differently oriented forces. The first is the compression due to forces acting on the end-faces of the cube. From Hooke's law, this is given as

$$\frac{\delta l_1}{l} = -\frac{P}{E}. \tag{A.5}$$

This compression results in an expansion in the orthogonal directions and thus

$$\frac{\delta l_2}{l} = \nu\frac{P}{E} = \frac{\delta l_3}{l}. \tag{A.6}$$

Using Eq. (A.5) and (A.6), the total change in the length becomes

$$\frac{\delta l}{l} = \frac{\delta l_1}{l}+\frac{\delta l_2}{l}+\frac{\delta l_3}{l} = \frac{-P(1-2\nu)}{E}. \tag{A.7}$$

The fluid pressure is equal on all sides and $\frac{\delta l}{l} = \frac{\delta h}{h} = \frac{\delta w}{w}$. Then, from Eq. (A.7), the volume change of the cube is

$$\Delta V = V\left(\frac{\delta l}{l}+\frac{\delta h}{h}+\frac{\delta w}{w}\right) = \frac{-3VP(1-2\nu)}{E}. \tag{A.8}$$

This can be written as $P = -K\frac{\Delta V}{V}$, where

$$K = \frac{E}{3(1-2\nu)} \tag{A.9}$$

is bulk modulus, i.e. the material's ability to resist volume changes (Fossen, 2010, p. 103).

Quantities of material properties

For every material, the direction of shear has to be in the same direction as the applied force. Hence, shear modulus $\mu = \frac{E}{2(1+\nu)}$ has to be positive. For this to be valid, the minimum value of ν is -1 (Pujol, 2003a). However, a negative value of Poisson's ratio is not possible, as this would imply that a material expands in the direction opposite of the stretching. Then, ν must be positive.

From the bulk modulus, $K = \frac{E}{3(1-2\nu)}$, it is obvious that ν has to be smaller than ½ in order for K to be positive (Pujol, 2003a). K has to be positive, as anything else would imply an increase in volume with a positive pressure P, which is not physically possible. Then one can conclude that the value of Poisson's ratio must be $0 < \nu < ½$ (Pujol, 2003a).

As a reference, Ewing et al. (1934a) estimated Young's modulus and Poisson's ratio based on the velocities of body waves in ice. They found a Poisson's ratio at 0.365, while DiMarco et al. (1993) assumes it constant at 0.33 for sea ice. The estimate of Young's modulus by Ewing et al. (1934a) gave 9.17 GPa $\left(= 9.17 * 10^9 \frac{N}{m^2}\right)$.

Appendix B

Equation of motion in one dimension

The 1D wave equation derives from considering a wave propagating along a string as in **Figure 49**. The vertical displacement of the string is described by $u(x)$. When a wave propagates, the string is bent such that a tension force occurs at each end of the string. The two forces, T, are oppositely directed, but due to the curvature of the string, they do not make the exact same angle, θ, to the horizontal. This results in a vertical force, F, pulling the string back to its equilibrium. Depending on whether $u(x)$ is positive or negative, the vertical forces will be negative or positive, and can be termed F_1 and F_2, respectively (Turcotte & Schubert, 2014a).

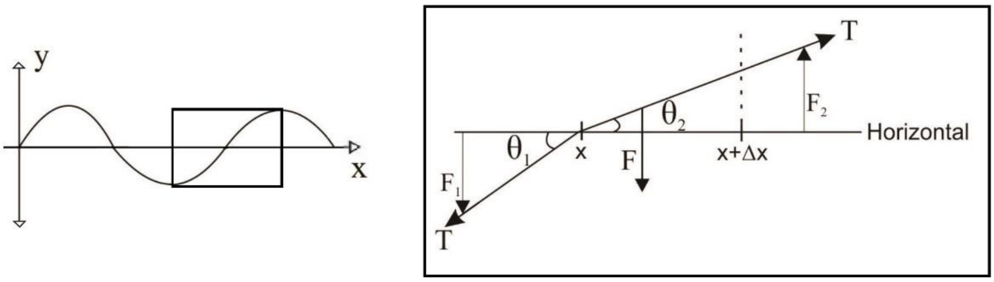

Figure 49 Illustration of waves on a string and related forces in a small segment [x, x + Δx].

Geometrical identities give that $F_1 = -\mathrm{T}\sin\theta_1$ and $F_2 = \mathrm{T}\sin\theta_2$ and thus F_1 is the force caused by motion in negative y-direction. In reality, vertical deflections are small (Pujol, 2003a) and hence θ has to be small. Then $\sin\theta \approx \theta$ is valid and $F_1 \approx \theta_1$ and $F_2 \approx \theta_2$. The net force acting on the string is the sum of F_1 and F_2,

$$F_{net} = F_2 + F_1 = T\theta_2 + (-T\theta_1) = T(\theta_2 - \theta_1). \qquad \text{(B.1)}$$

Due to the small deflections, a small segment of the string is considered plane and inclined. θ is the angle between the string and the horizontal, equivalent to the slope of the string segment $\frac{du}{dx}$ which gives $\theta_1 = \frac{\partial u}{\partial x_{|\Delta x|}}$ and $\theta_2 = \frac{\partial u}{\partial x_{|x+\Delta x|}}$. Substituting this into Eq. (B.1) gives

$$F_{net} = T\left(\left(\frac{\partial u}{\partial x_{|x+\Delta x|}}\right) - \left(\frac{\partial u}{\partial x_{|x|}}\right)\right). \qquad \text{(B.2)}$$

The difference from x to $\Delta x + x$ is simply just Δx, and the slope of the segment is found at the distance Δx. As we are moving in space, time passes and u becomes dependent on t. Therefore,

$$F_{net} = T\left[\frac{\partial u}{\partial x}(x + \Delta x, t) - \frac{\partial u}{\partial x}(x, t)\right]. \tag{B.3}$$

The definition of the derivative is (Rottmann, 2003, p. 127)

$$f'(x) = \lim_{\Delta x \to 0}\left(\frac{f(x + \Delta x) - f(x)}{\Delta x}\right). \tag{B.4}$$

Differentiating Eq. (B.3) and substituting it into Eq. (B.4) gives

$$F_{net} = T\left(\Delta x \frac{\partial^2 u}{\partial x^2}\right). \tag{B.5}$$

To compute the motion of the string resulting from F_{net}, Newton's second law, $F = ma$, is applied. A variable μ is defined as the mass per unit length such that $m = \Delta x \mu$. The acceleration is the second derivative of displacement and can be written as $a = \frac{\partial^2 u}{\partial t^2}$. Newton's second law therefore takes the form

$$T \Delta x \frac{\partial^2 u}{\partial x^2} = \mu \Delta x \frac{\partial^2 u}{\partial t^2}. \tag{B.6}$$

Rearrangements give the equation of motion of a wave propagating in one dimension as (Shearer, 2009)

$$\frac{\partial^2 u}{\partial t^2} = \frac{T}{\mu}\frac{\partial^2 u}{\partial x^2}. \tag{B.7}$$

One can look for a solution on the form $y(x,t) = f(x \pm ct)$, where c is a constant and f is a differentiable function. Then, $\frac{\partial y}{\partial t} = -cf'$ and $\frac{dy}{dx} = f'$. The second derivatives are $\frac{\partial^2 u}{\partial t^2} = c^2 f''$ and $\frac{\partial^2 u}{\partial x^2} = f''$. Substituting $\frac{\partial^2 u}{\partial x^2}$ and $\frac{\partial^2 u}{\partial t^2}$ into Eq. (B.7) gives $c^2 f'' = \frac{T}{\mu} f''$ and $c^2 = \frac{T}{\mu}$ or $c = \sqrt{\frac{T}{\mu}}$. The equation of 1D wave propagation can then be written as

$$\frac{\partial^2 u}{\partial t^2} = c^2 \frac{\partial^2 u}{\partial x^2}. \tag{B.8}$$

Solving the 1D wave equation

The solution of the wave equation is well known, and here we base our description on Pujol (2003b).

Eq. (B.8) is equivalent to

$$\frac{1}{c^2}\frac{\partial^2 u(x,t)}{\partial t^2} = \frac{\partial^2 u(x,t)}{\partial x^2}, \tag{B.9}$$

where $u(x,t)$ is the displacement in time and space and c is assumed constant. Separation of variables is applied to solve this partial differential equation, by assuming that $u(x,t)$ can be written as a product of two independent functions. We write $u(x,t) = X(x)T(t)$, where substitution into Eq. (B.9) gives $X''(x)T(t) = \frac{1}{c^2}X(x)T''(t)$. Rearranging the expression such that functions depending on *x* is on one side and functions depending on *t* is on the other side of the equation gives $\frac{X''(x)}{X(x)}c^2 = \frac{T''(t)}{T(t)}$.

Because X and T are independent functions, each side of the equation is equal to a constant defined as $\frac{X''(x)}{X(x)}c^2 = \lambda = \frac{T''(t)}{T(t)}$.

Rearrangements give two second-order differential equations as

$$X''(x) = \frac{\lambda X(x)}{c^2} \tag{B.10}$$

and

$$T''(t) = \lambda T(t). \tag{B.11}$$

Eq. (B.10) and (B.11) indicate that X and T have to be such that their second derivatives reproduce the function themselves. Functions of this property are among others the sine and cosine functions. To find solutions for the above equations, we now attempt to use $X(x) = Acos(kx)$ and $T(t) = Bcos(\omega t)$ as solutions.

Then $X'(x) = -Aksin(kx)$ and $T'(t) = -B\omega sin(\omega t)$, $X''(x) = -Ak^2cos(kx)$ and $T''^{(t)} = -B\omega^2 cos(\omega t)$. By substitution, Eq. (B.10) and Eq. (B.11) becomes

$-Ak^2cos(kx) = \frac{\lambda}{c^2}Acos(\omega t)$ and $-B\omega^2 cos(\omega t) = \lambda Bcos(\omega t)$. As a deduction, $\lambda = -k^2c^2$ and $\lambda = -\omega^2$, which gives

$$\omega = kc, \tag{B.12}$$

where ω is the angular frequency. In the suggested solution $T(t)$, ω is multiplied with t and thus its unit is $\left[\frac{1}{t}\right]$. k denotes the wavenumber, and similarly its unit has to be $\left[\frac{1}{x}\right]$ from $X(x)$. In other words, Eq. (B.12) is the relationship between frequency and wavenumber, known as the *dispersion relation* of acoustic waves.

As Pujol (2003b) argues: because λ may be any positive, negative, real or complex number, the solutions of Eq. (B.10) and (B.11) are on the form $X(x) = e^{\pm\sqrt{\lambda}\,x/c}$ and $T(t) = e^{\pm\sqrt{\lambda}\,t}$.

The general solution of Eq. (B.9) can be written $u(x,t) = \pm Ae^{\pm\sqrt{\lambda}\,(t-x/c)} + \left(\pm Be^{\pm\sqrt{\lambda}\,(t+x/c)}\right)$, because $u(x,t) = X(x)T(t)$. A and B are arbitrary constants. Thus u depends on x and t through $v = t - \frac{x}{c}$ and $w = t + \frac{x}{c}$ (Pujol, 2003b). For simplicity, these variables are used further.

The general solution is a combination of two second-order differentiable functions, g and h,

$$u(x,t) = h(v) + g(w). \tag{B.13}$$

To verify that $h(v)$ and $g(w)$ satisfies the wave equation, the chain rule applies (Pujol, 2003b). It states that

$\frac{\partial h}{\partial x} = \frac{\partial h}{\partial v}\frac{\partial v}{\partial x} = \frac{-1}{c}\frac{\partial h}{\partial v}$. The second derivative then becomes $\frac{\partial^2 h}{\partial x^2} = \frac{\partial}{\partial v}\frac{\partial h}{\partial x}\frac{\partial v}{\partial x} = \frac{1}{c^2}\frac{\partial^2 h}{\partial v^2}$, and $\frac{\partial^2 h}{\partial t^2} = \frac{\partial^2 h}{\partial v^2}$, where $\frac{\partial^2 h}{\partial v^2}\frac{1}{c^2} = \frac{\partial^2 h}{\partial x^2} \rightarrow \frac{\partial^2 h}{\partial v^2} = c^2\frac{\partial^2 h}{\partial x^2}$. Further,

$$\frac{\partial^2 h}{\partial t^2} = c^2\frac{\partial^2 h}{\partial x^2}, \tag{B.14}$$

which has the same form as Eq. (B.8) (or Eq. (B.9)) and therefore $h(v)$ has to solve it. The same arguments apply to verify that $g(w)$ is a valid solution.

From the chain rule we have that $\frac{\partial g}{\partial x} = \frac{\partial g}{\partial w}\frac{\partial w}{\partial x} = \frac{-1}{c}\frac{\partial g}{\partial w}$ and that $\frac{\partial^2 g}{\partial x^2} = \frac{\partial}{\partial w}\frac{\partial g}{\partial x}\frac{\partial w}{\partial x} = \frac{1}{c^2}\frac{\partial^2 g}{\partial w^2}$.

Then $\frac{\partial^2 g}{\partial t^2} = \frac{\partial^2 g}{\partial w^2}$, where $\frac{\partial^2 g}{\partial w^2}\frac{1}{c^2} = \frac{\partial^2 g}{\partial x^2} \rightarrow \frac{\partial^2 g}{\partial w^2} = c^2\frac{\partial^2 g}{\partial x^2}$. This gives

$$\frac{\partial^2 g}{\partial t^2} = c^2\frac{\partial^2 g}{\partial x^2}, \tag{B.15}$$

which is on the same form as Eq. (B.8) and therefore has to solve it. It can thus be concluded that $h(v) + g(w)$ solves the one-dimensional wave equation given.

The wave equation in three dimension

The following derivation is based on Pujol (2003b).

In three dimensions, u depends on x, y and z. For simplicity, it can be said that u depends on $\boldsymbol{r}$ and t, where $\boldsymbol{r}$ is a vector $\boldsymbol{r} = (x, y, z)$ and the 1D wave equation expands to

$$\frac{\partial^2 u(\boldsymbol{r},t)}{\partial t^2} = c^2\left[\frac{\partial^2 u(x,t)}{\partial x^2} + \frac{\partial^2 u(y,t)}{\partial y^2} + \frac{\partial^2 u(z,t)}{\partial z^2}\right]. \tag{B.16}$$

The partial derivatives of u with respect to x, y and z can be collected in one vector function

$$\nabla^2 u(\boldsymbol{r},t) = \frac{\partial^2 u(x,t)}{\partial x^2} + \frac{\partial^2 u(y,t)}{\partial y^2} + \frac{\partial^2 u(z,t)}{\partial z^2}, \tag{B.17}$$

where ∇^2 denotes the second partial derivative. Substitution of Eq. (B.17) into Eq. (B.16) gives

$$\nabla^2 u(\boldsymbol{r},t) = \frac{1}{c^2}\frac{\partial^2 u(\boldsymbol{r},t)}{\partial t^2}. \tag{B.18}$$

This equation is among others representative of propagating acoustic waves in a three dimensional plate (Pujol, 2003b).

Solving the 3D wave equation

Also Eq. (B.18) may be solved by separation of variables. The same arguments apply here, i.e. u is decomposed into a product of two independent functions such that $F''(\boldsymbol{r})T(t) = \frac{1}{c^2}F(\boldsymbol{r})T''(t)$. Rearrangements and the introduction of the separation constant λ gives $\frac{F''(\boldsymbol{r})}{F(\boldsymbol{r})}c^2 = \lambda = \frac{T''(t)}{T(t)}$.

Rearranged to two second-order differential equations it becomes $F''(\boldsymbol{r}) = \frac{\lambda F(\boldsymbol{r})}{c^2}$ and $T''(t) = \lambda T(t)$. Eq. (B.18) is separated into two second-order differential equations with one solution $T(t) = e^{\pm\sqrt{\lambda}\,t}$. In order to find the solution of $F(\boldsymbol{r})$, separation of variables is applied once more. $F(\boldsymbol{r})$ is separated into three independent functions $F(\boldsymbol{r}) = F(x,y,z) = X(x)Y(y)Z(z)$.

Then $c^2\nabla^2 F(\boldsymbol{r})$ becomes

$$\frac{c^2X''(x)Y(y)Z(z)}{X(x)Y(y)Z(z)} + \frac{c^2X(x)Y''(y)Z(z)}{X(x)Y(y)Z(z)} + \frac{c^2X(x)Y(y)Z''(z)}{X(x)Y(y)Z(z)},$$

which simplifies to

$$c^2\nabla^2 F(\boldsymbol{r}) = \frac{c^2X''(x)}{X(x)} + \frac{c^2Y''(y)}{Y(y)} + \frac{c^2Z''(z)}{Z(z)} = \lambda$$

or

$$\frac{c^2X''(x)}{X(x)} = \lambda_x, \qquad \frac{c^2Y''(y)}{Y(y)} = \lambda_{y,} \qquad \frac{c^2Z''(z)}{Z(z)} = \lambda_z.$$

Three independent differential equations occur as

$$X''(x) = \frac{\lambda_x}{c^2}X(x), \qquad Y''(y) = \frac{\lambda_y}{c^2}Y(y), \qquad Z''(z) = \frac{\lambda_z}{c^2}Z(z).$$

The same argumentation as for the 1D-case give the solutions $X = e^{\pm\sqrt{\lambda_x}\,({x}/{c})}$, $Y = e^{\pm\sqrt{\lambda_y}\,({y}/{c})}$ and $Z = e^{\pm\sqrt{\lambda_z}\,({z}/{c})}$. The complete solution of the 3D wave equation is the combination of all solutions of T and F, and therefore

$$u(\boldsymbol{r},t) = X(x)Y(y)Z(z)T(t)$$

$$= \left(\pm A e^{\pm\sqrt{\lambda}\left(t-{(mx+ly+nz)}/{c}\right)}\right) + \left(\pm B e^{\pm\sqrt{\lambda}\left(t+{(lx+my+nz)}/{c}\right)}\right), \tag{B.19}$$

where $l = \pm\sqrt{\frac{\lambda_x}{\lambda}}$, $m = \pm\sqrt{\frac{\lambda_y}{\lambda}}$, $n = \pm\sqrt{\frac{\lambda_z}{\lambda}}$ and $l^2 + m^2 + n^2 = 1$, indicating that u depends on x, y, z and t by $\boldsymbol{t} \pm (lx + my + nz)$.

On that account, the general solution is (Pujol, 2003b)

$$u(\boldsymbol{r},t) = h\left(t - \left(\frac{lx + my + nz}{c}\right)\right) + g\left(t + \left(\frac{lx + my + nz}{c}\right)\right). \tag{B.20}$$

Eq. (B.20) is known as D'Alembert solution (Pujol, 2003b), which is a traveling wave solution to a 3D wave equation.

To verify that h and g satisfies Eq. (B.18), v and w are defined as $v = t - \frac{1}{c}(lx + my + nz)$ and $w = t + \frac{1}{c}(lx + my + nz)$. The second derivatives of u with respect to v and to x, y, z and t are substituted into Eq. (B.18). To do so, we apply

$$\frac{\partial u}{\partial t} = \frac{\partial u}{\partial v}\frac{\partial v}{\partial t} + \frac{\partial u}{\partial w}\frac{\partial w}{\partial t} = \frac{\partial u}{\partial v} + \frac{\partial u}{\partial w},$$

$$\frac{\partial^2 u}{\partial t^2} = \frac{\partial^2 u}{\partial v^2} + \frac{\partial^2 u}{\partial w^2} + \frac{2\partial^2 u}{\partial v \partial w}$$

and

$$\frac{\partial u}{\partial x} = \frac{\partial u}{\partial v}\frac{\partial v}{\partial x} + \frac{\partial u}{\partial w}\frac{\partial w}{\partial x} = \left(\frac{\partial u}{\partial w} - \frac{\partial u}{\partial v}\right)\frac{l}{c},$$

$$\frac{\partial^2 u}{\partial x^2} = \left(\frac{\partial^2 u}{\partial v \partial w}\frac{\partial v}{\partial x} + \frac{\partial^2 u}{\partial w^2}\frac{\partial w}{\partial x} - \frac{\partial^2 u}{\partial v^2}\frac{\partial v}{\partial x} - \frac{\partial^2 u}{\partial v \partial w}\frac{\partial w}{\partial x}\right)\frac{l}{c} = \frac{l^2}{c^2}\left(\frac{\partial^2 u}{\partial v^2} + \frac{\partial^2 \psi}{\partial w^2} - \frac{2\partial^2 u}{\partial v \partial w}\right).$$

From these relations, the second derivatives with respect to y and z are found from substituting l with m and n. Substitution into Eq. (B.18) gives (Pujol, 2003b)

$$\frac{(l^2 + m^2 + n^2)}{c^2}\left(\frac{\partial^2 u}{\partial v^2} + \frac{\partial^2 u}{\partial w^2} - \frac{2\partial^2 u}{\partial v \partial w}\right) = \frac{1}{c^2}\left(\frac{\partial^2 u}{\partial v^2} + \frac{\partial^2 u}{\partial w^2} + \frac{2\partial^2 u}{\partial v \partial w}\right), \qquad \text{(B.21)}$$

which is valid for $\frac{\partial^2 u}{\partial v \partial w} = 0$. Hence, the equation for waves in three dimensions has the solution $u = h(v) + g(w)$, where g and h are second order differentiable functions. For simplicity, a vector is defined as $\boldsymbol{p} = (l, m, n)$. Because $l^2 + m^2 + n^2 = 1$ (from Eq. (B.21)), $\boldsymbol{p}$ has to be a unit vector and thus $|\boldsymbol{p}| = 1$. Furthermore, $\boldsymbol{p}$ has to be constant, due to l, m and n being independent of x, y and z. Eq. (B.20) can be written

$$u(\boldsymbol{r}, t) = h\left(t - \frac{\boldsymbol{p} \cdot \boldsymbol{r}}{c}\right) + g\left(t + \frac{\boldsymbol{p} \cdot \boldsymbol{r}}{c}\right). \qquad \text{(B.22)}$$

Acoustic seismic wave equations

The 1D wave in Eq. (B.8) can be applied to derive the equations for different seismic waves. The following section is based on the derivation of Shearer (2009).

The one-dimensional wave equation has the general solution $u(x, t) = f(x \pm ct)$ where f is a combination of the functions $h(v)$ and $g(w)$ as found in the previous section. In three spatial dimensions, one has to include stress, strain and displacement. Even though the three dimension equation of motion then becomes more complicated than the one-dimensional one, their solutions are similar (Shearer, 2009).

Because seismic waves are dependent on time and involves both velocity and acceleration, one need to account the effect of momentum. Consider a cube in a coordinate system x, y, z, where forces are working on each face normal to the directions x, y and z. These forces equal the product of the surface area and the traction vector. The sum of forces in all three dimensions is then (Shearer, 2009)

$$F_i = \partial_j \tau_{ij} dxdydz, \tag{B.23}$$

where $\tau_{ij} = [\tau_{11}\ \tau_{21}\ \tau_{31}]$ is the stress tensor and $d_j \tau_{ij}$ denotes the divergence of the stress tensor for each direction x, y and z, meaning i, j = 1, 2, 3. A body force may exist, termed $F_{i\,body} = f_i dxdzdy$. The total force on the cube is the sum of F_i and $F_{i\,body}$. The mass of the cube is $m = \rho dxdydz$ and the acceleration is $a = \frac{\partial^2 u}{\partial t^2}$. Substitution into Newton's second law gives

$$\partial_j \tau_{ij} dxdydz + f_i dxdzdy = \rho dxdydz \frac{\partial^2 u}{\partial t^2}, \tag{B.24}$$

which simplifies to

$$\partial_j \tau_{ij} + f_i = \rho \frac{\partial^2 u}{\partial t^2}. \tag{B.25}$$

Eq. (B.25) is the *momentum equation*. If there are no body forces, the equation is simply (Gelius & Johansen, 2012)

$$\partial_j \tau_{ij} = \rho \frac{\partial^2 u}{\partial t^2}, \tag{B.26}$$

for *i*, *j* = 1, 2, 3. Eq. (B.26) is the *homogenous* momentum equation. In order to solve this, we need to express the stress tensor τ in terms of u. From stress and strain analysis, it is given that the relationship between stress and strain is $\tau_{ij} = \lambda \delta_{ij} e_{kk} + 2\mu e_{ij}$, where λ and μ are Lamé constants. The strain tensor is given $e_{ij} = \frac{1}{2}(\partial_i u_j + \partial_j u_i)$ (Shearer, 2009).

Substitution gives $\tau_{ij} = \lambda \delta_{ij} \partial_k u_k + \mu(\partial_i u_j + \partial_j u_i)$, which together with Eq. (B.26) makes up a set of equations for displacement and stress. Substitution and vector notation for dimensions x, y and z gives

$$\rho \frac{\partial^2 u}{\partial t^2} = \nabla\lambda(\nabla \cdot u) + \nabla\mu \cdot (\nabla u + (\nabla \mathrm{u})^T) + (\lambda + \mu)\nabla\nabla \cdot u + \mu \nabla^2 u. \tag{B.27}$$

Eq. (B.27) is one way of writing the seismic wave equation. The terms involving $\nabla\lambda$ and $\nabla\mu$ are gradients of the Lamé parameters, which are zero in homogenous materials. Then the seismic wave equation simplifies to

$$\rho\frac{\partial^2 u}{\partial t^2} = (\lambda+\mu)\nabla\nabla\cdot u + \mu\nabla^2 u. \tag{B.28}$$

It is possible to separate Eq. (B.28) into solutions of P and S-waves. The divergence (dot product) and the vector identity $\nabla\cdot(\nabla\times\psi) = 0$ gives

$$\frac{\partial^2(\nabla\cdot u)}{\partial t^2} = \frac{(\lambda+\mu)\nabla\nabla\cdot u + \mu\nabla^2 u}{\rho} = \left(\frac{\lambda+2\mu}{\rho}\right)\nabla^2(\nabla\cdot u), \tag{B.29}$$

which can be written as

$$\nabla^2(\nabla\cdot u) - \frac{1}{\alpha^2}\frac{\partial^2(\nabla\cdot u)}{\partial t^2} = 0, \tag{B.30}$$

where $\alpha^2 = \frac{\lambda+2\mu}{\rho}$ is the squared *P-wave velocity*. The part associated with the scalar potential has no curl, meaning no rotational motion occurs and the wave cannot be polarized into another plane. Hence it is a compressional wave (Gelius & Johansen, 2012).

The curl (cross product) of Eq. (B.28) and the vector identity $\nabla\times(\nabla\phi) = 0$ gives

$$\frac{\partial^2(\nabla\times u)}{\partial t^2} = -\left(\frac{\mu}{\rho}\right)\nabla\times\nabla\times(\nabla\times u) = \left(\frac{\mu}{\rho}\right)\nabla^2(\nabla\times u), \tag{B.31}$$

which can be written as

$$\nabla^2(\nabla\times u) - \frac{1}{\beta^2}\frac{\partial^2(\nabla\times u)}{\partial t^2} = 0, \tag{B.32}$$

where $\beta^2 = \frac{\mu}{\rho}$ is the squared *S-wave velocity*. This vector potential has no divergence, meaning it causes no volume changes, and so it corresponds to shear waves (Gelius & Johansen, 2012). From these equations, it is clear that the velocity of P-waves has to be greater than that of S-waves, as $\left(\lambda + \frac{2\mu}{\rho}\right) > \frac{\mu}{\rho}$.

Appendix C

Torque balance in a bent plate

The following section is based on the derivations by Wangen (2010).

When a force is pushing at the surface of a floating plate, torques arises about the z-axis and about a point x in the plate. Torque is caused by rotation and controls the amount of bending. Because the plate is not rotating, the torques are in equilibrium, and because the plate does not have acceleration, the forces are in equilibrium as well. The torque about the z-axis is found from the flexure of a beam of thickness h as illustrated in **Figure 50**. The central fiber of the beam is where the change of length is zero during bending. Above this fiber, the beam compresses, and below it extends. When the change in length is zero, the stress along the x-axis (z = 0) is also zero. Accordingly, $\sigma_{xx} = 0$. The further a fiber is from z = 0, the higher the stress. The length of any fiber is then a function of distance from z = 0, giving $l(z) = (R - z)\phi$.

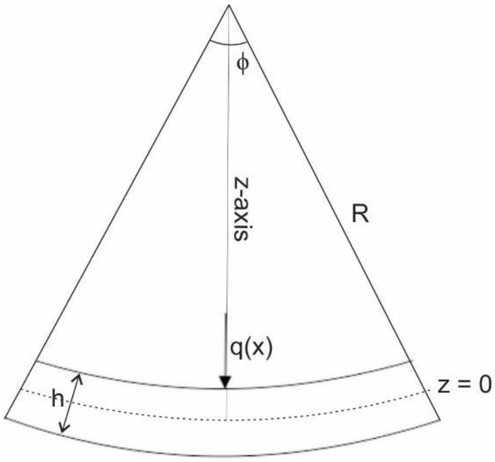

Figure 50 Flexure of a beam of thickness h due to a surface load *q(x)*. The line z = 0 is the neutral fiber of the beam, where bending causes no change in length. R is the curvature radius, and ϕ is the angle of the curvature.

The strain in a fiber is the change in length divided by the original length $\varepsilon_{xx} = \frac{-dl}{l}$, where the minus sign gives that stretching in the x-direction causes compression in the z-direction. When z = 0, the length of the fiber will be $l(0) = (R - 0)\phi = R\phi$, and at position z the change in length is $dl = -z\phi$. Then, the strain is $\varepsilon_{xx} = \frac{-(-z\phi)}{R\phi} = \frac{z}{R}$. Hooke's law gives $\sigma_{xx} = E\frac{z}{R}$. A bundle of fibers of thickness dz, causes a torque dM about the z-axis. Torque is defined as force multiplied by arm, and thus $M = zdF$, where $F = \sigma_{xx}dz$. Thus, $dM = \frac{E}{R}z^2dz$, and the total torque in the beam is

$$M(x) = \int dM = \frac{E}{R}\int_{-\frac{h}{2}}^{\frac{h}{2}} z^2\,dz = \frac{Eh^3}{12R}. \tag{C.1}$$

In **Figure 50**, R denotes the radius of curvature. Because we are dealing with very small motions, the angle of curvature of a beam (or a plate), ϕ, will be very small. Therefore, R has to be very large. The length of the curve along the surface of the beam will be *ds*. This is the distance between each end of the beam, x and dx. Geometrical identities give $ds = R\phi$. The displacement of the beam is $u(x)$ and (Wangen, 2010)

$$\frac{1}{R} = \frac{\frac{d^2u}{dx^2}}{\left(1 + \left(\frac{du}{dx}\right)^2\right)^{\frac{3}{2}}}. \tag{C.2}$$

When the bend of the beam is small, $\frac{du}{dx}$ is very small and thus

$$\frac{1}{R} \approx \frac{d^2u}{dx^2}. \tag{C.3}$$

Substituting R from Eq. (C.1) with Eq. (C.3) gives

$$M(x) = \frac{Eh^3}{12}\frac{d^2u}{dx^2}. \tag{C.4}$$

When the beam expands to a plate, the stretching takes place in the xy-plane and $\varepsilon_{zz} = 0$. From Poisson's formulas, it is known that $\varepsilon_{zz} = \frac{1}{E}(\sigma_{zz} - \nu\sigma_{xx} - \nu\sigma_{yy})$. Because the stretching is only in the x-direction, $\sigma_{yy} = 0$ and $\sigma_{zz} = \nu\sigma_{xx}$. This gives that $\varepsilon_{xx} = \frac{1}{E}(1-\nu^2)\sigma_{xx}$, and the torque about the z-axis in a plate instead of a beam is (Wangen, 2010)

$$M(x) = \frac{Eh^3}{12(1-\nu^2)}\frac{d^2u}{dx^2}. \tag{C.5}$$

The surface load causes torque about a point x along the horizontal axis as well. The distance vector of this torque is $(x'-x)$, and the torque working at this distance is $d\tau(x) = (x'-x)q(x')$. For the entire x-axis, the torque is

$$\tau(x) = \int_x^\infty (x'-x)q(x')dx'. \tag{C.6}$$

Torque balance requires that Eq. (C.6) equals Eq. (C.5), and therefore

$$\frac{Eh^3}{12(1-\nu^2)}\frac{d^2u}{dx^2} = \int_x^\infty (x'-x)q(x')dx'. \tag{C.7}$$

To solve for $q(x)$, the general formula (Rottmann, 2003, p. 129)

$$\frac{d}{dx}\int_{a(x)}^{b(x)} f(x,x')dx' = b'(x)f(x,b) - a'(x)f(x,a) + \int_{a(x)}^{b(x)} \frac{\partial f}{\partial x}(x,x')dx'$$

applies. Here, $a(x) = x, b(x) = \infty$ and $f(x,x') = (x'-x)q(x')$ and it follows that $a'(x) = 1, b'(x) = 0$ and $\frac{\partial f}{\partial x} = -q(x')$. This gives the deflection of a plate from a surface load as (Wangen, 2010)

$$\frac{Eh^3}{12(1-\nu^2)}\frac{d^4u}{dx^4} = q(x). \tag{C.8}$$

Flexure of a plate

Because the plate is floating on top of a fluid, the fluid pushes back on the plate as it deflects, and the difference in density of ice and water becomes essential. The push from the water is $\Delta\rho g u(x)$, and the total vertical forces in the plate are $q(x) - \Delta\rho g u = 0$, where $q(x)$ is working downwards and $\Delta\rho g u$ is working upwards. Here, $\Delta\rho$ is the difference in water and ice density. The equation of deflection of a plate into a fluid is henceforth (Wangen, 2010)

$$D\frac{d^4u}{dx^4} + \Delta\rho g u = q(x), \qquad \text{(C.9)}$$

where $D = \frac{Eh^3}{12(1-\nu^2)}$ is the flexural rigidity of the plate. As q is an arbitrary surface load, Eq. (C.9) may represent the deflection caused by any source type, i.e. a line and/or a point source.

Motion in viscoelastic materials

Ch. 2 argues that the best representation of sea ice deformation is by viscoelastic deformation. As the Maxwell-Voigt model describes, strain in viscoelastic deformation decomposes into an elastic (recoverable) and a viscous (permanent) component. Then, strain is $\varepsilon = \varepsilon_e + \varepsilon_v$ (Elias, 2008). In the same way, the flexure of the plate decomposes into the same components and $u = u_e + u_v$ (Wangen, 2010). Because viscous properties are depending on time, the strain and deflection depend on time (Elias, 2008; Fossen, 2010, pp. 103-109) and for that reason, the equation of flexure of a viscoelastic plate must contain a time derivative of deflection (Wangen, 2010), denoted $\dot{u}$, where the dot above denotes its time derivative. This accounts for all the following terms.

The elastic part of strain will simply equal $\varepsilon_e = \frac{\sigma}{E}$ according to Hooke's law. Meanwhile, the viscous component of strain is time dependent $\left(\dot{\varepsilon}_v \equiv \frac{d\varepsilon_v}{dt}\right)$ and it follows that $\dot{\varepsilon}_v = \frac{\sigma}{\mu}$, where μ is the viscosity. The total strain is thus $\dot{\varepsilon} = \varepsilon_e + \dot{\varepsilon}_v = \frac{1}{E}\left(\dot{\sigma} + \frac{\sigma}{t_e}\right)$, where $t_e = \frac{\mu}{E}$ is a time constant (Wangen, 2010).

Because the strain is time dependent, the torque balance in the viscoelastic plate must be so too. Following the same derivation of torque balance as above (Eq. (C.1) – (C.4)), except that now the strain is $\dot{\varepsilon} = \frac{1}{E}\left(\dot{\sigma} + \frac{\sigma}{t_e}\right)$, gives that the momentum in a viscoelastic plate is (Wangen, 2010)

$$\dot{M} + \frac{M}{t_e} = \frac{Eh^3}{12}\frac{\partial^2 \dot{u}}{\partial x^2} = D\frac{\partial^2 \dot{u}}{\partial x^2}, \qquad \text{(C.10)}$$

which must equal the external momentum of Eq. (C.6). As above, differentiating twice gives the deflection of a viscoelastic plate as (Wangen, 2010)

$$D\frac{\partial^4 \dot{u}}{\partial x^4} = \dot{q} + \frac{q}{t_e}, \qquad \text{(C.11)}$$

indicating that the deflection of viscoelastic plates is a function of both temporal and spatial derivatives. Because sea ice is floating on water, buoyancy supports the plate. The total vertical load is $q - \Delta\rho g u$ and the equation of flexure becomes (Wangen, 2010)

$$D\frac{\partial^4 \dot{u}}{\partial x^4} + \Delta\rho g \dot{u} + \Delta\rho g \frac{u}{t_e} = \dot{q} + \frac{q}{t_e}. \qquad \text{(C.12)}$$

Here, $D = \frac{Eh^3}{12}$ denotes the plate's rigidity. The $(1 - \nu^2)$ term from above may be left out because of its little influence on the deflection. The term will be close to one, because we know $0 < \nu < ½$ for all materials. Like explained in **Ch. 2**, Eq. (C.12) makes a basic model for flexural wave propagation in viscoelastic sea ice.